

Alma Mater Studiorum  
Università degli Studi di Bologna

---

Facoltà di Scienze Matematiche Fisiche e Naturali  
Dottorato di ricerca in Astronomia  
Ciclo XXI

**Gravitational Waves and  
Cosmic Microwave Anisotropies:  
from theory to data analysis for *Planck***

di  
Francesco Paci

Coordinatore dottorato :  
Prof. Lauro Moscardini

Relatore:  
Prof. Lauro Moscardini

Co-relatore:  
Dott. Fabio Finelli

---

Settore Scientifico Disciplinare: Area 02 - Scienze Fisiche  
FIS/05 Astronomia e Astrofisica  
Anno 2009



This thesis has been carried out  
at INAF/IASF-Bologna as part of  
the institute research activity



# Contents

<b>Introduction</b>	<b>1</b>
<b>1 The expanding universe</b>	<b>3</b>
1.1 The evolution of the universe . . . . .	3
1.2 The Standard Big Bang model . . . . .	6
1.3 Theory of cosmological perturbations . . . . .	8
1.4 Characterizing radiation field . . . . .	10
1.5 CMB Temperature anisotropies . . . . .	12
1.6 CMB Polarization . . . . .	14
1.7 The <i>Planck</i> mission . . . . .	15
<b>2 Gravitational waves background</b>	<b>19</b>
2.1 GW in Robertson-Walker metric . . . . .	19
2.2 Inflationary spectrum . . . . .	21
2.2.1 Post inflationary evolution . . . . .	22
2.3 Interaction with non collisional matter . . . . .	23
2.4 Relation with Weinberg's integro-differential equation . . . . .	26
2.5 Interaction with primordial magnetic fields . . . . .	28
2.5.1 Impact of PMF on CMB anisotropies . . . . .	33
2.6 Energy Momentum Tensor . . . . .	34
2.6.1 GW equation of state . . . . .	37
<b>3 CMB foreground cleaning</b>	<b>41</b>
3.1 Astrophysical foregrounds . . . . .	41
3.1.1 CMB and foreground reconstruction methods . . . . .	43
3.2 Internal linear combination . . . . .	44
3.2.1 Algebra of the method . . . . .	44
3.2.2 Polarization . . . . .	45
3.2.3 Errors . . . . .	46
3.3 ILC for <i>Planck</i> . . . . .	46
3.3.1 No-noise limit . . . . .	47

---

3.3.2	Noisy case . . . . .	53
3.3.3	Impact of ILC on $r$ . . . . .	54
3.4	Template fitting . . . . .	56
<b>4</b>	<b>CMB power spectrum estimation</b>	<b>59</b>
4.1	Pseudo- $C_l$ estimator . . . . .	59
4.1.1	Some technical details . . . . .	61
4.2	Quadratic Maximum Likelihood estimator . . . . .	62
4.2.1	Algebra of QML . . . . .	62
4.3	<i>BolPol</i> - a QML for <i>Planck</i> . . . . .	63
4.4	<i>BoLike</i> - a pixel-based likelihood code for <i>Planck</i> . . . . .	64
4.5	<i>BolPol</i> on <i>Planck</i> simulated data . . . . .	65
4.6	<i>Super 70GHz</i> channel . . . . .	65
4.7	Application to <i>WMAP</i> low-resolution data . . . . .	74
4.7.1	Results . . . . .	74
	<b>Conclusions</b>	<b>91</b>
	<b>A Scalar and vectors magnetic modes</b>	<b>91</b>
	<b>B EMT integrals</b>	<b>95</b>
	<b>C QML derivation</b>	<b>97</b>
	<b>Bibliography</b>	<b>99</b>

# Introduction

Primordial gravitational waves are a key-prediction of inflation [1, 2, 3, 4, 5]. The amplitude of gravitational waves depends on the energy scale at which inflation occurred and a detection of such a background would then provide information on the inflationary energy scale. Similar considerations hold for models alternative to inflation, where the accelerated stage was not described by  $\ddot{a}/a \sim \text{const}$  [6, 7, 8]. Gravitational waves are not responsible for the structure of the universe we see today since they are not coupled to the energy density of matter. However, in the same way as scalar perturbations do, they induce fluctuations in the cosmic microwave background (CMB) [10, 9]. The CMB anisotropy pattern generated by scalar perturbations and by gravitational waves are different: beside the different temperature anisotropies and  $E$  polarization, gravitational waves generate polarization  $B$ -modes, whereas scalar perturbations do not.

Since the first detection of CMB anisotropies carried out by the COBE satellite in 1992 [11], several efforts have been done in planning CMB experiments (some of them are Boomerang[12], *WMAP* [13], ACBAR [14], DASI [15], CBI [16], Clover [17], BICEP [18], *Planck* [19], Quiet [20], B-pol [21], CMBPol [22]) and designing the instrumental configurations to reach higher sensitivities and angular resolution.

In this thesis we present a study of primordial gravitational waves, mainly in relation to CMB anisotropies. After an introductory chapter and a theoretical one, we dedicate two chapters to specific works done for the *Planck* satellite. The outline is the following.

In chapter 1 we review some basics of standard cosmology, the observable evidences of the Hot Big Bang model and the formalism for studying the cosmological perturbations. We provide then an introduction to CMB anisotropies in intensity and polarization. A section is then dedicated to the *Planck* mission, its instrumental characteristics and its scientific capabilities.

In chapter 2 we provide an analytical and numerical treatment of waves

gravitational waves evolution in presence of free-streaming matter - as neutrinos - and in presence of a background of inhomogeneous magnetic fields. Through the Boltzmann formalism, we derive analytically the interaction between gravitational waves and free-streaming massless and massive matter. We then discuss how the presence of free-streaming matter affects the behaviour of gravitational waves when a fully inhomogeneous component - as a stochastic background of primordial magnetic fields - is present. We also discuss the form of the energy-momentum tensor of gravitational waves from first principles.

In chapter 3 we tackle the issue of polarized foreground removal for the *Planck* mission. By masking the most contaminated region of the sky corresponding to the galactic plane, we test the Internal Linear Combination (ILC) procedure through a numerical implementation of the method on simulated CMB and foreground maps and by considering the nominal instrumental noise levels for *Planck*. The goodness of the cleaning process is then studied in terms of impact on tensor-scalar ratio. An alternative more viable method for cleaning *B*-modes which makes use of templates is suggested and its capabilities for polarization *B*-modes quantified in terms of impact on the tensor-scalar ratio.

In chapter 4 we move to CMB power spectrum estimation and likelihood evaluation. We present an implementation of the Quadratic Maximum Likelihood approach - *BolPol* - for the estimation of temperature and polarization power spectra. *BolPol* handles full instrumental noise covariance matrix and performs a joint estimate of all the six angular spectra. A naturally derived likelihood code is also presented. An application to *Planck* simulated data, i.e. a work conducted within the *Planck* CTP working group activity is reported. Furthermore, we present a reanalysis of *WMAP* low-resolution five year data performed with our power spectrum estimation and likelihood code.

# Chapter 1

## The expanding universe

In this first chapter we shall review some basic concepts of standard cosmology and CMB radiation. Many books and review articles in the literature cover such topics [26, 27, 28, 29, 30], ranging from popular to more technical ones. This is meant to be an introduction to the physics of CMB together with a summary of the *Planck* satellite capabilities, in order to give the reader a framework for the more technical issues tackled in the next chapters.

### 1.1 The evolution of the universe

It is an evidence that matter in the universe is clustered in stars, galaxies and cluster of galaxies. However, observations at scales larger than these structures show that the distribution of matter is homogeneous and isotropic at high level. Although the observation of homogeneity and isotropy necessarily concerns *our* observable universe, i.e. the universe observed from just one point, we assume this is the case from any other position in the universe as well. Such assumption leads to the *Cosmological Principle*, according to which

*space-time is sliced in spatial hypersurfaces and such hypersurfaces are homogeneous spaces,*

being their time evolution parametrized by the so-called cosmic time.

Relying on General Relativity (GR) for the dynamical evolution of space-time continuum and matter, the Cosmological Principle represents the starting point for characterizing the metric of the universe. GR is a geometric and relativistic theory of gravitation: a description of gravitation interaction as modification of space-time geometry which leads, in the absence of

gravitation itself, to Minkowski space-time. Einstein field equations are<sup>1</sup>

$$G_{\mu\nu} \equiv R_{\mu\nu} - \frac{1}{2}Rg_{\mu\nu} = 8\pi GT_{\mu\nu}. \quad (1.1)$$

The left-hand side of these equations (the Einstein tensor) describes the geometry of space-time through the metric tensor ( $g_{\mu\nu}$ ) and its first and second derivatives contained in the Ricci tensor ( $R_{\mu\nu}$ ) and the Ricci scalar ( $R$ ). On the right-hand side, instead, the energy-momentum tensor ( $T_{\mu\nu}$ ) is responsible for energy and momentum carried by matter.  $G$  is the Newton constant.

Homogeneity and isotropy lead to specific form for the metric: spatial hypersurfaces are constant-curvature space and the line element takes the form

$$ds^2 = dt^2 - a^2(t) \left[ \frac{r^2}{1 - kr^2} + r^2(d\theta^2 + \sin^2\theta d\phi^2) \right] \quad (1.2)$$

where spherical polar coordinates have been adopted. This is the so-called Friedmann-Robertson-Walker (FRW) line element, fully described by the scale factor  $a(t)$ . The quantity  $k$  parametrizes the spatial curvature, determining then its geometry:

$$\begin{aligned} k < 0 & \quad \text{hyperbolic geometry} \\ k = 0 & \quad \text{euclidean geometry (flat)} \\ k > 0 & \quad \text{spherical geometry} \end{aligned}$$

The homogeneous expansion of the universe is thus described by the time evolution of the scale factor, being its expansion rate the Hubble parameter,

$$H = \frac{\dot{a}}{a}. \quad (1.3)$$

where dot denotes derivative with respect to time  $t$ .

The same symmetries assumed for the background space-time must hold for energy-momentum tensor as well. It follows that in FRW metric, the energy-momentum tensor of a fluid takes the diagonal form

$$T_{\mu\nu} = pg_{\mu\nu} + (\rho + p)u_\mu u_\nu \quad (1.4)$$

where  $\rho$  and  $p$  are the energy density and isotropic pressure of the fluid respectively.  $u^\mu$  is the 4-velocity of the fluid, defined and normalized as

$$u^\mu \equiv \frac{dx^\mu}{adt}, \quad u^\mu u_\mu = -1. \quad (1.5)$$

---

<sup>1</sup>We assume  $c = 1$

The conservation of gravitational field sources is a direct consequence of contracted Bianchi identities,  $G_{\mu\nu}{}^{;\nu} = 0$ , from which

$$T_{\mu\nu}{}^{;\nu} = 0 \quad (1.6)$$

By feeding Eq. (1.4) into Eq. (1.6) conservation equations reduce to

$$\dot{\rho} + 3H(\rho + p) = 0 \quad (1.7)$$

Also Einstein equations under the assumption of FRW metric assume a much simpler form, reducing to just two equations for scale factor time evolution,

$$\begin{aligned} H^2 &= \frac{8\pi G}{3}\rho - \frac{k}{a^2}, \\ \ddot{a} &= -\frac{4\pi G}{3}(\rho + 3p)a, \end{aligned} \quad (1.8)$$

called Friedmann equations.

It is worth defining a critical density

$$\rho_{\text{cr}} \equiv \frac{3H^2}{8\pi G} \quad (1.9)$$

and a density parameter

$$\Omega \equiv \frac{\rho}{\rho_{\text{cr}}} \quad (1.10)$$

From the definitions above and the Friedmann equations it is evident that  $1 - \Omega$  is a measure of the curvature of the universe. Although time dependent, it keeps the same sign throughout the evolution of the universe and therefore the same does the curvature.

Another quantity which is particularly useful to introduce is a new time coordinate, the conformal time, defined as

$$\eta \equiv \int \frac{dt}{a(t)}. \quad (1.11)$$

In conformal time FRW metric becomes conformal to Minkowski space-time,

$$ds^2 = a(\eta)^2(-d\eta^2 + \gamma_{ij}dx^i dx^j), \quad (1.12)$$

where  $\gamma_{ij} = \delta_{ij}$  if the spatial hypersurfaces curvature vanishes ( $k = 0$ ). Denoting with a prime the derivative with respect to conformal time and

introducing the conformal Hubble parameter,  $\mathcal{H} = a'/a$ , Friedmann and conservation equations take the form

$$\mathcal{H}^2 = \frac{8\pi G}{3}\rho a^2 - k, \quad (1.13)$$

$$\mathcal{H}' = -\frac{4\pi G}{3}(\rho + 3p)a^2, \quad (1.14)$$

$$\rho' = -3\mathcal{H}(\rho + p). \quad (1.15)$$

These equations are not independent and describe the evolution of FRW space-time and the fluid contained at background level. What is still missing, though, is an equation of state for the fluid, namely a relation between energy density and pressure usually parametrized as  $p = w\rho$ . For a radiation fluid it is well known that the state parameter is  $w = 1/3$  leading to an evolution for the scale factor proportional to conformal time ( $a(\eta) \propto \eta$ ). For dust, instead,  $w = 0$  and the scale factor evolves as  $a(\eta) \propto \eta^2$ . From continuity equation one can derive how energy density redshifts with the expansion; for a general time dependence of the state parameter one gets

$$\rho \propto a^{-3} \exp \left[ -3 \int w(a) d \log a \right]. \quad (1.16)$$

## 1.2 The Standard Big Bang model

The Hot Big Bang model is strongly supported by three observational evidences: the expansion shown by Hubble diagram, the Big Bang nucleosynthesis and the cosmic microwave background radiation. All of these three fundamental observations point towards an adiabatic expansion of the universe driven by radiation at early epoch, by zero pressure matter later on and by some unknown form of energy at recent time, called dark energy. The reason why we expect that different forms of energy drive the scale factor evolution is clear from Eq. (1.16): from a mixture of cosmological components fixed as initial conditions at the end of inflation, the energy density of each of them cools down according to its state parameter. By measuring the energy density at present time, thus, we are able to go back in time and try to constrain the physical conditions of the universe in the past.

The Hubble diagram shows the recession of galaxies due to expansion of the universe. Such recession is observable as a stretching of the wavelength of light emitted by galaxies and measured in terms of redshift, defined as

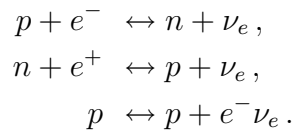
$$z \equiv \frac{a_0}{a} - 1 = \frac{\lambda_{\text{observed}}}{\lambda_{\text{emitted}}} - 1 \quad (1.17)$$

where  $a_0 = a(t_0)$  is the scale factor at present time<sup>2</sup>. Given a comoving distance  $x$  and the physical distance  $d = ax$ , the expansion induces a velocity,

$$v = \dot{d} = \dot{a}x = Hax = Hd, \quad (1.18)$$

proportional to the distance, being  $H$  the constant of proportionality. Since from doppler effect for low redshifts we have that  $z \simeq v/c$ , we expect to measure redshifts proportional to the distance of the object. This is what Hubble found [31] and what is shown from more recent measurements [32].

Big Bang nucleosynthesis leads to precise predictions on the abundances of light elements, depending on the baryon density. Protons and neutrons are kept in thermal equilibrium at temperature above 1 Mev by weak interaction through



Around  $T \sim 1$  Mev, though, the interactions above are no longer efficient enough and the relative abundance of neutrons and protons is frozen. From that time, neutrons and neutrinos fall out of thermal equilibrium. A small amount of deuterium can be formed at those temperatures through the interaction



but not much, being its binding energy of order 86 KeV. Afterwards, for  $T < 86$  KeV, although more deuterium nuclei could form from free neutrons and protons, they combine to give  $\text{He}^4$ , depending the rate on the baryon abundance. A very small amount of  $\text{He}^3$  and lithium is produced as well. The abundance of  $\text{He}^4$ , thus, depends mostly on the number of neutrons at  $T \sim 86$  KeV (which depends on the expansion rate), while the abundance of deuterium is an indicator of the how little is the amount of baryons. Constraints on abundance of light elements are given in Ref. (??).

The third observational pillar is the microwave background radiation. CMB radiation opens up a window to the physical conditions of the universe when it was just 300,000 years old, corresponding to  $z \sim 1090$ . Earlier than that time, the temperature of the plasma was high enough to keep photons and electrons strongly interacting mainly by Compton scattering, imprinting then a blackbody spectrum on radiation. Because of the Coulomb force between the electrons and the more massive protons, one can consider a

---

<sup>2</sup>We adopt  $a_0 = 1$

photon-baryon fluid. As universe expands and temperature falls off, efficiency of Compton interaction goes down as well and the universe becomes transparent to radiation which is free to propagate until the present time carrying the physical properties of the last scattering with matter. Since the energy density of a thermal bath of photons is proportional to the fourth power of its temperature, from Eq. (1.16) we see that

$$T(t) = \frac{T_0}{a(t)} \quad (1.20)$$

The relation above can also be derived from the simple argument that the wavelength of a photon in thermal equilibrium,  $\lambda = \hbar c/k_B T$ , stretches proportionally to  $a$  as the universe expands. We expect then to measure a blackbody isotropic radiation cooled down by expansion.

### 1.3 Theory of cosmological perturbations

The theory of cosmological perturbation [35, 36, 37, 38, 39] provides the framework for studying the growth of structures in the universe. The structures we observe today are thought to be generated by the gravitational instability mechanism starting from tiny perturbations present at very early times, produced from quantum fluctuations during inflation.

The starting point is a small perturbation of the metric tensor around its homogeneous part

$$g_{\mu\nu} = g_{\mu\nu}^{(0)} + \delta g_{\mu\nu} \quad (1.21)$$

where  $g_{\mu\nu}^{(0)}$  is the FRW metric,

$$g_{\mu\nu}^{(0)} = a^2(\eta) \begin{pmatrix} -1 & 0 \\ 0 & \gamma_{ij} \end{pmatrix}. \quad (1.22)$$

At first order, the metric tensor can be written as

$$\begin{aligned} \delta g_{00} &= -2a^2\psi \\ \delta g_{0i} &= \delta g_{i0} = a^2 B_i \\ \delta g_{ij} &= 2a^2 C_{ij}. \end{aligned} \quad (1.23)$$

Note that any 3-vector can be decomposed into a curl-free (constructed from a scalar) and a divergence free part. In the same way, a 3-tensor can be decomposed into its trace (scalar), the derivative of a 3-vector (with its curl-

and divergence-free contribution) plus a trace- and divergence-free tensor which can be neither constructed from scalars nor vectors. It follows that a decomposition of  $\delta g_{\mu\nu}$  into scalar, vector and tensor perturbations can be performed [40] by writing

$$\begin{aligned} B_i &= B_{,i} - S_i \\ C_{ij} &= -\phi\gamma_{ij} + E_{,ij} + F_{(i,j)} + \frac{1}{2}h_{ij}. \end{aligned} \quad (1.24)$$

With the notation above,  $\psi$ ,  $B$ ,  $\phi$  and  $E$  are scalars,  $S_i$  and  $F_i$  are (divergence-free) vectors and  $h_{ij}$  is the (trace- and divergence-free) tensor perturbation. The line element takes then the form

$$\begin{aligned} ds^2 &= a^2(\eta)[-(1 + 2\psi)d\eta^2 + 2(B_{,i} - S_i)d\eta dx^i \\ &\quad + ((1 - 2\phi)\gamma_{ij} + 2E_{,ij} + 2F_{i,j} + h_{ij}) dx^i dx^j]. \end{aligned} \quad (1.25)$$

Since the perturbations introduced above depend on the choice of the coordinate system, it is worth looking at how they change following a coordinate transformation. We consider a transformation

$$\tilde{x}^\mu = x^\mu + \xi^\mu \quad (1.26)$$

where, as stated before, the spatial part of  $\xi$  can be decomposed into a longitudinal and a transverse component  $\xi^i = \xi^{,i} + \bar{\xi}^i$  with  $\bar{\xi}_{,i} = 0$ . From the invariance of the line element under coordinate transformations ( $ds^2 = \tilde{d}s^2$ ), we get a relation between the two sets of perturbation variables:

$$\begin{aligned} \tilde{\psi} &= \psi - \mathcal{H}\xi^0 - \xi^{0'} \\ \tilde{\phi} &= \phi + \mathcal{H}\xi^0 \\ \tilde{B} &= B + \xi^0 - \xi' \\ E &= E - \xi \end{aligned} \quad (1.27)$$

for scalars,

$$\begin{aligned} \tilde{F}_i &= F_i - \bar{\xi} \\ \tilde{S}_i &= S_i + \bar{\xi}' \end{aligned} \quad (1.28)$$

for vectors and

$$\tilde{h}_{ij} = h_{ij} \quad (1.29)$$

for tensors. Tensor perturbations are then gauge invariant. Scalars and vectors instead are not gauge invariant quantities. Nonetheless some combination of them do, and precisely

$$\begin{aligned} \Phi &= \phi - \mathcal{H}(B - E') \\ \Psi &= \psi + \mathcal{H}(B - E') + (B - E) \end{aligned} \quad (1.30)$$

for the scalar sector and

$$\mathbf{V}_i = S_i + F'_i \quad (1.31)$$

for vectors.

What reviewed so far concerns metric perturbations. Let us write down now the energy-momentum tensor of a fluid in the most general form,

$$T^\mu{}_\nu = p\delta^\mu{}_\nu + (\rho + p)u^\mu u_\nu + \pi^\mu{}_\nu \quad (1.32)$$

where the anisotropic stress,  $\pi^\mu{}_\nu$ , has been added to Eq. (1.4) to account for free-streaming matter which is not properly described as perfect fluid. As seen, for the background we have

$$T^0{}_0 = -\rho_0, \quad T^0{}_i = 0, \quad T^i{}_j = \delta^i{}_j p_0 \quad (1.33)$$

while at first order in perturbations

$$\begin{aligned} T^0{}_0 &= -\delta\rho \\ T^i{}_0 &= -(\rho_0 + p_0)v^i \\ T^0{}_i &= (\rho_0 + p_0)(v_i + B_i) \\ T^i{}_j &= \delta p\delta^i{}_j + \pi^i{}_j \end{aligned} \quad (1.34)$$

where  $v^i$  is the spatial part of  $u^i$  and  $\pi^i{}_j$  can be splitted into its scalar ( $\pi$ ), vector ( $\pi_i$ ) and tensor ( $\Pi^i{}_j$ ) contribution as

$$\pi^i{}_j = \pi^i{}_j - \frac{1}{3}\nabla^2\pi\delta^i{}_j + \frac{1}{2}(\pi^i{}_{,j} - \pi_{j,i}) + \Pi^i{}_j \quad (1.35)$$

## 1.4 Characterizing radiation field

Relic radiation will be the center of this thesis. Before tackling any aspect of CMB anisotropies we need to fix some basic notion about how to describe a radiation field.

The intensity field  $I_{ij}$  in the 2-dimensional plane perpendicular to propagation direction can be decomposed into

$$I_{ij} = \begin{pmatrix} T + Q & U \\ U & T - Q \end{pmatrix} \quad (1.36)$$

where  $T$  is the temperature and  $Q$  and  $U$  are two Stokes parameters for linear polarization [33]. No circular polarization is taken into account since we do not expect Compton scattering to produce it at leading order.  $Q$  and  $U$  depend on the reference frame chosen in the plane perpendicular to

the propagation direction. A combination of the them, though, is invariant under rotation of the polarization plane and defines a vector of amplitude  $P = (Q^2 + U^2)^{1/2}$  and direction  $\alpha = (\arctan(U/Q))/2$  with respect to the  $x$  axis.

CMB photons appear to us as incoming radiation coming from any direction of the sky  $\hat{n}$ . We need to characterize the radiation field and to study its angular distribution on the sphere. Temperature is a scalar quantity and does not depend on the reference frame; it is natural then to expand it using spherical harmonics as orthonormal basis. This is not the case for  $Q$  and  $U$  quantities. However, spin-2 objects can be constructed out of them as  $Q \pm iU$ . This two combinations of linear polarization parameters can be expanded in two families of generalized spherical harmonics leading to

$$\begin{aligned} T(\hat{n}) &= \sum_{\ell,m} a_{T,\ell m} Y_{\ell m}(\hat{n}), \\ (Q \pm iU)(\hat{n}) &= \sum_{\ell,m} a_{\pm 2,\ell m \pm 2} Y_{\ell m}(\hat{n}). \end{aligned} \quad (1.37)$$

Although we might be happy with the description above, a different choice is usually made to describe the angular distribution of CMB. In fact, the quantities  $Q \pm iU$ , are not conserved under parity transformations. This property is not needed to represent the field onto the sphere but may be something we are interested in. It turns out that by defining

$$\begin{aligned} a_{E,\ell m} &= -(a_{2,\ell m} + a_{-2,\ell m})/2, \\ a_{B,\ell m} &= i(a_{2,\ell m} - a_{-2,\ell m})/2 \end{aligned} \quad (1.38)$$

they are the harmonic coefficients of non local (constructed in harmonic space, not in real space) quantities,  $E$  and  $B$ , which transform under parity as scalar and pseudo-scalar respectively. As  $B$ -modes change sign under parity transformation, they are not excited by linear scalar perturbation.

For each polarization  $X$ , the angular power spectrum is defined as the variance of the zero-mean distribution of the  $a_{\ell m}$  coefficients

$$\langle a_{\ell m} \rangle = 0, \quad \langle a_{\ell m} a_{\ell' m'} \rangle = \delta_{\ell \ell'} \delta_{m m'} C_{\ell}. \quad (1.39)$$

where the average is meant to be over an ensemble of realizations. The variance is independent of  $m$ , i.e. all the  $2\ell + 1$  coefficients for a given  $\ell$  have the same variance

$$C_{\ell}^{XX'} = \frac{1}{2\ell + 1} \sum_{m=-\ell}^{\ell} \langle a_{\ell,m}^{*X} a_{\ell,m}^{X'} \rangle. \quad (1.40)$$

This means that to draw the distribution of each  $C_\ell$  we have no more than  $2\ell + 1$  samples. Such a limitation is called *cosmic variance* and poses a fundamental uncertainty

$$\Delta C_\ell = C_\ell \sqrt{\frac{2}{2\ell + 1}}. \quad (1.41)$$

in the knowledge of the  $C_\ell$ .

## 1.5 CMB Temperature anisotropies

Accurate measurements of the microwave background show small deviations from a perfect isotropy of the radiation field. The origin of such anisotropies lies in primordial perturbations generated during inflation and grown afterwards throughout the whole history of the universe. We give now a brief review of the physics behind the inhomogeneities of the primordial radiation field, observed today as anisotropies, choosing the Newtonian gauge for the gravitational potentials.

The proper way of treating radiation is through the Boltzmann formalism. Boltzmann equation describes the phase space evolution of the distribution function of photons in presence or not of collisions between photons and other particles. We know that prior to decoupling between matter and radiation, a mechanism of interaction is provided by Compton scattering, which produces a time variation of phase space density. Its efficiency depends on the electron density ( $n_e$ ) and the optical depth of the plasma

$$\tau(\eta) \equiv \int_\eta^{\eta_0} d\eta' n_e \sigma_T a. \quad (1.42)$$

We also know that it introduces a non negligible angular dependence  $\propto (1 - \cos^2 \theta)$ , i.e. in the rest frame of electrons, outgoing radiation angular distribution has a small quadrupole moment.

Since the anisotropy we observe today are small we expect that linear regime for small temperature perturbations is appropriate for all their evolution. Although the time evolution of temperature fluctuation,  $\Theta$ , can be followed by feeding the evolution equation into Einstein-Boltzmann codes, a physical understanding of the anisotropies we observe can be reached through basic considerations and analytic results.

By moving to Fourier space and defining  $\mu = \hat{k} \cdot \hat{p}$ , the temperature fluctuation can be expanded in Legendre polynomials,  $P_\ell(\mu)$ , as

$$\Theta_\ell = \frac{1}{2(-i)^\ell} \int_{-1}^1 d\mu P_\ell(\mu) \Theta(\mu) \quad (1.43)$$

and Boltzmann equation is

$$\Theta' + ik\mu\Theta = -\phi' - ik\mu\psi - \tau' \left[ \Theta_0 - \Theta + \mu v_b - \frac{1}{2}P_2(\Theta_2 + \Theta_{P0} + \Theta_{P2}) \right] \quad (1.44)$$

One way of solving this equation is by turning it into a hierarchy of equations for each multipole  $\Theta_\ell$  through Eq. (1.43) and then integrate each of them over time and wavenumber. This approach is not exactly the one adopted by Einstein-Boltzmann codes but it is nonetheless useful to describe the physics of CMB anisotropies. For  $\ell \geq 2$ , we get that a good approximation for each multipole is

$$\Theta_\ell \sim \frac{k\eta}{2\tau} \Theta_{\ell-1} \quad (1.45)$$

In the regime of high optical depth, for modes comparable to the Hubble radius, ( $k\eta \sim 1$ ), we have therefore  $\Theta_\ell \ll \Theta_{\ell-1}$ . This leads to the fluid approximation for radiation: when interactions with matter are highly frequent, photons evolve like a fluid, described by its monopole (energy density) and dipole (velocity) equation,

$$\begin{aligned} \Theta'_0 + k\Theta_1 &= -\phi' \\ \Theta'_1 - \frac{k}{3}\Theta_0 &= \frac{k\psi}{3} + \tau' \left[ \Theta_1 - \frac{iv_b}{3} \right], \end{aligned} \quad (1.46)$$

being the higher order multipoles negligible. The two equations above can be written as a single second order for the monopole  $\Theta_0$ , a wave equation damped by baryonic matter and forced by gravitational potentials. Tight-coupling approximation holds until matter and radiation are strongly interaction and recombination of plasma to form the first atoms subtracts free electrons. So, prior to recombination, temperature inhomogeneities undergo oscillations with sound speed and typical length scale

$$c_s = (3(1+R))^{-1/2}, \quad r_s = \int_0^\eta d\eta' c_s(\eta') \quad (1.47)$$

where  $R$  is the baryon-photon energy density ration defined as  $R = 3\rho_b/4\rho_\gamma$ .

To solve these equations, the whole system of equations for the other components and metric perturbations is needed. An approximate analytic solution [42, 43] is

$$\begin{aligned} \Theta_\ell(k, \eta_0) &\simeq [\Theta_0(k, \eta_\star) + \psi(k, \eta_\star)] j_\ell[k(\eta_0 - \eta_\star)] \\ &+ 3\Theta_1(k, \eta_\star) \left( j_{\ell-1}[k(\eta_0 - \eta_\star)] - \frac{(l+1)j_\ell[k(\eta_0 - \eta_\star)]}{k(\eta_0 - \eta_\star)} \right) \\ &+ \int_0^{\eta_0} d\eta e^{-\tau} [\psi'(k, \eta) - \phi'(k, \eta)] j_\ell[k(\eta_0 - \eta_\star)] \end{aligned} \quad (1.48)$$

which shows that the anisotropies seen today in the radiation distribution are mainly due to the monopole and dipole at the time of matter recombination together with the gravitational potential  $\psi$  at the same epoch. There is then a smaller contribution coming from the integrated changing of gravitational potential until the present time, called integrated Sachs-Wolfe effect. Each Fourier mode is projected onto the sphere by the Bessel functions. Since  $\eta_0 \gg \eta_*$  and  $j_\ell(x)$  is strongly peaked at  $x \sim \ell$ , then a perturbation with wavenumber  $k$  is primarily responsible for anisotropies at angular scale

$$\ell \sim k\eta_0. \quad (1.49)$$

The angular oscillations we observe today as CMB anisotropies are (mainly) due to the projection of acoustic oscillations of temperature fluctuations at recombination onto the sphere.

## 1.6 CMB Polarization

As mentioned before, a small amount of polarization is expected to arise at the time of recombination because of Compton scattering. The evolution of a small polarization field, described by the Stokes parameters  $Q$  and  $U$ , can be treated in the same way as temperature fluctuation through the Boltzmann formalism. Instead of writing down the Boltzmann equation for  $Q$  and  $U$  we can write them as

$$\begin{aligned} Q(\mathbf{k}, \hat{n}) &= \Theta_P(\mu) \cos(\phi) \\ U(\mathbf{k}, \hat{n}) &= \Theta_P(\mu) \sin(\phi), \end{aligned} \quad (1.50)$$

and study the Boltzmann equation for  $\Theta_P(\mu)$ :

$$\Theta'_P + ik\mu\Theta_P = -\tau' \left[ -\Theta_P + \frac{1}{2}(1 - P_2(\mu))(\Theta_2 + \Theta_{P0} + \Theta_{P2}) \right]. \quad (1.51)$$

As the quadrupole of the polarization field appears in the Boltzmann equation for temperature (Eq. (1.44)), the contrary is also true: polarization is sourced by the quadrupole moment of temperature field. Following the same lines as before, a rather accurate analytical solution can be found for  $\Theta_{P\ell}$  at the present time,

$$\Theta_{P\ell}(k, \eta_0) \simeq \frac{5k\Theta_1(k, \eta_*)}{6\tau(\eta_*)} \frac{\ell^2}{(k\eta_0)^2} j_\ell(k\eta_0). \quad (1.52)$$

The solution above shows that the CMB polarization is small and out of phase compared to temperature (it depends on the opacity and is proportional to the temperature dipole at recombination). Further, there is no

integrated contribution due to changing potential. The same argument about the angular projection of temperature fluctuations still holds for polarization: the angular power spectrum we observe today is oscillating, being the projection through the Bessel functions of the oscillating polarization field at last scattering.

The two analytical solutions of the Boltzmann equation for temperature and polarization reported above give a feeling of the physics behind the CMB pattern we observe. The traditional approach for solving Boltzmann equation numerically consists of turning it into a set of coupled equations for each multipole and integrate each of them over time up to the present time [39]. An alternative method [44, 45], instead, goes through a formal integration of the Boltzmann equation along the line of sight and an angular decomposition of the solution. This approach is much faster than the previous one and is the one adopted by the CMBFAST [44] and CAMB [46] codes.

Fig. (1.1) shows in black the CMB power spectra due to scalar perturbations. Temperature,  $E$  polarization and  $TE$  cross-correlation are reported as solid, dotted and dot-dashed lines respectively. We also plot in red the same three spectra induced by tensor modes ( $r = 0.133$ ); although for each polarization the tensor contribution has a different behaviour with respect to the scalar one - and then they are in principle separable -, their amplitude is much lower. As mentioned before, scalar modes do not produce polarization  $B$ -modes at linear order, whereas tensors do (red dotted line). However, a scalar contribution to  $B$ -modes arises from lensing of  $E$ -modes (blue dotted line). It is a second order effect but of relevance for the detection of primordial  $B$ -modes because of the higher level of  $E$  polarization.

## 1.7 The *Planck* mission

The *Planck* satellite [19] is scheduled to be launched in April 2009 to reach the lagrangian point L2. It is the third generation space mission, after COBE/DMR and *WMAP*, devoted to image the CMB anisotropies. The *Planck* satellite is made of two instruments: the Low Frequency Instrument (LFI) and the High Frequency Instruments (HFI). The Low Frequency Instrument [47] will observe the sky at three frequency bands centered at 30, 44 and 70 GHz with a FWHM angular resolution of 33, 27 and 13, respectively. It is composed by 11 pseudo-correlation receivers, actively cooled to 20 K, able to detect both orthogonal polarisations of the incoming signal. LFI and HFI are located in the focal region of a 1.5 m aperture telescope. While *WMAP* is not sensitive at frequency higher than 90 GHz, the instru-

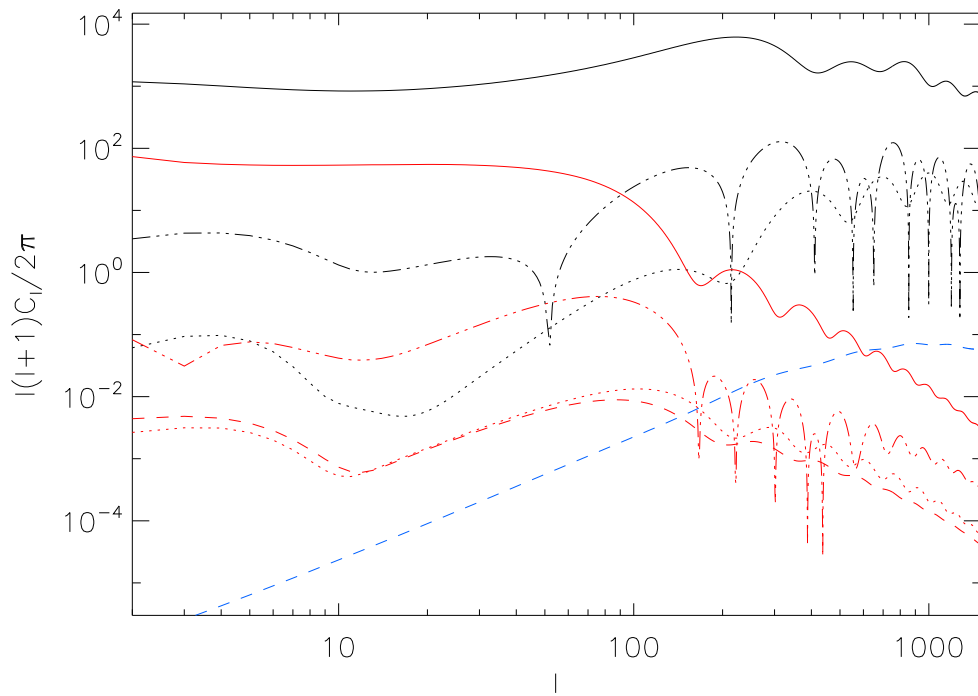


Figure 1.1: TT (solid), EE (dotted), TE (dot-dashed) angular power spectra from scalar (black) and tensor (red) perturbations. The red dashed line is the B contribution from tensors. The blue dashed line is the B-mode induced by lensing.

ments aboard the *Planck* satellite will produce cross-calibrated full sky maps spanning a very large frequency range. This will give a higher control of the foreground emissions. The High Frequency Instruments [48] will observe the sky at six frequency bands, centered at 100, 143, 217, 353, 545 and 857 GHz; it will be able then to monitor, for instance, the contamination from dust emission, whereas the Low Frequency Instrument is sensitive to the galactic synchrotron and free-free emission. The combination of the two instruments will therefore produce the cleanest image of the CMB anisotropies ever obtained. Moreover, the wide frequency range covered, delivering all-sky maps for each channel, will provide at the same time a gold-mine of astrophysical information.

After the first detection of CMB temperature anisotropies, more accurate measurements of the temperature angular power spectrum up to the third peak have been obtained by the *WMAP* satellite, together with an improvement of TE and EE measurements. With its better sensitivity and angular resolution, *Planck* is expected to improve the already measured spectra and has a chance of detecting primordial *B*-modes. For a detailed discussion of the *Planck* capabilities, we refer the reader to the *Planck* Scientific Program [94].



# Chapter 2

## Gravitational waves background

Whereas a certain amount of primordial scalar perturbations with a nearly scale invariant spectrum is in good agreement with CMB temperature and polarization anisotropies and the large scale structure we observe today, there is no direct evidence of vector and tensor perturbations. Relying on inflation or alternative models which solve the horizon problem to generate the primordial spectrum of perturbations, the classical perturbations we see in the CMB derive from geometrical amplification of quantum fluctuation. The amplitude of primordial gravitational waves carries information on the scale at which the early stage which solved the horizon problem took place. Moreover tensors propagate as waves whatever the content of the universe is. For this reason if tensor perturbations have been excited and their amplitude is high enough, CMB experiments should be able to detect them through their distinctive imprints onto CMB anisotropies.

### 2.1 GW in Robertson-Walker metric

Let us consider the following action for gravity and matter

$$S \equiv \int d^4x (\mathcal{L}_g + \mathcal{L}_m) = \int d^4x \left[ \sqrt{-g} \frac{R}{16\pi G} + \mathcal{L}_m \right] \quad (2.1)$$

and a metric tensor

$$g_{\mu\nu} = g_{\mu\nu}^{(0)} + h_{\mu\nu} \quad (2.2)$$

where  $h_{\mu\nu}$  is a small perturbation to the flat Robertson-Walker metric  $g_{\mu\nu}^{(0)}$ .

In the synchronous gauge, the  $g_{00}$  and  $g_{0i}$  components are zero by definition and the line element takes the form

$$ds^2 = a^2(\tau)[-d\eta^2 + (\delta_{ij} + h_{ij}(\mathbf{x}, \eta))dx^i dx^j] \quad (2.3)$$

According to Eq. (2.1), small perturbations evolve at linear order according to linearized Einstein equations

$$\delta \left[ R_{\mu\nu} - \frac{1}{2} R g_{\mu\nu} \right] = 8\pi G \delta T_{\mu\nu} \quad (2.4)$$

where the energy-momentum tensor can be computed for each cosmological component by integrating the distribution function over the momentum space.

We are not interested now in a complete and exhaustive study of cosmological perturbations, being this chapter devoted to tensors. For this reason we will mean by  $h_{\mu\nu}$  just its tensorial contribution, avoiding in this way to carry all around any other index.

Gravitational waves are represented by the transverse and traceless part of the spatial metric perturbation,

$$\partial_i h_{ij} = h_{ii} = 0, \quad (2.5)$$

which evolve according to the equation of motion

$$h''_{ij} + 2\mathcal{H}h'_{ij} - \nabla^2 h_{ij} = 16\pi G a^2 \Pi_{ij}, \quad (2.6)$$

where  $\Pi_{ij}$  is the transverse ( $\partial_i \Pi_{ij} = 0$ ) and traceless ( $\Pi_{ii} = 0$ ) part of the energy momentum tensor.

Let us perform a Fourier expansion and consider the two polarization states  $h_+$  and  $h_\times$

$$h_{ij}(\mathbf{x}, \eta) = \frac{1}{(2\pi)^3} \int d\mathbf{k} e^{i\mathbf{k}\cdot\mathbf{x}} [h_+ e_{ij}^+ + h_\times e_{ij}^\times] \quad (2.7)$$

where  $e_{ij}^+$  and  $e_{ij}^\times$  are the two symmetric polarization tensors which have the following properties:

$$\begin{aligned} k^i e_{ij}^+ &= k^i e_{ij}^\times = 0, & e_i^{+,i} &= e_i^{\times,i} = 0, \\ e_{ij}^+ e^{+,ij} &= e_{ij}^\times e^{\times,ij} = 2, & e_{ij}^+ e^{\times,ij} &= 0. \end{aligned} \quad (2.8)$$

By making use of the same polarization tensors to project the energy-momentum tensor which sources gravitational waves, two Fourier amplitudes  $\Pi_+$  and  $\Pi_\times$  can be defined as well, leading us to the Fourier equation for each polarization state  $+$  and  $\times$ ,

$$h''_k + 2\mathcal{H}h'_k + k^2 h_k = 16\pi G a^2 \Pi_k. \quad (2.9)$$

## 2.2 Inflationary spectrum

The simplest way of driving an inflationary expansion is through a scalar field. Since the energy-momentum tensor associated to scalar fields does not carry anisotropic pressure, tensor evolution equation has no source term during the inflationary stage, just as if propagation would be in vacuum,

$$h_k'' + 2\mathcal{H}h_k' + k^2 h_k = 0. \quad (2.10)$$

By approximating the inflationary stage as pure de-Sitter space-time the time evolution of the scale factor is given by  $a(\eta) = -(H\eta)^{-1}$ . To solve the evolution equation for tensor modes is useful to make use of the quantity  $v_k = M_{\text{pl}} a h_k / \sqrt{2}$ , solve for it and go back to the tensor amplitude  $h_k$ . Eq. (2.10) for  $v_k$  reads

$$v_k'' + \left( k^2 - \frac{a''}{a} \right) v_k = 0, \quad (2.11)$$

which, since in de-Sitter space-time  $a''/a = 2/\eta^2$ , can be written as

$$v_k'' + \left( k^2 - \frac{2}{\eta^2} \right) v_k = 0. \quad (2.12)$$

and has solution

$$v_k = \frac{e^{-ik\eta}}{\sqrt{2k}} \left[ 1 - \frac{i}{k\eta} \right] \quad (2.13)$$

Going back to  $h_k$ , in the limit of small  $k|\eta|$ , corresponding to super-horizon gravitational waves, Eq. (2.13) reduces to

$$h_k = \frac{H}{M_{\text{pl}}} i e^{-ik\eta} k^{-3/2} \quad (2.14)$$

which is time independent and leads, as well known, to a scale-free power spectrum

$$\mathcal{P}_h(k) \equiv \frac{k^3}{\pi^2} (|h_+|^2 + |h_\times|^2) = \frac{2H^2}{\pi^2 M_{\text{pl}}^2} \quad (2.15)$$

However, inflationary phase is expected to slightly deviate from pure de-Sitter expansion, being  $H$  time-dependent. As consequence, a small  $k$ -dependence in the power spectrum is introduced, usually parametrized as

$$\mathcal{P}_h(k) = \mathcal{P}_h(k_0) \left( \frac{k}{k_0} \right)^{nt}, \quad (2.16)$$

where  $k_0$  is a pivot scale and the spectral index is related to the time derivative of the Hubble parameter at horizon crossing and then to the first slow-roll parameter,  $\epsilon \equiv -H'/(aH^2)$ , as

$$n_t = \frac{2H'}{aH^2}|_{k=aH} = -2\epsilon. \quad (2.17)$$

To connect the amplitude of primordial tensor modes to the scalar spectrum, a tensor-scalar ratio is defined as follows

$$r = \frac{\mathcal{P}_h(k_0)}{\mathcal{P}_\mathcal{R}(k_0)}, \quad (2.18)$$

which turns out to be related to  $n_t$ , in single-field inflationary models, via the so-called consistency relation,

$$r = -8n_t = 2\epsilon. \quad (2.19)$$

### 2.2.1 Post inflationary evolution

Also after the end of inflation, throughout radiation- and matter-dominated epoch, if free-streaming particles are absent, the homogeneous approximation in Eq. (2.10) for gravitational waves evolution still holds. This is due to the fact that the content of the universe is pretty well described in terms of perfect fluids. When radiation drives the expansion of the universe, the time-dependence of the scale factor is  $a(\eta) \propto \eta$ . For matter-dominated epoch instead, it is quadratic ( $a(\eta) \propto \eta^2$ ). The solution of the wave equation (2.10) in the two regimes is

$$\begin{aligned} h_k^{(\text{rad})} &\propto j_0(k\eta) = \frac{\sin(k\eta)}{k\eta} \\ h_k^{(\text{mat})} &\propto \frac{j_1(k\eta)}{k\eta} = \frac{\sin(k\eta)}{(k\eta)^3} - \frac{\cos(k\eta)}{(k\eta)^2} \end{aligned} \quad (2.20)$$

where  $j_0$  and  $j_1$  are the spherical Bessel functions of first and second order respectively.

When free-streaming particles are present the above description fails; free streaming particles do carry anisotropic pressure and therefore act at the right hand side in the wave equation for tensors. Responsible for this are in particular neutrinos, which free-stream at the energy scale of 1 MeV, well above the time at which perturbations are initialized in Einstein-Boltzmann codes. Since the current upper bound on neutrino mass constrain it below 1 eV [58, 59, 56], they drove the expansion in the radiation-dominated

era together with photons, which were tightly coupled to baryons through Compton scattering. Such a strong interaction, absent for neutrinos, prevent photons to develop anisotropic pressure. The result is that neutrinos do free-streaming during radiation-dominated era whereas photons not. During matter-dominated era both of them carry anisotropic stress but are subdominant. Only the small residual fraction of photons at the decoupling epoch, when Compton ceases holding them tied to baryons, may lead to a significant contribution. However, neutrino mass plays also a role: massive neutrinos are less subdominant than radiation at the early stage of matter-dominated era, and in particular when CMB photons last scatter. The density parameter for massive neutrinos can be written as

$$\Omega_\nu = \frac{\sum_i m_i}{93.14 h^2 \text{eV}} \quad (2.21)$$

where  $h^2$  is the present value of the Hubble parameter in units of  $100 \text{ km s}^{-1} \text{ Mpc}^{-1}$  and the sum is meant over the neutrino states. In the next sections we will study in some details the effect of free-streaming neutrinos on the evolution of gravitational waves, together with the impact of primordial magnetic fields on tensors.

## 2.3 Interaction with non collisional matter

The evolution of phase space distribution for non collisional matter is driven by the homogeneous Boltzmann equation

$$\frac{\partial f}{\partial \tau} + \frac{dx^i}{d\tau} \frac{\partial f}{\partial x^i} + \frac{dP_j}{d\tau} \frac{\partial f}{\partial P_j} = 0, \quad (2.22)$$

where  $P_j$  is the canonical conjugate momentum of the comoving coordinate  $x^i$ . We define, according to the literature [106], a new momentum variable,  $q_j = qn_j$ , (with  $n^i n_i = 1$ ) related to  $P_i$  by

$$P_i = \left[ \delta_{ij} + \frac{1}{2} h_{ij} \right] q^j, \quad (2.23)$$

and expand the distribution function at first order around its homogeneous part,

$$f(\tau, x^i, q_j) = f_0(q) \left[ 1 + \Psi(\tau, x^i, q_j) \right], \quad (2.24)$$

The phase space density of the particles is described at 0-th order by the Fermi-Dirac distribution function (ignoring any chemical potential),

$$f_0(\epsilon) = \frac{g_s}{h_P^3} \frac{1}{e^{\epsilon/K_B T_0} + 1}, \quad (2.25)$$

where  $\epsilon = (q^2 + a^2 m^2)^{1/2}$  is the energy of the particles,  $T_0$  is the temperature today,  $g_s$  is number of degrees of freedom,  $h_P$  and  $K_B$  are the Planck and Boltzmann constant respectively.

The energy-momentum tensor is then defined through the following integrals over momentum space:

$$\begin{aligned} T^0_0 &= -a^{-4} \int q^2 dq d\Omega \epsilon f_0(q) (1 + \Psi) \\ T^0_i &= a^{-4} \int q^2 dq d\Omega q n_i f_0(q) \Psi \\ T^i_j &= a^{-4} \int q^2 dq d\Omega \frac{q^2}{\epsilon} n^i n_j f_0(q) (1 + \Psi). \end{aligned} \quad (2.26)$$

In a fluid description, homogenous energy density and pressure are

$$\bar{\rho} = a^{-4} \int q^2 dq d\Omega \epsilon f_0(q), \quad \bar{p} = \frac{1}{3} a^{-4} \int q^2 dq d\Omega \frac{q^2}{\epsilon} f_0(q), \quad (2.27)$$

while at first order in the perturbations we have

$$\begin{aligned} \delta\rho &= a^{-4} \int q^2 dq d\Omega \epsilon f_0(q) \Psi \\ \delta p &= \frac{1}{3} a^{-4} \int q^2 dq d\Omega \frac{q^2}{\epsilon} f_0(q) \Psi \\ \delta T^0_i &= a^{-4} \int q^2 dq d\Omega q n_i f_0(q) \Psi \\ \Sigma^i_j &= a^{-4} \int q^2 dq d\Omega \frac{q^2}{\epsilon} (n^i n_j - \frac{1}{3} \delta^i_j) f_0(q) \Psi \end{aligned} \quad (2.28)$$

In this notation,  $\Sigma^i_j = T^i_j - \delta^i_j T^k_k / 3$  denotes the anisotropic stress, the trace-free component of  $T^i_j$ .

We want to write down Boltzmann equation at first perturbative order explicitly. To do this, we make use of the time derivative of the phase space coordinate

$$\begin{aligned} \frac{dx^i}{d\eta} &= \frac{q}{\epsilon} n^i \\ \frac{dq}{d\eta} &= -\frac{1}{2} q h'_{ij} n^i n^j \end{aligned} \quad (2.29)$$

Any first order term in position derivative is ignored because  $f_0$  does not depend on position and therefore their product is null. Any variation of

momentum direction is ignored as well, since it is first order and would lead to second order term in Boltzmann equation.

By fixing a spherical coordinate system with the polar axis along the  $\hat{k}$  direction, the momentum direction  $\hat{n}$  is described by two angles  $(\theta, \phi)$ ,

$$(\hat{k} \cdot \hat{n}) = \cos \theta, \quad (2.30)$$

$$(e_{ij}^+ + e_{ij}^\times) n^i n^j = \sin^2 \theta (\sin 2\phi - \cos 2\phi) \quad (2.31)$$

and the Boltzmann equation at first order reads

$$\frac{\partial \Psi}{\partial \eta} + ik \frac{q}{\epsilon} \cos \theta \Psi + \frac{1}{2} \frac{d \ln f_0}{d \ln q} \left[ h'_+ \sin^2 \theta \cos 2\phi - h'_\times \sin^2 \theta \sin 2\phi \right] = 0. \quad (2.32)$$

Moreover, we wish to perform an angular expansion of  $\Psi$  on the sphere and convert Boltzmann equation into a hierarchy of coupled equations for the moments. We perform the following angular expansion,

$$\Psi = \sqrt{2\pi} \sum_{\ell, m} (-i)^\ell \sqrt{2\ell + 1} \frac{\sqrt{(\ell - m)! (\ell + m)!}}{\ell!} Y_{\ell, m} \Psi_{\ell, m}. \quad (2.33)$$

With this choice, the hierarchy for tensor moments is

$$\begin{aligned} \Psi'_{2, \pm 2} &= -\frac{k}{3} \frac{q}{\epsilon} \Psi_{3, \pm 2} + \frac{1}{15\sqrt{2}} \frac{d \ln f_0}{d \ln q} (h'_+ \pm ih'_\times) \\ \Psi'_{\ell, \pm 2} &= \frac{k}{2\ell + 1} \frac{q}{\epsilon} \left[ \ell \Psi_{\ell-1, \pm 2} - \frac{(\ell + 3)(\ell - 1)}{\ell + 1} \Psi_{\ell+1, \pm 2} \right], \quad \ell > 2 \end{aligned} \quad (2.34)$$

Defining the two circular polarization tensors [104] as

$$e_{ij}^R = \frac{1}{\sqrt{2}} (e_{ij}^+ + ie_{ij}^\times), \quad e_{ij}^L = \frac{1}{\sqrt{2}} (e_{ij}^+ - ie_{ij}^\times), \quad (2.35)$$

Einstein equations for each circular polarization state take the form

$$h_k'' + 2\mathcal{H}h_k' + k^2 h_k = 16\pi G a^2 \Pi_k \quad (2.36)$$

with

$$\Pi_k = 2a^{-4} \int dq \frac{q^4}{\epsilon} f_0(q) \Psi_{2, \pm 2}, \quad (2.37)$$

To consider the massless case, which corresponds to particles with  $\epsilon = q$ , we formally integrate  $\Psi$  over momentum space and define

$$F = \frac{\int dq q^3 f_0(q) \Psi}{\int dq q^3 f_0(q)} = \sqrt{2\pi} \sum_{\ell, m} (-i)^\ell \sqrt{2\ell + 1} \frac{\sqrt{(\ell - m)! (\ell + m)!}}{\ell!} Y_{\ell, m} F_{\ell, m}, \quad (2.38)$$

The hierarchy for  $F$  turns out to be

$$\begin{aligned} F'_{2,-2} &= -\frac{k}{3}F_{3,-2} - \frac{4}{15}h'_R \\ F'_{2,2} &= -\frac{k}{3}F_{3,2} - \frac{4}{15}h'_L \\ F'_{\ell,\pm 2} &= \frac{k}{2\ell+1} \left[ \ell F_{\ell-1,\pm 2} - \frac{(\ell+3)(\ell-1)}{\ell+1} F_{\ell+1,\pm 2} \right], \quad \ell > 2 \end{aligned} \quad (2.39)$$

and the Einstein equations read

$$h''_k + 2\mathcal{H}h'_k + k^2h_k = 16\pi G a^2 \Pi_k \quad (2.40)$$

with

$$\Pi_k = \bar{\rho}_\nu F_{2,\pm 2}. \quad (2.41)$$

Written explicitly for each polarization state they are

$$\begin{aligned} h''_R + 2\mathcal{H}h'_R + k^2h_R &= 16\pi G a^2 \bar{\rho}_\nu F_{2,-2} \\ h''_L + 2\mathcal{H}h'_L + k^2h_L &= 16\pi G a^2 \bar{\rho}_\nu F_{2,2} \end{aligned} \quad (2.42)$$

## 2.4 Relation with Weinberg's integro-differential equation

We want now to compare Eqs. (2.42) with integro-differential equation obtained by Weinberg [51] and furtherly deeply studied [52, 53, 54], to show that shortly after neutrino decoupling the two approaches lead to the same result.

The equation we refer to is Eq. (D23) of [54]

$$h''_k + 2\mathcal{H}h'_k + k^2h_k = -24f_\nu \mathcal{H}^2 \int_{\eta_{\nu dec}}^{\eta} d\eta' \left[ \frac{j_2[k(\eta - \eta')]}{k^2(\eta - \eta')^2} \right] h'_k \quad (2.43)$$

where  $f_\nu = \bar{\rho}_\nu/\bar{\rho}_{tot}$  is fractional neutrino energy density and  $j_2$  is the spherical Bessel function of order 2. In the limit of  $k(\eta - \eta') \rightarrow 0$  the kernel in the integral is  $1/15$  and, using Friedmann equation,

$$\mathcal{H}^2 = \frac{8\pi G}{3} \bar{\rho}_{tot} a^2, \quad (2.44)$$

it is easy to obtain

$$h''_k + 2\mathcal{H}h'_k + k^2h_k = -\frac{64\pi G}{15} \bar{\rho}_\nu a^2 [h_k(\eta) - h_k(\eta_{\nu dec})] \quad (2.45)$$

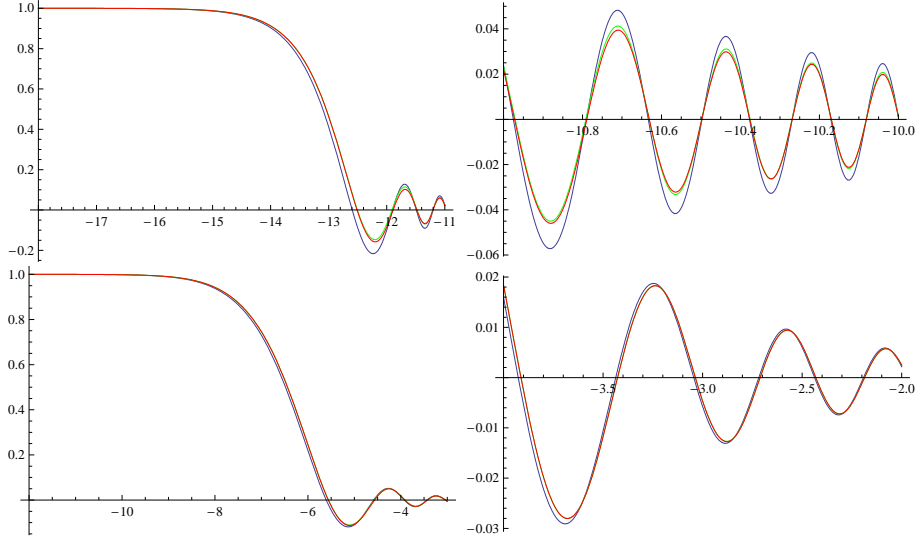


Figure 2.1: Evolution on  $h_k(\eta)$  for  $k = 2 \text{ Mpc}^{-1}$  (top) and  $k = 5 \times 10^{-3} \text{ Mpc}^{-1}$  (bottom). Blue lines show the homogeneous evolution, green lines the evolution with  $F_{3,\pm 2} = 0$  and red lines the evolution with  $F_{5,\pm 2} = 0$ . The two plots on the left show the horizon crossing of the fluctuations, whereas the right ones the oscillatory phase. (Figure produced with *Mathematica*).

On the other hand, let us consider Eqs. (2.46) and the case in which the moments with  $m = \pm 2$  and  $\ell \geq 3$  are zero,

$$\begin{aligned} F'_{2,-2} &= -\frac{4}{15} h'_R \\ F'_{2,2} &= -\frac{4}{15} h'_L \end{aligned} \tag{2.46}$$

Integrating from  $\tau_{\nu dec}$  and feeding the result into the right hand side of Eq. (2.42) it is immediate to recover Eq. (2.45). A truncation of the hierarchy as sharp as the one above turns out not to be suitable for precise numerical calculation. However, as illustrated in Fig. (2.1), it is not too far from a more accurate treatment which includes further multipoles. Two Fourier modes are shown adopting two different truncations as explained in the caption. Furthermore, as discussed in [26] and shown in Fig. (2.1), free-streaming neutrinos significantly modify the evolution of modes which enter the horizon during radiation-dominated epoch, whereas are almost negligible for modes which cross the horizon later, during matter-dominated epoch.

The impact of neutrino damping on  $B$ -mode angular power spectrum is

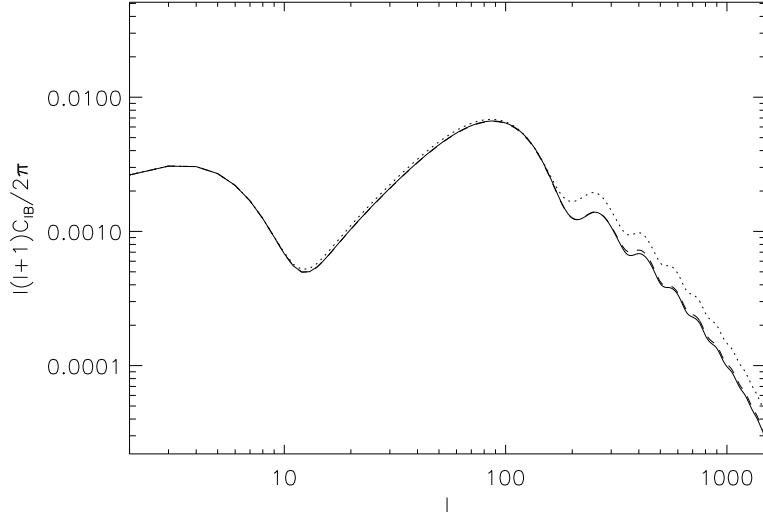


Figure 2.2: Damping of tensor modes due to massless neutrinos with hierarchy truncated at  $F_{3\pm 2}$  (dashed) and at  $F_{6\pm 2}$  (solid), compared to the case of no-anisotropic stress induced by neutrinos (dotted). As seen for each Fourier mode, different truncations of the neutrino hierarchy have small impact on the power spectrum.

shown in Fig.(2.2) for two different truncations of the neutrino hierarchy, as explained in the caption. The effect of considering more multipoles in the neutrino hierarchy is small, consistently with what we saw for each Fourier mode.

In the top panel of Fig (2.3), instead, is shown the case of massive neutrinos for two neutrino masses compared to the massless case. The highest mass of the two corresponds to the current upper limit from *WMAP* [56], under the assumption of three equal mass families. A very high neutrino mass is considered in the bottom panel to emphasise the effect. Of course, by feeding a high neutrino mass the background cosmology changes.

## 2.5 Interaction with primordial magnetic fields

In this section we include a stochastic background of primordial magnetic fields (PMF) in our treatment [64, 62]. Since they carry anisotropic stress beside energy, one expects an impact due to their presence on tensors evolution. Our results on the interaction of primordial magnetic fields with scalars

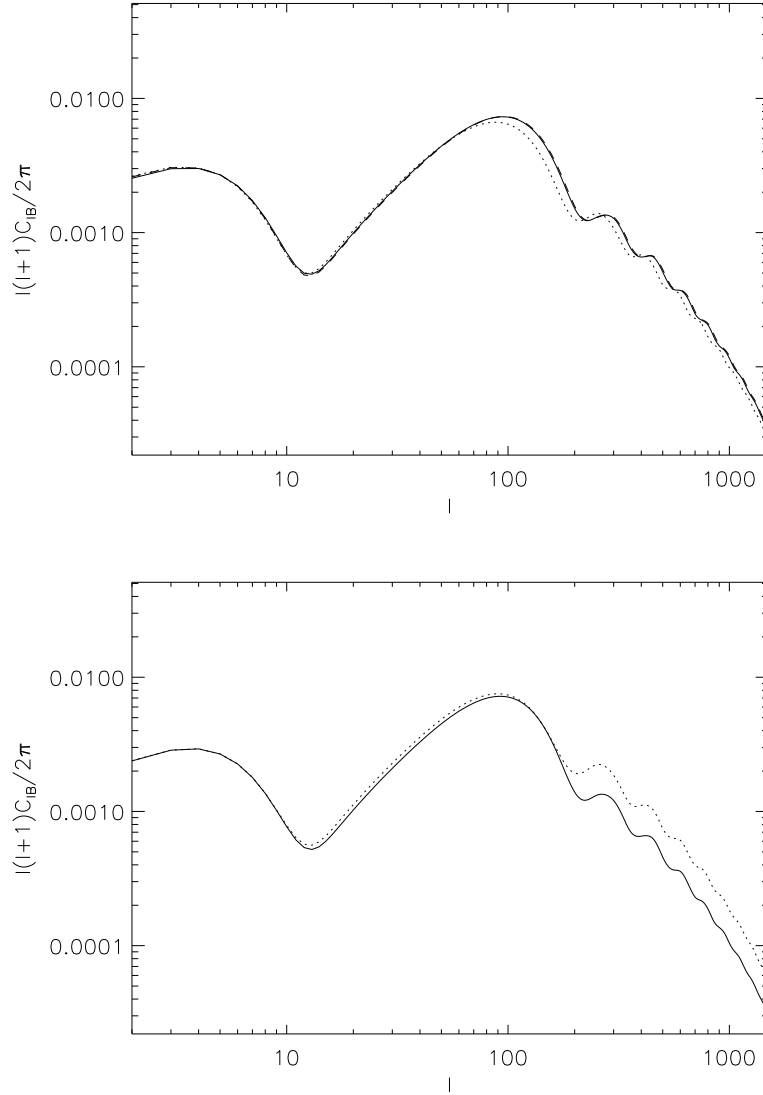


Figure 2.3: Top:  $B$ -modes in the presence of massive neutrinos with  $m_\nu = 0.065$  eV (dashed) and at  $m_\nu = 0.22$  eV (solid), compared to the massless case (dotted). Bottom:  $B$ -modes with (solid) and without (dotted) interaction of gravitational waves with neutrinos. A large mass of  $m_\nu = 0.67$  eV has been used to increase the effect

and vectors [63, 64] are summarized in appendix A.

Before the decoupling epoch the electric conductivity of the primordial plasma is very large. Therefore, we are allowed at first order to assume the infinite conductivity limit, in which the induced electric field is zero. Within such a limit, the magnetic field amplitude scales as  $\mathbf{B}(\mathbf{x}, \eta) = \mathbf{B}(\mathbf{x})/a(\eta)^2$  and the EMT of a SB of PMF is:

$$\begin{aligned}\tau_0^0 &= -\rho_B = -\frac{B^2(\mathbf{x})}{8\pi a^4} \\ \tau_i^0 &= 0 \\ \tau_j^i &= \frac{1}{4\pi a^4} \left( \frac{B^2(\mathbf{x})}{2} \delta_j^i - B_j(\mathbf{x}) B^i(\mathbf{x}) \right)\end{aligned}\quad (2.47)$$

The two point correlation function in Fourier space for fully inhomogeneous fields is:

$$\langle B_i(\mathbf{k}) B_j^*(\mathbf{k}') \rangle = (2\pi)^3 \delta(\mathbf{k} - \mathbf{k}') (\delta_{ij} - \hat{k}_i \hat{k}_j) \frac{P_B(k)}{2}, \quad (2.48)$$

where  $P_B(k)$  is the power spectrum parametrized as a power-law with respect to a certain scale  $k_*$ :

$$P_B(k) = A \left( \frac{k}{k_*} \right)^{n_B}. \quad (2.49)$$

PMF are damped on small scales by radiation viscosity. We model this damping introducing a sharp cut-off in the PMF power spectrum at a damping scale called  $k_D$ . To calculate the relation between the amplitude of PMF power spectrum and the amplitude of the fields themselves we evaluate the two point correlation function in the coincidence limit,

$$\langle B^2 \rangle = \langle B_i^*(\mathbf{x}') B_i(\mathbf{x}) \rangle |_{\mathbf{x}'=\mathbf{x}} = \frac{1}{2\pi^2} \int_0^{k_D} dk k^2 P_B(k) = \frac{A}{2\pi^2(n_B + 3)} \frac{k_D^{n_B+3}}{k_*^{n_B}}, \quad (2.50)$$

where for the convergence of the integral above  $n_B > -3$  is requested. Note that no gaussian smearing has been adopted in the definition of the magnetic field amplitude, being any ultraviolet divergence removed by introducing the cut-off  $k_D$ .

As shown by Eq. (2.47), the EMT of PMF is quadratic in the magnetic field and therefore its Fourier transform is a convolution. The two point correlation function of the spatial part of EMT is:

$$\begin{aligned} \langle \tau_{ab}^*(\mathbf{k}) \tau_{cd}(\mathbf{k}') \rangle &= \frac{1}{64\pi^5} \int d\mathbf{q} d\mathbf{p} \delta_{ab} \delta_{cd} \langle B_l(\mathbf{q}) B_l(\mathbf{k} - \mathbf{q}) B_m(\mathbf{p}) B_m(\mathbf{k}' - \mathbf{p}) \rangle \\ &\quad - \frac{1}{32\pi^5} \int d\mathbf{q} d\mathbf{p} \langle B_a(\mathbf{q}) B_b(\mathbf{k} - \mathbf{q}) B_c(\mathbf{p}) B_d(\mathbf{k}' - \mathbf{p}) \rangle \end{aligned} \quad (2.51)$$

To extract the tensor contribution out of the expression above we make use of the quantities  $P_{ij} = \delta_{ij} - \hat{k}_i \hat{k}_j$  and  $\mathcal{M}_{ijkl} = P_{ik} P_{jl} + P_{il} P_{jk} - P_{ij} P_{kl}$ , getting

$$\begin{aligned} \langle \Pi_{ij}^{*B}(k) \Pi_{il}^B(k') \rangle &= \left( P_{ia}(k) P_{jb}(k) - \frac{1}{2} P_{ij}(k) P_{ab}(k) \right) \times \\ &\quad \left( P_{tc}(k') P_{ld}(k') - \frac{1}{2} P_{kl}(k') P_{cd}(k') \right) \langle \tau_{ab}^*(k) \tau_{cd}(k') \rangle \\ &= \frac{1}{4} |\Pi^B(k)|^2 \mathcal{M}_{ijil}(k) \delta(k - k') \end{aligned} \quad (2.52)$$

where

$$|\Pi^B(k)|^2 = \frac{1}{512\pi^5} \int d\mathbf{p} P_B(p) P_B(|\mathbf{k} - \mathbf{p}|) (1 + 2\gamma^2 + \gamma^2 \beta^2) \quad (2.53)$$

with  $\gamma = \hat{\mathbf{k}} \cdot \hat{\mathbf{p}}$ ,  $\beta = \mathbf{k} \cdot (\mathbf{k} - \mathbf{p}) / (k|\mathbf{k} - \mathbf{p}|)$ .

We perform the exact calculation of  $|\Pi^B(k)|^2$  for many spectral indices [64]. We limit here to provide the analytic form of the spectrum for two cases,  $n_B = 2$  and  $n_B = -5/2$ ,

$$\begin{aligned} |\Pi^B(k)|_{n_B=2}^2 &= \frac{A^2 k_D^7}{256\pi^4 k_*^4} \left[ \frac{8}{15} - \frac{7\tilde{k}}{6} + \frac{16\tilde{k}^2}{15} - \frac{7\tilde{k}^3}{24} - \frac{13\tilde{k}^5}{480} + \frac{11\tilde{k}^7}{1920} \right], \\ |\Pi^B(k)|_{n_B=-5/2}^2 &= \frac{A^2 k_*^5}{256\pi^4 k_D^2} \left[ \frac{1984}{5775\sqrt{|1-\tilde{k}|}} + \frac{512}{1155\tilde{k}^5} - \frac{512}{1155\sqrt{|1-\tilde{k}|\tilde{k}^5}} + \right. \\ &\quad \left. + \frac{256}{1155\sqrt{|1-\tilde{k}|\tilde{k}^4}} + \frac{64}{105\tilde{k}^3} - \frac{128}{231\sqrt{|1-\tilde{k}|\tilde{k}^3}} + \right. \\ &\quad \left. + \frac{117728}{5775\sqrt{|1-\tilde{k}|\tilde{k}^2}} + \frac{28}{3\tilde{k}} - \frac{37088}{1925\sqrt{|1-\tilde{k}|\tilde{k}}} + \right. \\ &\quad \left. + \frac{2\tilde{k}}{5} - \frac{3968\tilde{k}}{5775\sqrt{|1-\tilde{k}|}} + \frac{\tilde{k}^3}{100} \right], \end{aligned} \quad (2.54)$$

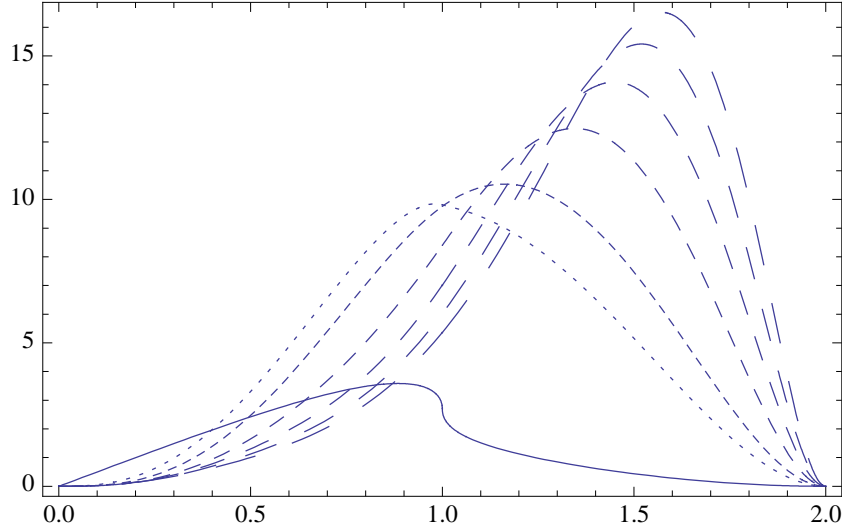


Figure 2.4: Plot of  $k^3|\Pi_{ij}^B(k)|^2$  in units of  $\langle B^2 \rangle^2/(1024\pi^3)$  versus  $k/k_D$  for different  $n_B$  for fixed  $\langle B^2 \rangle$ . The different lines are for  $n_B = -5/2, -3/2, -1, 0, 1, 2, 3$  ranging from the solid to the longest dashed.

and show the behaviour of the same quantity for all the spectral indices considered (Fig. (2.4)).

In the presence of PMF, the evolution equation for the metric tensor perturbation  $h_{ij}$  is:

$$h''_{ij} + 2\mathcal{H}h'_{ij} + k^2h_{ij} = 16\pi Ga^2(\Pi'_{ij} + \Pi_{ij}^B). \quad (2.55)$$

which, for each polarization state deep in radiation era reads

$$h''_k + \frac{2}{\eta}h'_k + k^2h_k = \frac{6}{\eta^2}[R_\nu F_2 + (1 - R_\nu)\tilde{\Pi}^B] \quad (2.56)$$

where  $\tilde{\Pi}^B$  represents the time independent variable  $\Pi^B/\rho_\gamma$ . The large scales solution to this equation can be found expanding  $h_k$  in powers of  $(k\tau)$ . In order to keep the leading and the next-to-leading terms we need to take into account the neutrino octopole ( $F_3$ ), truncating the propagation of anisotropic stress through higher moments by posing  $F_4 = 0$ . Hence, the neutrino anisotropic stress evolves according to

$$\begin{aligned} F'_2 &= -\frac{4}{15}h'_k - \frac{k}{3}F_3 \\ F'_3 &= \frac{3}{7}kF_2 \end{aligned} \quad (2.57)$$

and the solution is then:

$$\begin{aligned}
h_k &= A \left[ 1 - \frac{5(k\tau)^2}{2(15 + 4R_\nu)} \right] + \frac{15(1 - R_\nu)\tilde{\Pi}^B(k\tau)^2}{28(15 + 4R_\nu)}, \\
F_2 &= -\frac{(1 - R_\nu)\tilde{\Pi}^B}{R_\nu} \left[ 1 - \frac{15(k\tau)^2}{14(15 + 4R_\nu)} \right] \\
&\quad + A \frac{4(k\tau)^2}{3(15 + 4R_\nu)}. \tag{2.58}
\end{aligned}$$

The presence of magnetic fields is responsible for the new leading term in  $F_2$  - otherwise absent. This is the so-called compensation between collisionless fluid and magnetic anisotropic stresses due to fact that magnetic fields gravitate only at perturbative level. Two new next-to-leading terms appear as well in  $F_2$  and  $h_k$  respectively.

To show the effect of compensation between neutrinos and PMF we have switched off the interaction of neutrinos with tensors keeping the magnetic contribution. From Eq. (2.56), the proper initial conditions for tensors are then

$$\begin{aligned}
h_k &= 6(1 - R_\nu)\tilde{\Pi}^B \log(k_*\eta), \\
h'_k &= 6(1 - R_\nu)\tilde{\Pi}^B \frac{1}{\eta}. \tag{2.59}
\end{aligned}$$

In the absence of compensating neutrinos, the amplitude of tensors grows logarithmically [65]. It is clear by comparing Eqs. (2.59) and (2.58) that gravitational waves behave completely different in presence of inhomogeneous primordial magnetic fields if free-streaming matter is taken, or is not, into account. See Fig. (2.5) for the impact of this difference onto tensor contribution to CMB anisotropies. It is clear that neutrinos should be taken into account in the computation of the tensor contribution to CMB anisotropies when inhomogeneous components as PMF are considered. One may argue that Eq. (2.59) might hold before the neutrino decoupling - a time prior to the initial time of Einstein-Boltzmann codes -, although other free-streaming matter might be present. It would be therefore interesting to study the neutrino decoupling to understand how eventually Eqs. (2.58) and (2.59) match.

### 2.5.1 Impact of PMF on CMB anisotropies

By our modified version of CAMB, we have computed the full contribution of a SB of PMF to CMB anisotropies in temperature and polarization.

We have considered some values of  $n_B$  and for all of them the CMB temperature pattern generated by the SB of PMF is dominated by the scalar contribution at low and intermediate multipoles; the vector contribution takes over the scalar one at high multipoles, whereas the tensor one is always sub-leading with respect to scalar and vector.

It is interesting to note that the  $B$  polarization signal due to the vector contribution is always larger than the tensor one. The  $B$  mode produced by vector perturbations has a power spectrum which can be steeper than the one produced by lensing with a peak around  $\ell \sim \text{few} \times 10^3$ ; therefore, for suitable values of the magnetic field amplitude the  $B$  mode produced by a SB of PMF can be larger than the lensing one for any  $n_B$ . For  $n_B > -3/2$  the  $B$  spectra from the vector contribution are almost indistinguishable for different  $n_B$ , because  $\Pi_B^{(V)}$  is white noise for  $k \ll k_D$ ; for  $-3 < n_B \leq -3/2$  we note a dependence of the  $B$  spectrum on  $n_B$ . Analogous dependence on  $n_B$  also holds for the vector contribution to  $TT$ .

$B$ -mode power spectra for magnetic spectral index  $n_B = 2$  and  $n_B = -2.5$  are shown in Fig. (2.5). Vector and tensor contributions are shown, compared to the one given by lensing of scalars. It is clearly visible how the compensation mechanism with neutrinos work: in the absence of it, magnetic contribution would be much larger (dot-dot-dashed line).

## 2.6 Energy Momentum Tensor

An energy momentum tensor can be associated to gravitons as the part of the Einstein's tensor quadratic in the perturbation  $h_{\mu\nu}$  [66, 67, 68],

$$\begin{aligned} \tau_{\mu\nu}^{GW} &= -\frac{1}{8\pi G} G_{\mu\nu}^{(2)} = -M_{\text{pl}}^2 \left[ R_{\mu\nu}^{(2)} - \frac{1}{2} (g_{\mu\nu} g^{\alpha\beta} R_{\alpha\beta})^{(2)} \right] \\ &= -M_{\text{pl}}^2 \left[ R_{\mu\nu}^{(2)} - \frac{1}{2} g_{\mu\nu}^{(0)} g^{(0)\alpha\beta} R_{\alpha\beta}^{(2)} \right] \end{aligned} \quad (2.60)$$

where by the superscript (2) we mean terms which are quadratic in the perturbation  $h_{ij}$ . The EMT of gravitons takes a perfect fluid form, being the energy density and the pressure associated respectively

$$\epsilon = \sum_s \frac{M_{\text{pl}}^2}{a^2} \int \frac{d^3k}{(2\pi)^3} \left[ \frac{1}{4} |h'_k|^2 + \frac{k^2}{4} |h_k|^2 + 2\mathcal{H} |h'_k h_k| \right], \quad (2.61)$$

$$p = \sum_s \frac{M_{\text{pl}}^2}{a^2} \int \frac{d^3k}{(2\pi)^3} \left[ -\frac{5}{12} |h'_k|^2 + \frac{7k^2}{12} |h_k|^2 \right] \quad (2.62)$$

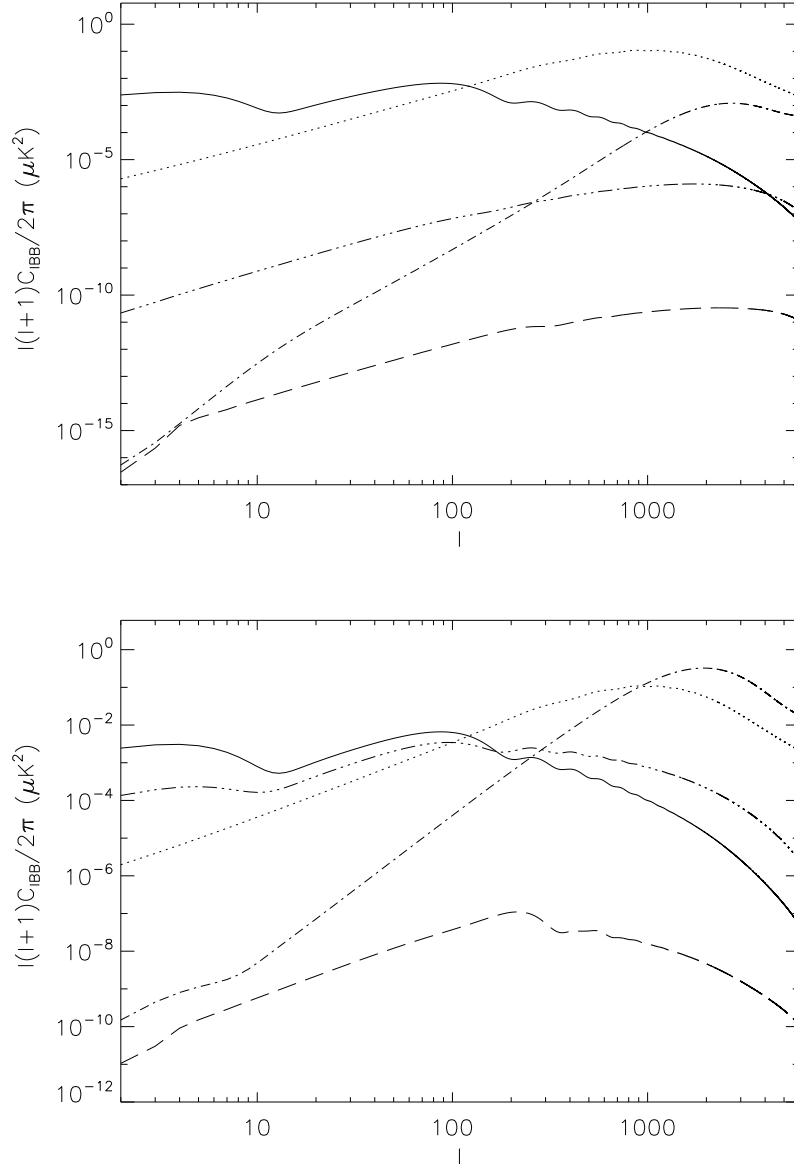


Figure 2.5: Upper panel: CMB  $B$  angular power spectrum. The solid line is the tensor homogeneous contribution for a tensor-scalar ratio  $r = 0.1$ ; the dotted, dot-dashed, dashed line is the lensing, vector and tensor contribution of a SB of PMF respectively for  $\sqrt{\langle B^2 \rangle} = 7.5$  nG,  $n_B = 2$  and  $k_D = 2\pi \text{ Mpc}^{-1}$ . The cosmological parameters of the flat  $\Lambda\text{CDM}$  model are  $\Omega_b h^2 = 0.022$ ,  $\Omega_c h^2 = 0.123$ ,  $z_{\text{re}} = 12$ ,  $n_s = 1$ ,  $H_0 = 100 h \text{ km s}^{-1} \text{ Mpc}^{-1} = 72 \text{ km s}^{-1} \text{ Mpc}^{-1}$ . Lower Panel: same as before but for  $n_B = -5/2$ . Dot-dot-dashed lines show the magnetic contribution in the absence of neutrinos: by comparing them with dashed lines, the effect of compensation is more than evident.

In de Sitter space-time the EMT of gravitons is conserved:

$$\epsilon' + 3\mathcal{H}(\epsilon + p) = 0 \quad (2.63)$$

As we will see later on, this is not true anylonger in radiation- and matter-dominated universe.

Assuming a scale factor evolving as  $a = a_* \eta^\beta$ , the homogeneous solution for tensor modes can be written in terms of Bessel functions of the first and second kind as follows

$$h_k = A_k \frac{J_{\beta-1/2}(k\eta)}{(k\eta)^{\beta-1/2}} + B_k \frac{N_{\beta-1/2}(k\eta)}{(k\eta)^{\beta-1/2}}. \quad (2.64)$$

Keeping only the growing mode of this solution and parametrizing the inflationary spectrum for tensors as,

$$A_k^2 = \tilde{A}^2 k^{-3+n_T}, \quad (2.65)$$

we calculate explicitly the quantities  $\epsilon$  and  $p$ , preserving a general dependence from  $\beta$  and  $n_T$ .

In the Appendix we perform explicitly the integration, here are the results:

$$\begin{aligned} \epsilon = & \frac{M_{\text{pl}}^2 \tilde{A}^2 \eta^{-2\beta-2-n_T}}{2^{2\beta-n_T} \pi^2 a_*^2} \left[ \frac{\Gamma(2\beta - n_T - 2) \Gamma(2 + n_T/2)}{\Gamma^2(\frac{2\beta-n_T-1}{2}) \Gamma(2\beta - n_T/2)} \right. \\ & + \frac{\Gamma(2\beta - n_T - 2) \Gamma(1 + n_T/2)}{\Gamma^2(\frac{2\beta-n_T-1}{2}) \Gamma(\frac{4\beta-n_T-2}{2})} \\ & \left. - 4\beta \frac{\Gamma(2\beta - n_T - 1) \Gamma(1 + n_T/2)}{\Gamma(\frac{2\beta-n_T-1}{2}) \Gamma(\frac{4\beta-n_T+1}{2}) \Gamma(2\beta - n_T/2)} \right] \quad (2.66) \end{aligned}$$

$$\begin{aligned} p = & \frac{M_{\text{pl}}^2 \tilde{A}^2 \eta^{-2\beta-2-n_T}}{2^{2\beta-n_T} \pi^2 a_*^2} \left[ - \frac{5\Gamma(2\beta - n_T - 2) \Gamma(2 + n_T/2)}{3\Gamma^2(\frac{2\beta-n_T-1}{2}) \Gamma(2\beta - n_T/2)} \right. \\ & \left. + \frac{7\Gamma(2\beta - n_T - 2) \Gamma(1 + n_T/2)}{3\Gamma^2(\frac{2\beta-n_T-1}{2}) \Gamma(\frac{4\beta-n_T-2}{2})} \right] \quad (2.67) \end{aligned}$$

with the condition

$$-2 < n_T < 2\beta - 2 \quad (2.68)$$

imposed by the integral convergence in the high frequency limit.

### 2.6.1 GW equation of state

Using the expressions above it is easy to show that for gravitational waves in a Friedmann-Robertson-Walker metric the conservation of EMT takes the form

$$\epsilon' + 3\mathcal{H}(\epsilon + p) = C \quad (2.69)$$

where

$$C = \frac{M_{\text{pl}}^2 \tilde{A}^2 \beta (1 + \beta) \eta^{-n_T - 3}}{2^{2\beta - n_T - 2} \pi^2} \times \left[ \frac{\Gamma(2\beta - n_T - 1) \Gamma(1 + n_T/2)}{\Gamma(\frac{2\beta - n_T - 1}{2}) \Gamma(2\beta - n_T/2) \Gamma(\frac{2\beta - n_T + 1}{2})} \right]. \quad (2.70)$$

It is thus worth to introduce an effective pressure

$$p_{\text{eff}} = p - \frac{\mathcal{H}C}{3} \quad (2.71)$$

such that the energy conservation looks as usual

$$\epsilon' + 3\mathcal{H}(\epsilon + p_{\text{eff}}) = 0. \quad (2.72)$$

Let us spend few words on equation of state of GW. Introducing the parameter of state

$$w_{\text{eff}} = \frac{p_{\text{eff}}}{\epsilon} \quad (2.73)$$

it is straight to obtain, from eq. (2.72), that

$$w_{\text{eff}} = \frac{2 - \beta + n_T}{3\beta}, \quad (2.74)$$

which in radiation- and matter-dominated period leads respectively to

$$w_{\text{eff,rad}} = \frac{1}{3} + \frac{n_T}{3}, \quad w_{\text{eff,mat}} = +\frac{n_T}{6} \quad (2.75)$$

This shows that GW's equation of state, in the limit of scale-invariant inflationary spectrum, tracks the background behavior.

In Fig. (??) the energy density spectrum at present time at large and small scales is shown. The mixed term in the energy density - usually neglected - carries a completely negligible contribution at high frequencies and then is of no relevance for direct detection of primordial gravitational waves. However its contribution is dominant at very large scale and then important

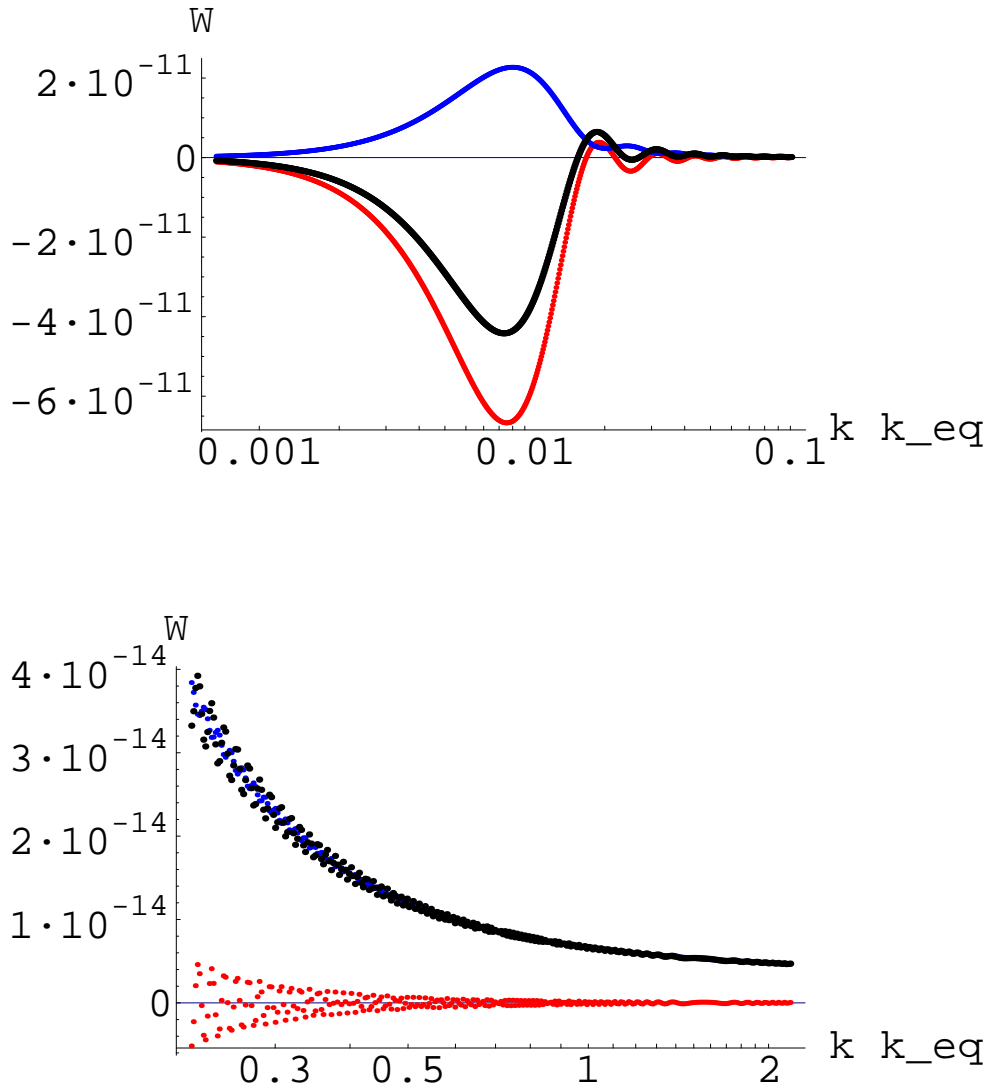


Figure 2.6: Energy density spectrum of primordial gravitational waves (black) at present time. Blue curves show what is usually assumed as energy density, i.e. the laplacian and kinetic term in the integral. Red curves show the contribution coming from the mixed term: it is very close to zero at for high frequency modes but not negligible at all at low frequencies.  $n_T = 0$  has been assumed and abscissa is normalized to the scale of matter-radiation equivalence,  $k/k_{eq}$ .

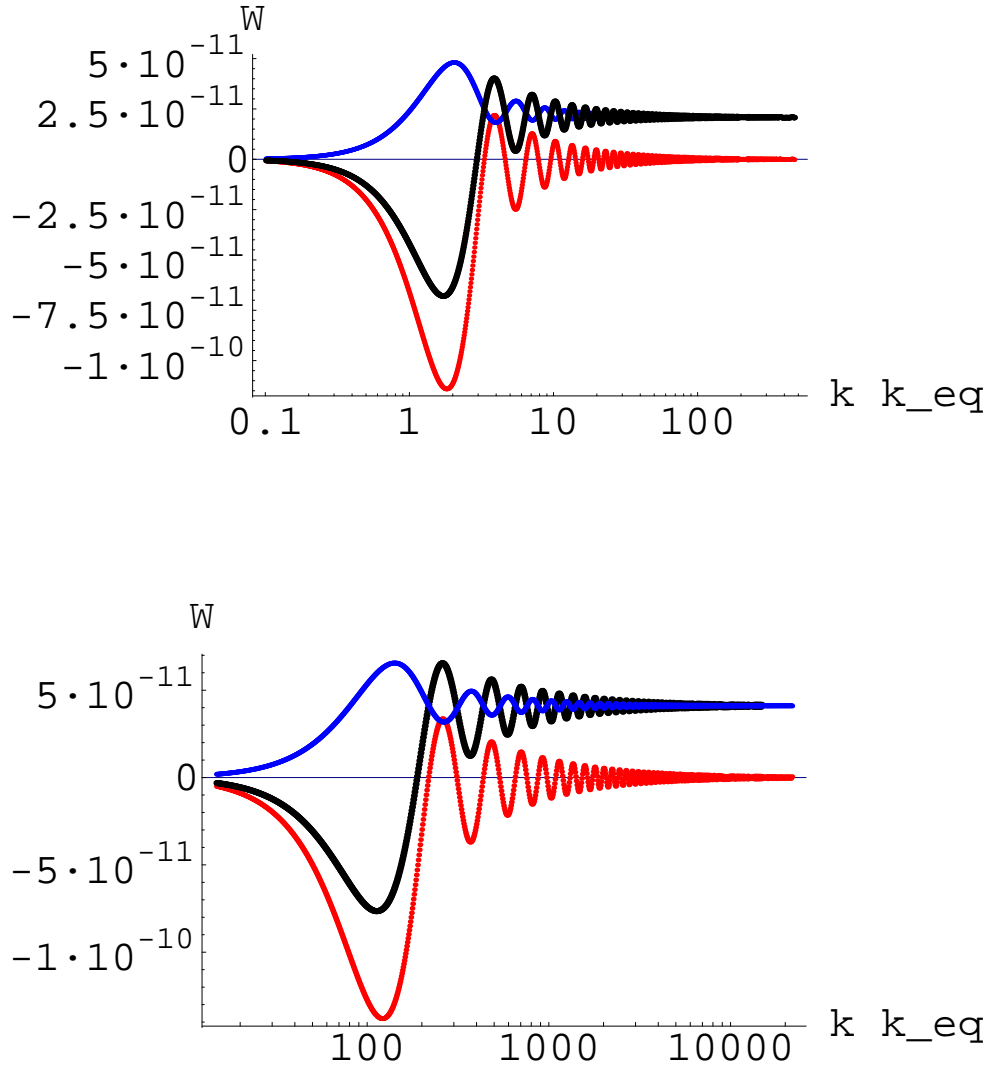


Figure 2.7: Energy density spectrum of primordial gravitational waves (black) at radiation-matter equivalence (top) and at  $z = 10^6$  (bottom). Blue curves show what is usually assumed as energy density, i.e. the laplacian and kinetic term in the integral. Red curves show the contribution coming from the mixed term: it is very close to zero at for high frequency modes but not negligible at all at low frequencies.  $n_T = 0$  has been assumed and abscissa is normalized to the scale of matter-radiation equivalence,  $k/k_{eq}$ .

for the integrated energy density.

Many efforts are put at present on the direct detection of gravitational. Several experiments (LIGO [69], LISA [70], TAMA300 [71], GEO600 [72], Big Bang Observer [73], DECIGO [74]) are dedicated to the direct detection of gravitational waves, either of primordial origin or from astrophysical emission processes. The typical frequencies at which these instruments work ( $\sim 1$  Hz) are order of magnitudes higher than those of interest for CMB. For this reason the two approaches - direct detection and through CMB anisotropies - are somehow complementary, as they study different scales. In this thesis we focus on the second one.

# Chapter 3

## CMB foreground cleaning

In mapping the sky at different frequencies in the microwave band, cosmological signal and emissions due to astrophysical processes are unavoidably blended. Our capability of extracting cosmological information from observing the sky is thus directly linked to our knowledge of the astrophysical emissions and the instrumental noise properties at the frequencies of interest. For this reason, assuming some external good description of the non-CMB signals, the best choice would be looking at the sky in the frequency window where these are as small as possible. On the other hand, since a detailed understanding of the astrophysical emission processes across the sky and in the frequency domain is still lacking, a wider frequency coverage for CMB mission is then convenient, being the ‘dirtiest’ channels used as tracers for different frequency dependent non-CMB signals. This approach allows us to improve our astrophysical knowledge and at the same time to perform a better cleaning of CMB maps. The multifrequency observation of the microwave sky has been adopted by the COBE and *WMAP* missions and, with a further push towards the highest frequencies by *Planck*.

In this chapter, after an overview on astrophysical foregrounds, we present some tests performed through the Internal Linear Combination method on polarization maps and suggests an alternative more viable way for CMB *B*-modes cleaning [49].

### 3.1 Astrophysical foregrounds

Galactic and extragalactic emission processes are responsible for a strong contamination of CMB measurements. Therefore, particular care must be taken in indentifying and removing their contribution before extracting any

information of cosmological interest from sky maps. In the microwave band, synchrotron emission from relativistic cosmic-ray electrons moving through the magnetic field of our galaxy ( $\sim 3 \mu\text{G}$ ), free-free emission (bremsstrahlung) from electron-electron scattering in the ionized interstellar medium and thermal emission from dust grains are the three major sources of contamination from our own galaxy. Radio and infrared point sources, together with the Sunyaev-Zeldovich effect - distortions of CMB photons moving through galaxy clusters -, are the most predominant sources of astrophysical extragalactic emission. Moreover, a fraction of foreground emissions is expected to be polarized. Although subdominant with respect to the temperature emission, polarized foreground contaminations represent a challenge in particular for the extraction of cosmological  $B$ -modes, being the latter fainter at all the frequencies of *Planck*.

The frequency dependence of synchrotron emission is well described by a power law,  $T(\nu) \propto \nu^{\beta_s}$ , where  $T$  is the antenna temperature and the index  $\beta_s$  is related to the energy distribution of electrons, assumed to follow a power law  $N(E) \propto E^{-p}$  as well, through  $\beta_s = -(p + 3)/2$ . A fraction

$$f_s = \frac{p + 1}{p + 7/3} \quad (3.1)$$

of such emission is then expected to be linearly polarized [75]. Current observations lead to a spectral index of order  $\beta_s \sim -3$  [76]. However, in order to take into account deviations from a simple power law affecting the high energy electron distribution, it is better to consider a varying synchrotron spectral index over the sky. Such a deviation induces a steeper spectral index for regions at high galactic latitude [77]. For  $\beta_s \sim -3$ , the relations above would lead to a degree of polarization of  $f_s \sim 0.75$ . However, superposition of different regions along the line of sight and Faraday rotation (almost irrelevant for the *Planck* frequencies) may play a role in reducing the effective polarization degree. Along the galactic plane, in particular, a strong depolarization is seen. Although not utterly from a physical point of view, temperature and polarization synchrotron spectral indices are usually modelled by the same parameters.

Free-free emission arises from interaction between electrons of the warm interstellar medium, at temperature of order  $\sim 10^4 K$  and is traced rather well outside the galactic plane by  $\text{H}\alpha$  emission [78]. The physics of such process is quite well known and its spectral behaviour quite close to a power-law with a (rather weakly frequency-dependent) spectral index of  $\sim -2.1$ . Given the different spectral index, synchrotron emission dominates over free-free emission at low frequency, getting the two comparable around 60 GHz. Since the scattering directions are random, free-free emission is unpolarized. A tiny

amount of polarization may arise, though, caused by Thomson scattering between photons and electrons at the edges of HII regions [79].

At frequency higher than, say  $\sim 80$  GHz, the dominant galactic foreground is the thermal emission from interstellar dust grains [80]. The simplest model of thermal dust emission is parametrized by one temperature and one spectral index as follows,  $I(\nu) \propto \nu^{\beta_d} B_\nu(T)$ , where  $B_\nu(T)$  is the Planck distribution. A refinement of the model, consists of assuming two populations of thermal dust, i.e. two temperatures and two spectral indices. *WMAP* observations are consistent with a choice of the four parameters of  $T_1 = 9.5K$ ,  $T_2 = 16K$ ,  $\beta_{d1} = 1.7$  and  $\beta_{d2} = 2.7$  [76]. A small amount of dust emission is expected to be polarized. This is due to the nonspherical shape of the dust grains, which align their long axes perpendicularly to the magnetic field and absorb starlight preferably in the same direction. Absorbed radiation is then re-emitted with a thermal spectrum. We observe therefore a polarization of starlight in the same direction of the magnetic field and a foreground of polarized thermal emission perpendicular to it. Unfortunately, our knowledge of thermal dust emission is still poor. A big step in this direction, will come with the *Planck* satellite, which will observe the polarized sky also at high frequencies, where the dust contribution is sensibly higher than synchrotron.

As mentioned above, extragalactic point sources and SZ effect are a source of foreground contamination as well, mostly for temperature and at very high multipoles. Only a very tiny amount of polarization may be introduced by point sources. SZ effect should be taken into account for the brightest sources (as Coma) but can be ignored as a diffuse foreground from our own galaxy.

### 3.1.1 CMB and foreground reconstruction methods

A wide number of methods which aim at cleaning CMB maps and reconstructing physical foreground emissions have been proposed in the literature. The *Planck* Working Group 2 is leading a great effort to study how different approaches perform on simulated *Planck* data [81].

While the primary goal of the mission is the cosmological analysis of CMB maps, a great interest lies in a deeper understanding of the astrophysical emission processes. For this reason, we can approach CMB cleaning in two different ways: treating CMB as one of the many physical signal we want to recover together with synchrotron, dust and free-free emissions, or focusing on isolating the CMB regardless of the physical mechanisms responsible for the ‘contaminating’ emission. It follows that different choices can be made in the level of assumptions on foregrounds. A classification scheme of foreground removal/reconstruction techniques is the following:

- *Blind.* Methods which do not make use of external information. An example is Internal Linear Combination, which does not require any knowledge of the foregrounds but performs a mere CMB separation, providing no physical information about them.
- *Unblind.* Strong assumptions are made in terms of physical model of foreground emissions. By fitting over the parameters of the model the different components are recovered. Obviously, if the model assumed is not correct the fit lead to completely wrong results.
- *Semi-blind.* External informations are used but without any modeling of the physical emission. Typically, external template are used as tracers for foregrounds and fit are performed over the combination of the template themselves.

In the following we focus on the first and the third method approach.

## 3.2 Internal linear combination

Internal linear combination [82] of multifrequency temperature maps has been performed by the WMAP team since the first year analysis [77]. In the following we review the algebra, extend it to polarization and discuss it in the context of *Planck* mission.

### 3.2.1 Algebra of the method

In this section we shall review the algebra of internal linear combination technique, starting with the traditional only-temperature case and moving then to include polarization as well.

We model the temperature data for each frequency channel  $i$  in the pixel  $p$  as

$$T_i(p) = S(p) + F_i(p) + N_i(p), \quad (3.2)$$

where  $S$  is the primordial signal and  $F$  and  $N$  are the foreground and instrumental noise emission respectively. What we are looking for is an estimate of  $S$  through a linear combination of the  $N_{ch}$  frequency maps

$$\hat{S}(p) = T^{\text{ILC}}(p) = \sum_{i=1}^{N_{ch}} w_i T_i(p), \quad (3.3)$$

being the coefficients independent of the position in the sky. Out of the infinite choices of the  $w_i$  coefficients, we want to pick up those which satisfy

two conditions: the variance of  $\hat{S}$  is minimized and the CMB - which is the only contribution to the data vector independent of the frequency - is properly counted. Introducing the quadratic form of the data

$$C_{ij} = \frac{1}{N_{\text{pix}}} \sum_{p=1}^{N_{\text{pix}}} (T_i(p) - \bar{T}_i) \times (T_j(p) - \bar{T}_j), \quad (3.4)$$

where  $\bar{T}_i$  is the mean temperature at frequency  $i$ , the first condition corresponds to minimize the quantity

$$\sum_{i,j=1}^{N_{\text{ch}}} w_i w_j C_{ij}, \quad (3.5)$$

while the second one imposes

$$\sum_{i=1}^{N_{\text{ch}}} w_i = 1. \quad (3.6)$$

With the help of some algebra, it is quite straightforward to show that building  $w_i$  as

$$w_i = \frac{\sum_{j=1}^{N_{\text{ch}}} C_{ij}^{-1}}{\sum_{i,j=1}^{N_{\text{ch}}} C_{ij}^{-1}}, \quad (3.7)$$

the two conditions above are satisfied. A proof of that which exploits the method of Lagrange multipliers can be found in the appendix of Ref. [83].

### 3.2.2 Polarization

An extension to polarization is presented in this section. The idea is the same as for the temperature case but the data set is now a set of three maps ( $T$ ,  $Q$  and  $U$  Stokes parameters) for each frequency and the linear combination we aim at must be some weighted sum of all such maps. Once again, the contribution from CMB to the data, this time also in the polarization sector, is expected to be frequency independent.

We stack all the data in a vector  $\mathbf{x}$ , say a vector of  $N_{\text{ch}} \times 3$  components for each pixel, and denote by  $\tilde{\mathbf{x}}$  the corresponding zero-mean vector (where the average is meant for each frequency channel). Along the same lines as before we build a quadratic form from the data

$$\mathbf{C} = \frac{1}{N_{\text{pix}}} \tilde{\mathbf{x}}^T \tilde{\mathbf{x}}, \quad (3.8)$$

and write the ILC solution corresponding to Eq. (3.3) as

$$\hat{\mathbf{c}} = \mathbf{w}^T \mathbf{x}, \quad (3.9)$$

where the corresponding of E. (3.7) is

$$\mathbf{w} = \mathbf{C}^{-1} \mathbf{e} (\mathbf{e}^T \mathbf{C}^{-1} \mathbf{e})^{-1} \quad (3.10)$$

In this notation the ILC coefficients  $w_i$  of the previous section are replaced by  $\mathbf{w}$ , a  $(N_{\text{ch}} \times 3)$  by 3 matrix, which assigns a weight to each of the  $N_{\text{ch}} \times 3$  maps for each of the 3 ILC cleaned maps ( $T$ ,  $Q$  and  $U$ ). The  $\mathbf{e}$  matrix has then the same dimension as  $\mathbf{w}$ , and is made of 0's and 1's, to ensure that CMB is counted just once.

### 3.2.3 Errors

Although the statistical goodness of ILC maps is somehow assured by the variance minimization, associated errors are not trivial to assess. We will consider then the case of instrumental noise simply described by a variance  $\sigma_i^2$  (uniform and isotropic noise) for each frequency channel. A first rough way of assessing the effective noise associated to ILC maps is then to propagate the noise variances through the ILC coefficients

$$\sigma_{\text{ILC}}^2 = \sum_{i,j=1}^{N_{\text{ch}}} w_i w_j \langle T_i T_j \rangle = \sum_{i=1}^{N_{\text{ch}}} w_i^2 \sigma_i^2 \quad (3.11)$$

One thing which is worth to be mentioned, though, is that the expression above should be used with some care. If some of the ILC weights are bigger than unity and the frequency noise levels are not particularly small, the sum can become large, leading to large effective errors for the ILC map. Moreover, to account for spatial variations of foreground over the sky, the ILC weights can be computed separately on patches. In that case the expression above could still hold region-by-region and need to be connected on the whole sky.

## 3.3 ILC for *Planck*

A Fortran 90 code which implements an Internal Linear Combination (ILC) algorithm has been used to study the impact of such a technique in cleaning polarization CMB maps for the *Planck* mission. Foreground maps have been produced with the Planck Sky Model<sup>1</sup> (PSM) at the *Planck* frequencies of 70, 100, 143 and 217 GHz (polarization maps are shown in Fig.

<sup>1</sup>The Planck Sky Model has been developed by the Planck Component Separation Working Group for use in simulations of the *Planck* mission [81]

(3.1)). CMB maps have also been simulated and added on top. All the maps have been generated at full *Planck* resolution ( $N_{\text{side}} = 2048$ ), smoothed with a  $7^\circ$  FWHM gaussian beam and reconstructed at low resolution ( $N_{\text{side}} = 16$ ). Table 1 shows the *rms* residuals of simulated CMB and foregrounds outside the mask adopted to cover the galactic plane (Fig. 3.2). The numbers immediately give the *B*-mode contribution to CMB compared to the foregrounds for polarization maps.

### 3.3.1 No-noise limit

In the absence of instrumental noise, an analytic solution for the ILC coefficients (Eq. (3.7)) can be written,

$$w_i = \frac{(1 + \sum_{jk} X_j F_{jk}^{-1}) \sum_j F_{ji}^{-1}}{\sum_{jk} F_{jk}^{-1}} - \sum_j X_j F_{ji}^{-1}, \quad (3.12)$$

where  $X_i$  and  $F_{ij}$  are a measure of the correlation between CMB and the *i*-th foreground and between foregrounds respectively,

$$X_i = \frac{1}{N_{\text{pix}}} \sum_{p=1}^{N_{\text{pix}}} S(p) F_i(p), \quad F_{ij} = \frac{1}{N_{\text{pix}}} \sum_{p=1}^{N_{\text{pix}}} F_i(p) F_j(p). \quad (3.13)$$

In Eq. (3.12) two contribution can be separate: one which depends entirely on the foregrounds regardless of the CMB signal and another one which quantifies the cross-correlations and is strongly dependent on the specific CMB realization.

ILC cleaning has been performed over the pixels outside the galactic mask shown in Fig.(3.2). The mask has been obtained by putting a threshold of  $10\mu\text{K}$  to the foreground polarization maps at 217 GHz. We are mainly interested in the impact of ILC on *B*-mode detection, we compare the residuals of ILC to the CMB contribution due to *B* modes.

For a more quantitative approach it is worth listing the ILC weights obtained and the *rms* of residuals ( $\langle (T^{\text{ILC}} - T^{\text{CMB}})^2 \rangle^{1/2}$  ( $\mu\text{K}$ )). In the upper panel of Table 2 we list the ILC coefficients computed from foregrounds alone, namely by replacing  $C_{ij}$  in Eq. (3.4) with  $F_{ij}$  of Eq. (3.13). The column in the right lists instead the residuals we get doing so. The lower panel lists the same quantities but where the ILC coefficients have been computed from the foregrounds+CMB maps.

It is quite evident from the only-foreground case that a set of weights that properly clean foreground contaminations does exist, being the residuals of

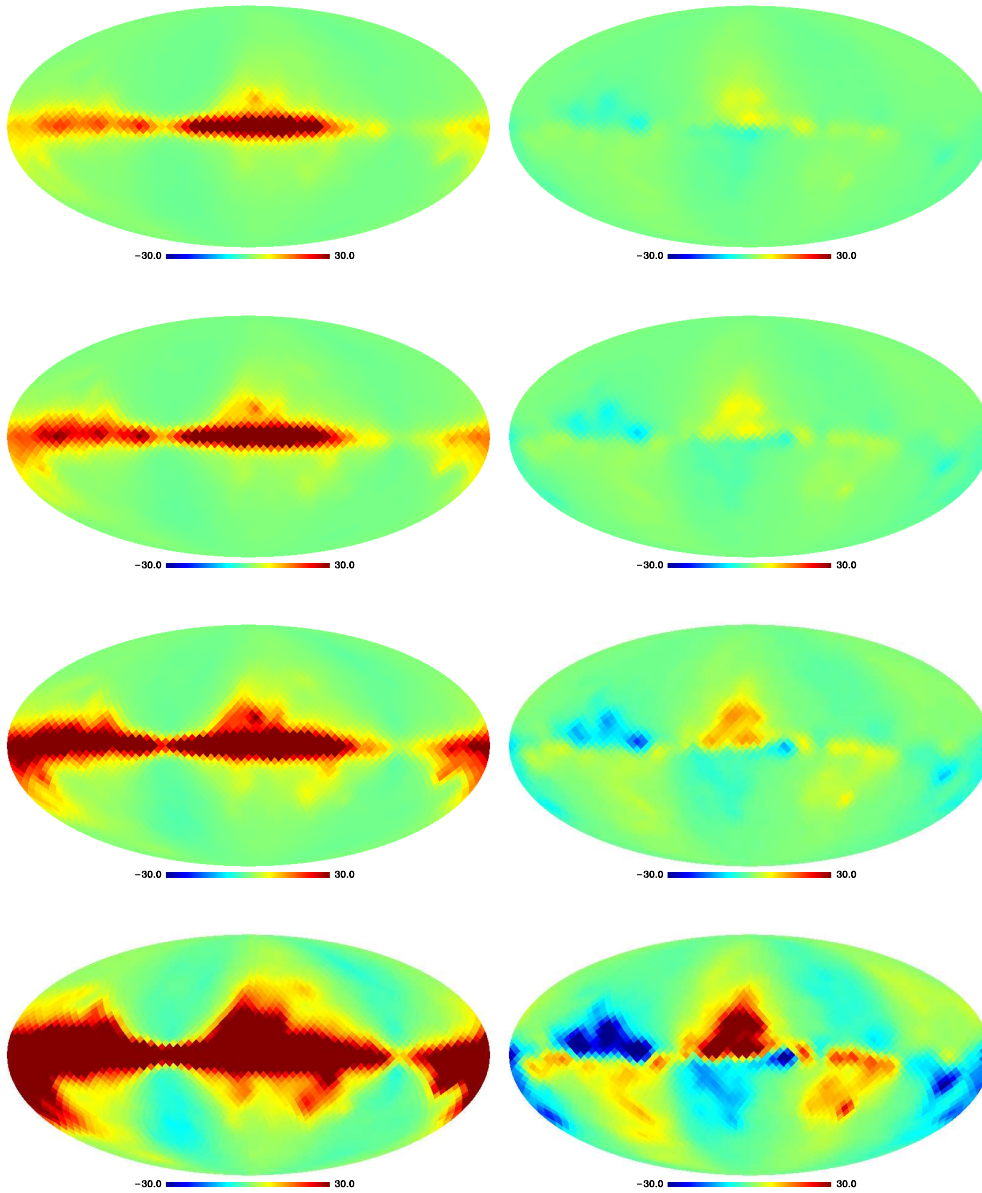


Figure 3.1: From top to bottom:  $Q$  and  $U$  foreground polarization maps at 70, 100, 143 and 217 GHz respectively

**Table 1: RMS residuals outside internal mask**

Map	$T$ ( $\mu\text{K}$ )	$Q$ ( $\mu\text{K}$ )	$U$ ( $\mu\text{K}$ )
CMB ( $r = 0$ )	50.4	0.257	0.232
CMB B-mode	2.26	0.062	0.064
PSM 70 GHz	19.0	0.661	0.608
PSM 100 GHz	22.7	0.720	0.692
PSM 143 GHz	40.8	1.29	1.27
PSM 217 GHz	119.2	3.82	3.76

Notes: CMB and foreground residuals outside the mask shown in Fig. (3.2).

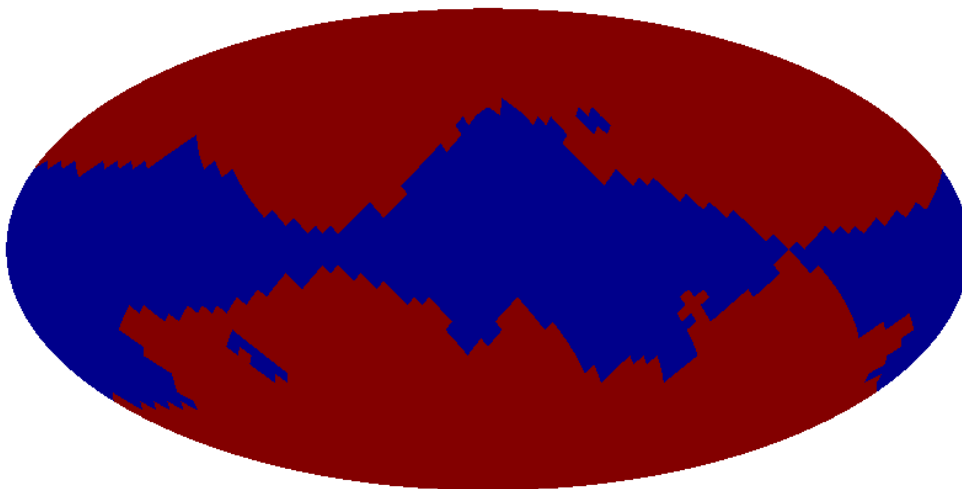


Figure 3.2: Galactic mask. It has been obtained by posing a threshold of  $10m\mu\text{K}$  on  $Q$  and  $U$  foreground maps at 217GHz. It cuts off about 36% of the sky

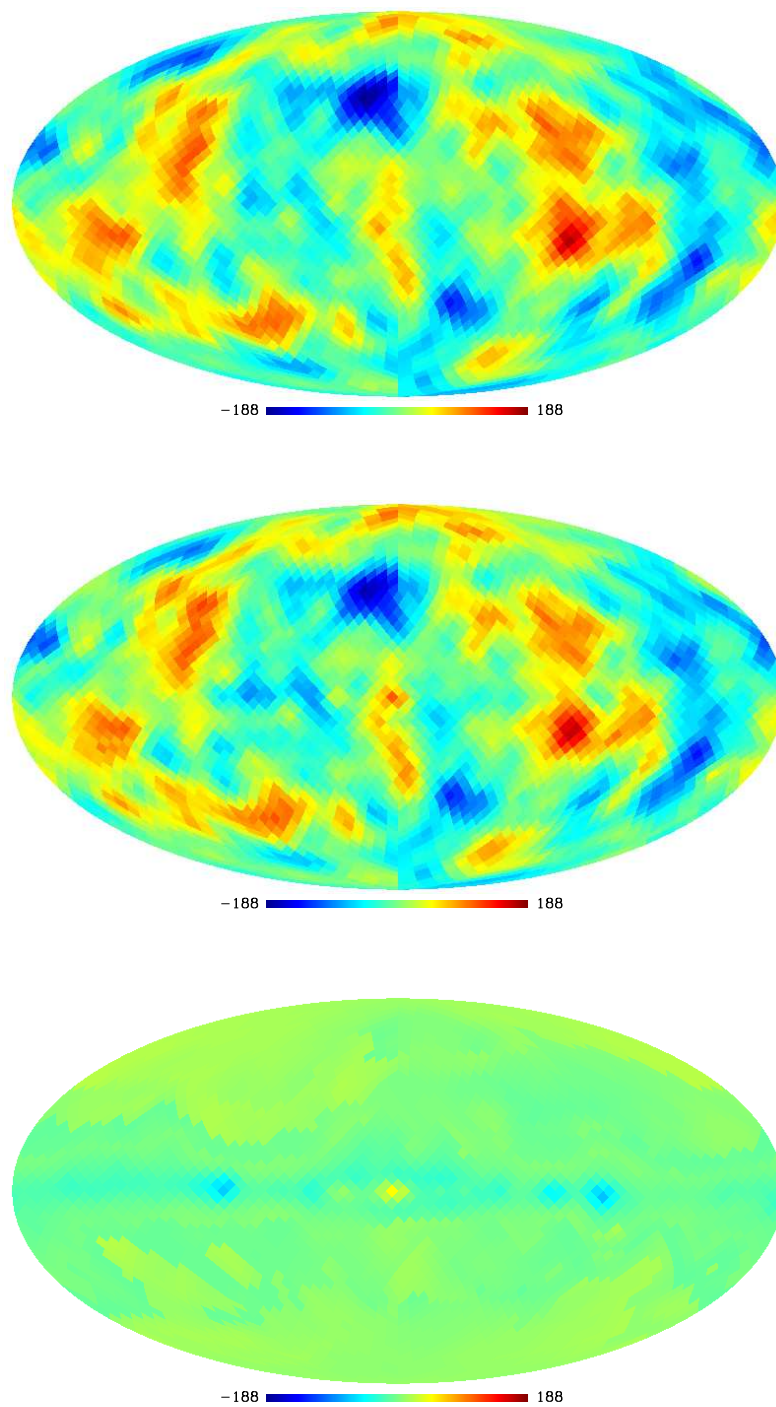


Figure 3.3: From top to bottom: simulated CMB temperature map, ILC map, map of residuals after ILC cleaning

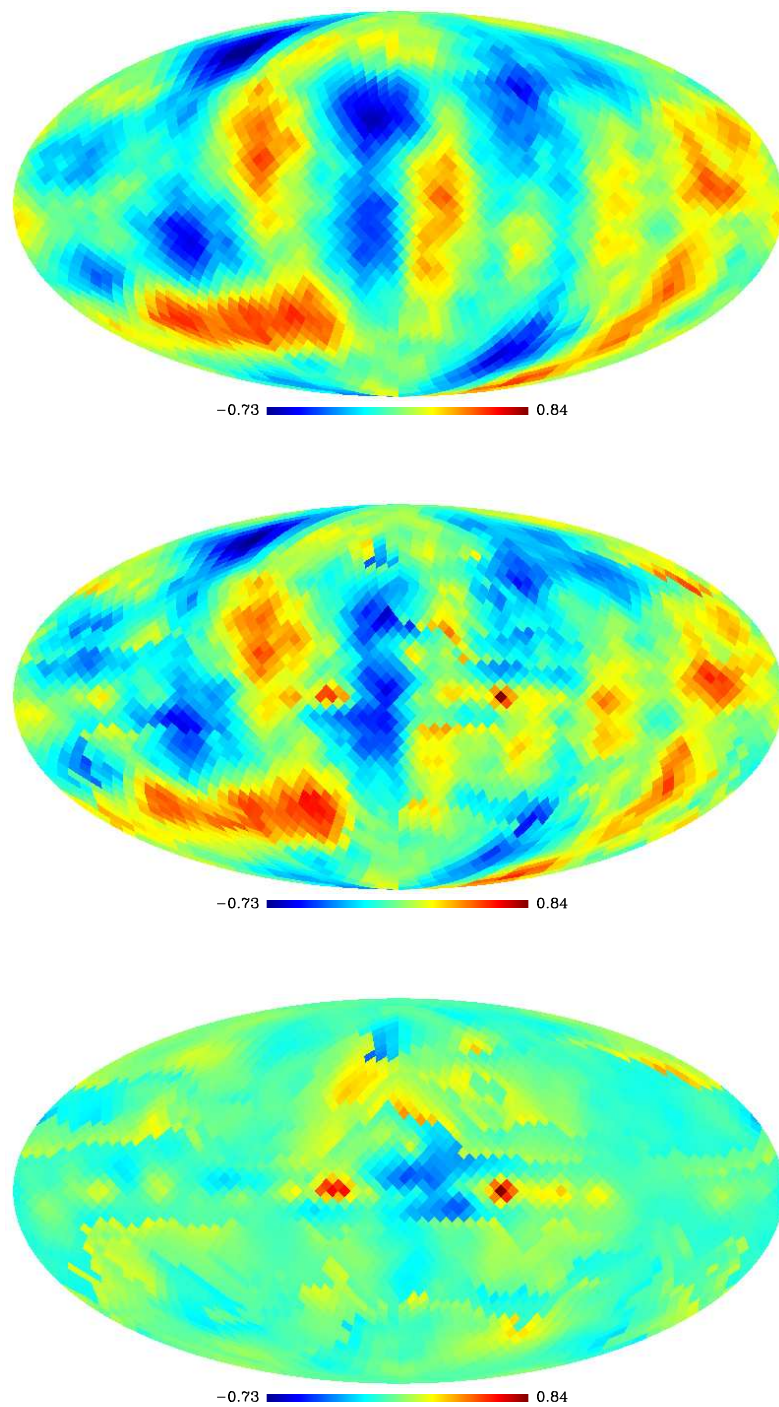


Figure 3.4: From top to bottom: simulated CMB  $Q$  map, ILC map, map of residuals after ILC cleaning

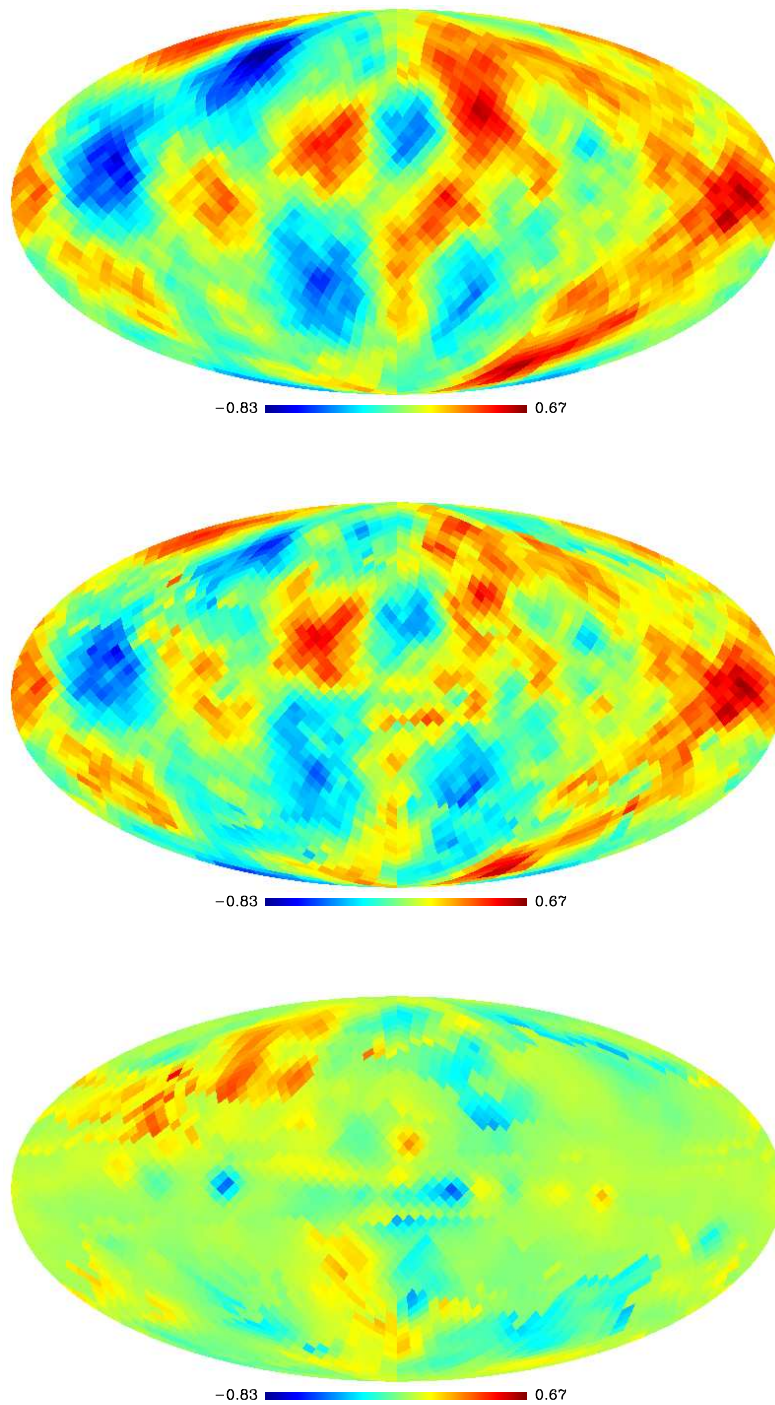


Figure 3.5: From top to bottom: simulated CMB  $U$  map, ILC map, map of residuals after ILC cleaning

Table 2: ILC weights

	70 GHz	100 GHz	143 GHz	217 GHz	
only Foregrounds	$w_1$	$w_2$	$w_3$	$w_4$	Res.
T	-0.1427	-1.0457	2.995	-0.8070	0.947
Q	-1.5525	5.2210	-2.936	0.2675	0.0054
U	-1.6387	5.5929	-3.285	0.3303	0.0047
Foregrounds+CMB	$w_1$	$w_2$	$w_3$	$w_4$	Res.
T	37.191	-129.68	113.52	-20.028	9.547
Q	-5.3553	19.526	-15.707	2.536	0.0578
U	-6.7704	26.042	-21.886	3.614	0.0619

Notes: ILC weights,  $w_i$ , computed from the foregrounds alone and for the combined foreground and CMB maps. The right column list the rms residuals of the ILC maps  $\langle (T^{\text{ILC}} - T^{\text{CMB}})^2 \rangle^{1/2}$ .

ILC maps one order of magnitude lower than the  $B$ -mode *rms*. This means that, in the no-noise limit, if we were given these weights we could perform a good cleaning through ILC. However, from the lower panel it is immediate to notice that this is not the case if we compute the weights from the coadded maps: the ILC residuals are comparable to those associated to the  $B$ -mode contribution (see Table 1), preventing us to recover the cosmological information. Most of the contribution to ILC residuals, thus, comes from the cross-correlation of foregrounds with the CMB.

### 3.3.2 Noisy case

In the limit of instrumental noise described by a noise variance  $\sigma_i^2$  for each frequency channel, the noise property of ILC cleaned maps are given by the linear combination of the noise variances  $\sigma_i^2$  through the ILC weights, as stated in Eq. (3.11). But since many of the weights listed in Table 2 are larger than unity, such a linear combination lead to a catastrophic noise level for the cleaned maps. For the foreground only case and the sensitivities of sc Planck they would lead to a level of noise of order  $\sim 0.6 \mu\text{K}$ . Including CMB in the ILC solution the situation becomes even more dramatic, getting the weights larger and larger. Minimizing the foreground contamination then lead to uncontrolled level of noise. On the other hand we might want to

minimize the noise, by selecting the ILC coefficients as

$$w_i = \frac{1}{\sigma_i^2} \left( \sum_j \frac{1}{\sigma_j^2} \right)^{-1}. \quad (3.14)$$

However, such a choice will not remove the foreground contribution.

To visualize the impact of noise on ILC cleaned  $B$ -modes we have performed a Monte Carlo analysis. Although not optimal for low multipoles<sup>2</sup>, a pseudo- $C_\ell$  estimator has been used to compare ILC cleaned maps power spectrum to the CMB input. Keeping the same foreground maps we produced  $10^5$  CMB skies and  $10^5$  noise realizations for each frequency considered (from the *Planck* nominal sensitivities [94]) and perform ILC cleaning on them. The averaged ILC cleaned noise levels are used to de-bias the spectrum, then deconvolved for the galactic mask. From Fig. (3.6) it is clear that the huge noise associated to ILC maps produce a large scatter on the estimates (but very small bias), which is still visible also after averaging over  $10^5$  realizations.

### 3.3.3 Impact of ILC on $r$

To study the impact of ILC cleaning on tensor-scalar ratio we generate ten CMB maps with  $r = 0$ , add the foreground contribution and clean the maps through the ILC prescription. We then compute the likelihood function for the ten ILC cleaned  $Q$  and  $U$  maps, allowing only  $r$  to vary. The likelihood function is

$$\mathcal{L} = \frac{1}{\sqrt{(2\pi)^n \det \mathbf{C}}} \exp \left[ -\frac{1}{2} \mathbf{x}^t \mathbf{C}^{-1} \mathbf{x} \right] \quad (3.15)$$

where  $\mathbf{x}$  is the dataset and  $\mathbf{C}$  is the covariance matrix. We assume a signal covariance matrix regularized by a small diagonal noise level of  $0.1\mu\text{K}$  which has been consistently added to the polarization maps. Residual errors from ILC are not taken into account in the covariance matrix.

Fig. (3.7) shows the likelihood distributions. Each of the ten realizations considered shows a different and rather broad likelihood distribution for  $r$ . As seen previously, the contribution to  $rms$  residuals associated only to foregrounds is subdominant (see Table 2), being the cross-correlations between CMB and foregrounds dominant. Such correlations are responsible for the large offset induced on the likelihood distribution of  $r$ , highly dependent on

---

<sup>2</sup>We will widely discuss CMB power spectrum estimation in Chapter 4. The reason why we use such a sub-optimal method here is that it offers a computationally faster tool to perform a Monte Carlo analysis

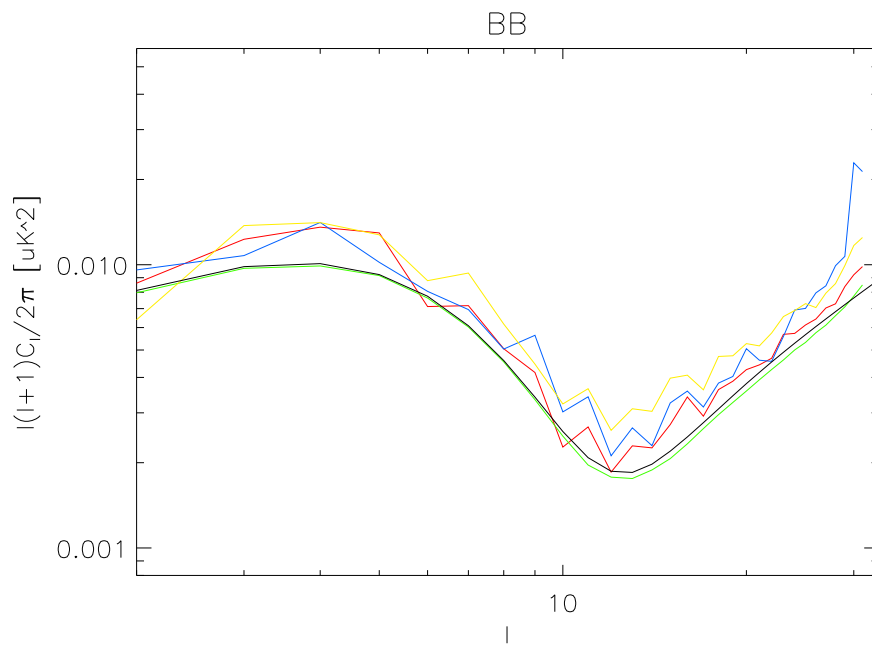


Figure 3.6: BB power spectrum averaged over  $10^4$  ILC cleaned noisy maps. The blue solid line has been obtained by performing a full sky ILC cleaning (no mask). The yellow curve shows the result of ILC coefficients computed using WMAP 5y polarization mask and the red one with WMAP 5y processing mask. The black solid line shows the CMB model used for simulations, recovered by the average over pure CMB realizations (green line).

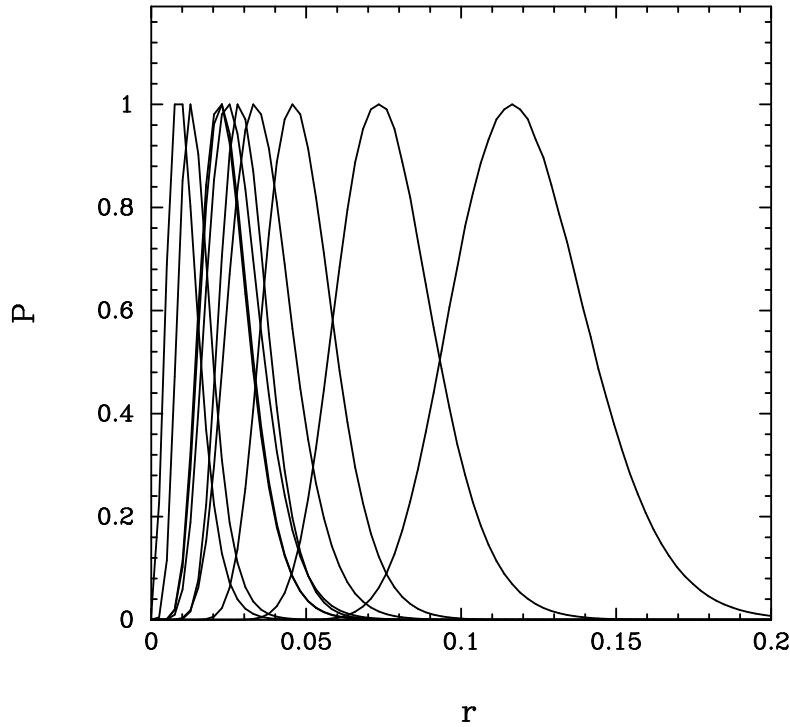


Figure 3.7: Probability distribution for  $r$  for ten ILC cleaned maps. The CMB model has  $r = 0$ .

the specific CMB realization, which can reach the value of  $r \sim 0.1$ . An offset of  $r \sim 0.1$  is consistent with what we found before: ILC cleaning on maps generated with  $r = 0$ , produces residuals comparable to the  $B$ -modes contribution when  $r = 0.1$ .

### 3.4 Template fitting

In this section we suggest an alternative more promising way for cleaning polarization maps than ILC does. The high level of cross-correlation between CMB and foregrounds is visible from the large spread in the probability distributions shown in Fig. (3.7). By making use of templates and fitting the data over them, we expect to reach better results. This is because any features common to CMB and foregrounds can be in principle disentangled with the help of some knowledge about spatial distribution of foregrounds.

We model the data as

$$\mathbf{x} = \mathbf{s} + \mathbf{F}\boldsymbol{\beta} \quad (3.16)$$

where  $\mathbf{s}$  is the signal,  $\mathbf{F}$  is the matrix of template maps and  $\beta$  is a set of parameters. The idea is to use two sets of  $Q$  and  $U$  simulated foreground maps as internal templates.

We combine CMB (with  $r = 0$ ) and foreground  $Q$  and  $U$  maps (same simulations used for ILC) by weighting them through the inverse noise variances. Therefore, the data vector we get contains the CMB and a combination of foregrounds. Once the parameters  $\beta$  have been found by minimizing

$$\chi^2 = (\mathbf{x} - \mathbf{F}\beta)\mathbf{C}^{-1}(\mathbf{x} - \mathbf{F}\beta), \quad (3.17)$$

where  $\mathbf{C}$  is the covariance matrix, we compute the maps  $\hat{\mathbf{s}} = \mathbf{x} - \mathbf{F}\beta$ . This estimate of the signal  $\mathbf{s}$  can be fed into Eq. (3.15) to compute the posterior of  $r$ . As for the case of ILC cleaning in the absence of instrumental noise, we plot (see Fig. (3.8)) the distribution for the tensor-scalar ratio we get from the  $Q$  and  $U$  cleaned maps. Two probability distributions are shown: one obtained performing the template fitting through the 30GHz and 217 GHz channels and the other one using the 30GHz and 353GHz channels. In the first case the distribution is very narrow around  $r = 0$ . Using the 353GHz channel as high frequency template, the posterior for  $r$  is slightly offset ( $\sim 3 \times 10^{-3}$ ), due to the fact that the high frequency template is not contained in the data vector.

In this section we have shown in the limit of no-noise that, if the PSM is a good description of the polarized foreground emissions, the use of internal templates for *Planck* performs by far better than ILC does at low resolution for polarization maps.

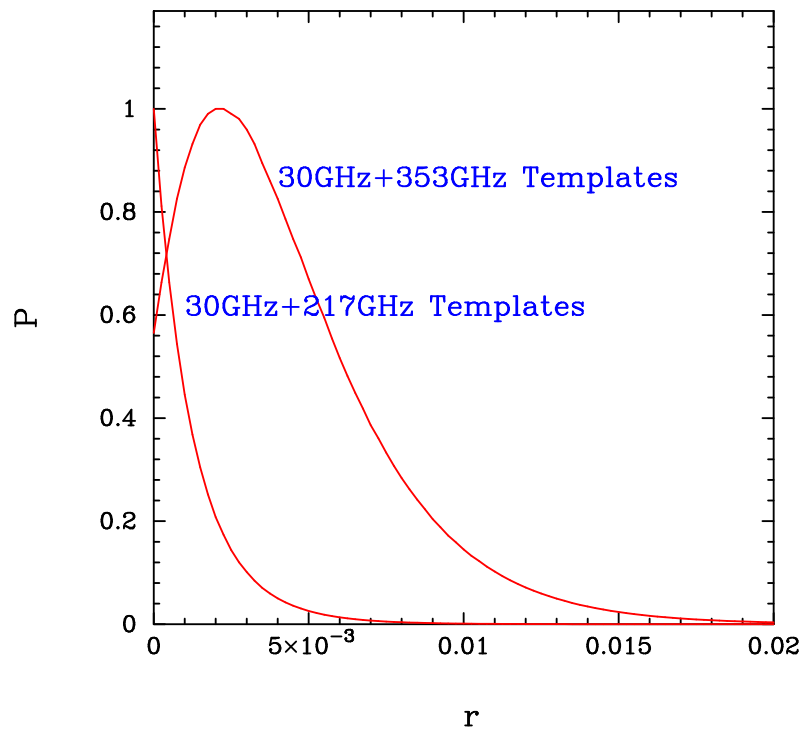


Figure 3.8: Top: Probability distribution of  $r$  by using two pairs of internal templates. We assume  $r = 0$  in the simulations.

# Chapter 4

## CMB power spectrum estimation

If CMB anisotropies are gaussian distributed, angular power spectra carry all the statistical information contained in CMB temperature and polarization maps. In the inflationary paradigm cosmological perturbations are expected to be very close to gaussian, and then mostly described in terms of their variance. Also from an observational point of view non-gaussianities are constrained to be rather small [56]; therefore power spectra represent a very useful compression of the cosmological information that we get mapping the sky in the microwave band.

In this chapter we will show the techniques typically used to estimate CMB power spectra and present a Fortran 90 code (*BolPol*) for power spectrum estimation (PSE) from temperature and polarization low resolution maps.

### 4.1 Pseudo- $C_l$ estimator

Angular power spectrum is the variance  $\ell$ -by- $\ell$  of the (ensemble averaged) harmonic coefficients  $a_{\ell m}$  of the sky map (let us focus for now on the temperature only case). The most straightforward and natural way of getting an estimate of it out of a map is just by directly transforming it by spherical harmonics:

$$a_{\ell m} = \int d\hat{n} T(\hat{n}) Y_{\ell m}(\hat{n}) \quad (4.1)$$

where the temperature field convolved with the spherical harmonic is integrated over the directions  $\hat{n}$ .

More operatively, since what we get from a CMB experiment is a pixelized map with finite size for each pixel, the direction in the sky  $\hat{n}$  is discretized

according to the pixelization scheme and the harmonic coefficients can be computed as a sum over the pixels:

$$\tilde{a}_{\ell m} = \sum_i T_i w_i \Omega_i Y_{\ell m}(\hat{n}_i), \quad (4.2)$$

where  $\Omega_i$  is the area of the pixel  $i$  and  $w_i$  is a weight for each pixel we may want to introduce. Because of the discretization of the map, we can not get any information on scales smaller than the pixel size and the coefficients above may be computed only up to some  $\ell = \ell_{\max}$ . By plugging them into

$$\tilde{C}_\ell = \frac{1}{2\ell + 1} \sum_{m=-\ell}^{\ell} |\tilde{a}_{\ell m}|^2. \quad (4.3)$$

we get *Pseudo- $C_\ell$*  estimates up to  $\ell_{\max}$ .

Weights different from unity may be required if we wish to mask the region of the sky along the galactic plane (just by putting the corresponding  $w_i = 0$ ), where the contamination from galactic astrophysical emissions is stronger. Pixels contaminated by sistematics or not covered by the scanning of the experiment can also be accounted for by a proper choice of the wights. A fundamental implication of cutting out the galactic plane or whatever else sky region is that spherical harmonics do not provide a complete and orthonormal set of functions any longer, being such only on the whole sphere. Such incompleteness of the sky coverage induces thus a mixing among harmonic coefficients and then among  $C_\ell$ 's. The approach usually adopted to face this issue is to correct the *Pseudo- $C_\ell$* 's for some coupling matrix, a geometrical object built up from the angular power specrum of the weights.

Unfortunately, it turns out that the estimates we obtain this way are biased because of the unavoidable presence of instrumental noise in the map on top of the cosmological signal. Therefore, to get unbiased estimates of CMB angular power spectrum we need to subtract the contribution coming from the instrumental noise, which can be computed through Eq. (4.2) starting from simulated noise time streams projected onto the sky according to the scanning strategy of the experiment. Reproducing the process a large number of times we get a Monte Carlo estimate of the average noise angular power spectrum.

Other effects, like the one induced by the intrinsic intrumental beam used to observe the sky - usually frequency dependent -, may be also taken into account in correcting *Pseudo- $C_\ell$*  estimates. Such an ingredient turns out to be essential in analysing very high resolution maps.

An important aspect one should take care of in estimating CMB angular power spectrum concerns the errors associated to the estimator. The way

they are commonly computed is through Monte Carlo on signal plus noise simulated maps. While for the latter one needs to know the noise properties of the instrument (the same used to debias the spectrum), the former requires the assumption of a CMB fiducial model.

The discussion above, although introduced for temperature spectrum, applies to polarization spectra as well. The starting point will be maps in the  $Q$  and  $U$  Stokes parameters and the harmonic basis used to expand the maps will be the two sets of *spin-2* spherical harmonics  $_{\pm 2}Y_{\ell m}$ .

### 4.1.1 Some technical details

We will give now a concise review of the maths one needs to know to construct a *Pseudo- $C_\ell$*  estimator and correct it for the effects introduced above.

Starting from two sets of harmonic coefficients  $X$  and  $Y$ , where  $X$  and  $Y$  are any of  $T$ ,  $E$ ,  $B$ , their *Pseudo-spectrum* is given by

$$\tilde{C}_\ell^{XY} = \frac{1}{2\ell + 1} \sum_{m=-\ell}^{\ell} \tilde{a}_{\ell m}^X \tilde{a}_{\ell m}^{Y*}. \quad (4.4)$$

and its ensemble average is related to the true power spectrum,  $C_\ell^{XY}$ , as

$$\langle \tilde{C}_\ell^{XY} \rangle = \sum_{\ell'} M_{\ell\ell'}^{XY, X'Y'} B_{\ell'}^{X'} B_{\ell'}^{Y'} C_{\ell'}^{X'Y'} + \langle \tilde{N}_\ell^{XY} \rangle, \quad (4.5)$$

where  $M_{\ell\ell'}^{XY, X'Y'}$  is the coupling matrix,  $B_\ell^X$  is the beam function and  $\tilde{N}_\ell^{XY}$  is the noise power spectrum. As mentioned before, the coupling matrix can be computed analytically once the geometry of the observed sky is known and a choice of a weighting scheme has been made, and can be expressed in terms of the Wigner 3- $j$  symbols. For the beam function, instead, the situation is different as they have to be measured experimentally. A first rough approximation might be the one of Gaussian symmetric beam,

$$B_\ell^X = \exp \left\{ -\frac{1}{2} \theta_X^2 \ell(\ell + 1) \right\}, \quad (4.6)$$

fully described by the rms beam width,  $\theta_X$ , but a real and complex mission like *Planck* implies a much deeper characterization of the observational beams. A big effort is being done by the *Planck* collaboration in this direction.

To conclude, one remark on noise power spectrum, which, as already pointed out, needs to be constructed from simulated noise maps. In case

of independent detectors it turns out that for cross-spectra ( $X \neq Y$ ) constructed on different maps, the noise is uncorrelated and there is no need of correcting *Pseudo- $C_\ell$*  estimates, being them not biased. Since only-noise simulations require a highly accurate knowledge of the instrumental noise properties, the possibility of not using them makes such an estimation of cross-spectra much more appetible than auto-spectra.

For more detailed discussions about the *Pseudo- $C_\ell$*  estimator we refer to the reader Refs. [84, 85, 86, 87].

## 4.2 Quadratic Maximum Likelihood estimator

The Quadratic Maximum Likelihood estimator for CMB temperature power spectrum was presented by Tegmark in 1997 [88]. Few years later, following the same lines as for the temperature case, an extension of the method to CMB polarization power spectra estimation appeared in the literature [89]. Such an estimator, built up in pixel space as a quadratic form of the data, i.e. the CMB maps, has been proved to be unbiased and optimal [88, 89]. While the meaning of the first property is clear, i.e. averaging over an infinit number of sky realizations the estimator converges onto the theoretical underlying power spectrum, the second one needs few more words. According to the Fisher-Cramer-Rao inequality [90], the inverse of the Fisher matrix of a set of parameters which we want to estimate represents the best covariance matrix in the parameters space; therefore if the covariance matrix associated to some estimator is just the Fisher matrix then that estimator has the smallest errors, and we may call it *optimal*. This is the case of QML estimator in the space of the  $C_\ell$ 's [88].

In the following we will review the algebra of the method, though without giving a detailed prove of it as it has already been done in the literature.

### 4.2.1 Algebra of QML

Let us introduce some notation and go through the algebra of QML estimator. We stack the temperature and polarization data in a column vector  $\mathbf{x}$  and write its covariance matrix  $\mathbf{C}$  as a sum of two contributions coming from the CMB itself and from instrumental noise respectively,

$$\langle \mathbf{x}\mathbf{x}^t \rangle \equiv \mathbf{C} = \mathbf{S} + \mathbf{N} = \sum_{\ell, X} C_\ell^X \mathbf{P}_\ell^X + \mathbf{N}, \quad (4.7)$$

being the former a linear combination of the parameters we want to estimate - the  $C_\ell^X$ 's, where  $X = T, E, B, TE, TB, EB$  - and the latter independent of them. Such a linear relation between covariance matrix and the  $C_\ell^X$ 's comes directly from choosing the spherical harmonics (and their generalization to spin-2 fields) as basis on the sphere for the temperature (and polarization) field, whose the  $\mathbf{P}_\ell^X$  functions are a proper rescaling. By construction, it turns out then that

$$\mathbf{P}_\ell^X = \frac{\partial \mathbf{C}}{\partial C_\ell^X}, \quad (4.8)$$

from which is evident that they are geometrical objects, independent of  $C_\ell^X$ . The QML estimator for  $C_\ell^X$  is defined as

$$\hat{C}_\ell^X = \sum_{\ell', X'} (F^{-1})_{\ell\ell'}^{XX'} \left[ \mathbf{x}^t \mathbf{E}_{\ell'}^{X'} \mathbf{x} - \text{tr}(\mathbf{N} \mathbf{E}_{\ell'}^{X'}) \right] \quad (4.9)$$

where

$$F_{\ell\ell'}^{XX'} = \frac{1}{2} \text{tr} \left[ \mathbf{C}^{-1} \frac{\partial \mathbf{C}}{\partial C_\ell^X} \mathbf{C}^{-1} \frac{\partial \mathbf{C}}{\partial C_{\ell'}^{X'}} \right] \quad (4.10)$$

is the Fisher matrix and  $\mathbf{E}_\ell^X$  is defined as

$$\mathbf{E}_\ell^X = \frac{1}{2} \mathbf{C}^{-1} \frac{\partial \mathbf{C}}{\partial C_\ell^X} \mathbf{C}^{-1}. \quad (4.11)$$

The two properties mentioned before which make such an estimator optimal can be written as follows,

$$\langle \hat{C}_\ell^X \rangle = C_\ell^X \quad \langle \Delta \hat{C}_\ell^X \Delta \hat{C}_{\ell'}^{X'} \rangle = (F^{-1})_{\ell\ell'}^{XX'} \quad (4.12)$$

where the averages are meant to be over an ensemble of realizations. The demonstration of these formulae are given in Appendix C.

### 4.3 *BolPol* - a QML for *Planck*

*BolPol* is a fully parallel Fortran 90 code which implements the QML method described above. Since the method works in pixel space the computational costs increase as one considers small angular resolution, in the scaling described below. This is the reason why a parallelization of the code was required. The inversion of the covariance matrix scales as  $\mathcal{O}(N_{\text{pix}}^3)$ . The number of operations is roughly driven, once the inversion of the total covariance matrix is done, by the matrix-matrix multiplications needed to build the operators  $\mathbf{E}_\ell^X$  in Eq. (4.11) and by calculating the Fisher matrix  $F_{\ell\ell'}^{XX'}$

given in Eq. (4.10). To do that, the number of operations scales as  $\mathcal{O}(N_{\text{pix}}^{7/2})$ . The RAM required is of order  $\mathcal{O}(\Delta\ell N_{\text{pix}}^2)$  where  $\Delta\ell$  is the number of  $\mathbf{C}^{-1} \mathbf{P}_\ell^X$  (for every  $X$ ) that are built and kept in memory during the execution time. The code is optimized such that the pre-factor of the memory scaling is 39 instead of 56 (that is the number of blocks of size  $N_{\text{pix}}^2$  that are present in the 6 matrices  $\mathbf{C}^{-1} \mathbf{P}_\ell^X$ , labeled by  $X$ ).

Given these kind of scalings, it is clear that it is unrealistic to run the QML estimator on maps of resolution larger than  $N_{\text{side}} = 8$  (Healpix parameter [92]), on a single CPU. To reach higher resolution we use the ScaLapack package and the BLACS routines, which allow us to run *BolPol* on the WMAP data set with the resolution of  $N_{\text{side}} = 16$  on a supercomputer like BCX (at CINECA, Bologna, processor type: Opteron Dual Core 2.6 GHz, with 4 GB per processor) in  $\sim 40$  minutes using 64 processors. *BolPol* has been run on  $N_{\text{side}} = 32$  simulated *Planck* maps leading to non-binned reliable estimates of the six power spectra up to  $\ell = 64$ .

#### 4.4 *BoLike* - a pixel-based likelihood code for *Planck*

As seen in the previous chapter, the likelihood function for a cosmological model given the data  $\mathbf{x}$  is

$$\mathcal{L} = \frac{1}{\sqrt{(2\pi)^n \det(\mathbf{C})}} \exp \left[ -\frac{1}{2} \mathbf{x}^t \mathbf{C}^{-1} \mathbf{x} \right] \quad (4.13)$$

where  $n$  is the dimension of the vector  $\mathbf{x}$ . *BoLike* is a Fortran 90 implementation of the exact expression above for temperature and polarization. It is a natural derivation of the *BolPol* code and can be used to compute the posterior probability of a given cosmological model or the conditional posterior probability of  $C_\ell$ . *BoLike* uses the same routines and modules as *BolPol* to build the signal covariance matrix. The code can handle the full noise covariance matrix (which needs to be provided) and different masks in intensity and polarization.

The computational costs are much lower than *BolPol* in terms of memory requirements, since only the inversion of the covariance matrix and the computation of the determinant need to be performed. At resolution  $N_{\text{side}} = 16$ , about 9 seconds are needed for each cosmological model. The parameter  $N_{\text{side}}$  corresponds to a map of  $12 \times N_{\text{side}}$  pixels. A  $(T, Q, U)$  full-sky map at  $N_{\text{side}} = 16$  is therefore represented by a vector of 9216 elements and its covariance by a matrix of 84,934,656 elements.

## 4.5 *BolPol* on *Planck* simulated data

We present now some results obtained with *BolPol* on *Planck* simulated data. Part of this work has been carried out within the *Planck* CTP working group activity<sup>1</sup>.

Realistic noise realizations together with the full noise covariance matrix at low resolution ( $N_{\text{side}} = 32$ ) for the 70GHz channel of *Planck* has been simulated by the developers of the *MADAM* map-making method [91], and CMB signal has been added on top. Such simulations are then available for the exercises of testing and comparison of different methods and implementations for the *Planck* community. We have joined the activity and here report the results.

The plot in Fig. (4.2), (4.3) and (4.4) show in red the estimates of all the six angular power spectra obtained with *BolPol* together with the associated error bars. The instrumental noise is almost negligible for temperature and the angular power spectrum of the particular CMB realization in intensity is very well recovered. For cross-correlations and polarization spectra, instead the high noise level compared to the cosmological signal is evident from the scatter of the estimates around the *true* sky. However, the scatter induced by a *Pseudo- $C_\ell$*  estimator at low multipoles would be much bigger.

An illustration is provided by the blue estimates and errors in the figures, which show how *ROMAster* perform on the same simulated data-set. At very low multipoles, where no binning procedure is usually adopted by the *Pseudo- $C_\ell$*  method, the blue estimates appear to be noisier and with larger error bars. The first 10 multipoles of *EE* spectrum are a clear evidence of how much the QML estimator improves over a *Pseudo- $C_\ell$*  approach. Moving towards the higher multipoles considered here, the effect is of course mitigated by the binning of *ROMAster*, whereas *BolPol* does not bin in any  $\ell$ 's. All these analysis has been performed masking the pixel corresponding to the galactic plane, as shown in Fig. (4.1).

On the same data-set we have also performed a likelihood analysis with *BoLike*. The conditional likelihood distributions for some multipoles are shown Fig. (4.5).

## 4.6 *Super 70GHz* channel

So far, the *BolPol* code has never been applied to CMB maps which contain a tensor contribution. In this section we present a very preliminary

---

<sup>1</sup>Courtesy of CTP working group.

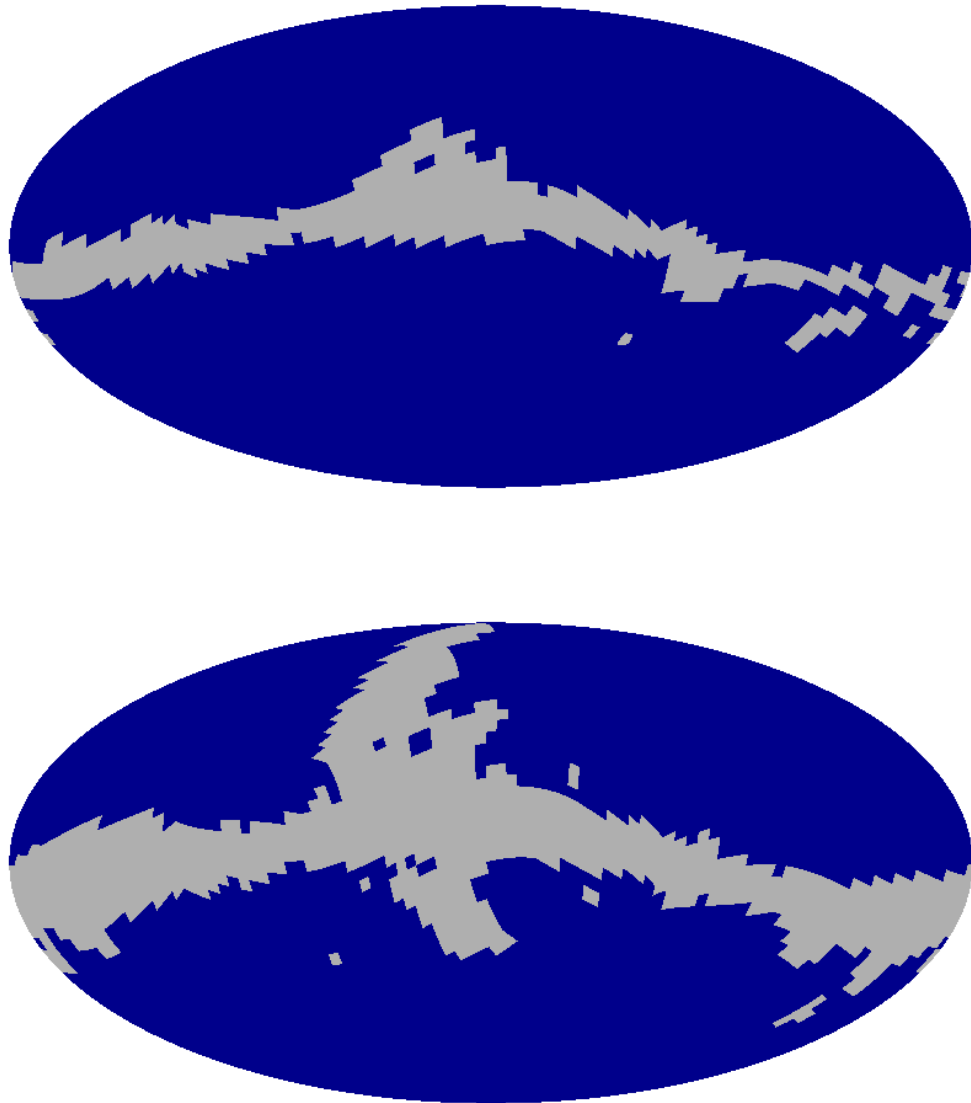


Figure 4.1: Temperature (top) and polarization (bottom) galactic masks adopted.

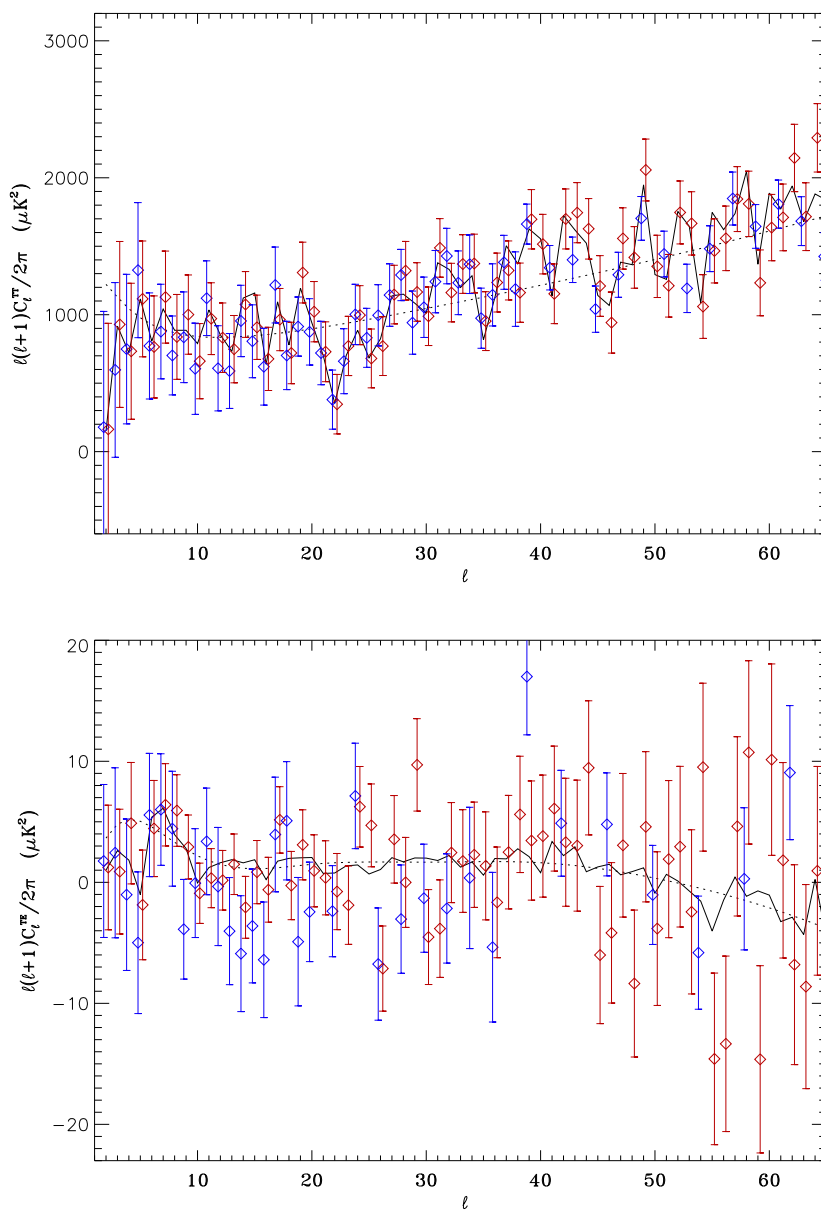


Figure 4.2: Red estimates and error bars have been obtained with *BolPol* on *Planck* CTP simulated data at resolution  $N_{\text{side}} = 32$ . Solid and dotted line show the *true* CMB sky used and the fiducial model beneath it respectively. In blue, the result from *ROMaster* on the same simulations. Top:  $TT$  spectrum. Bottom:  $TE$  spectrum.

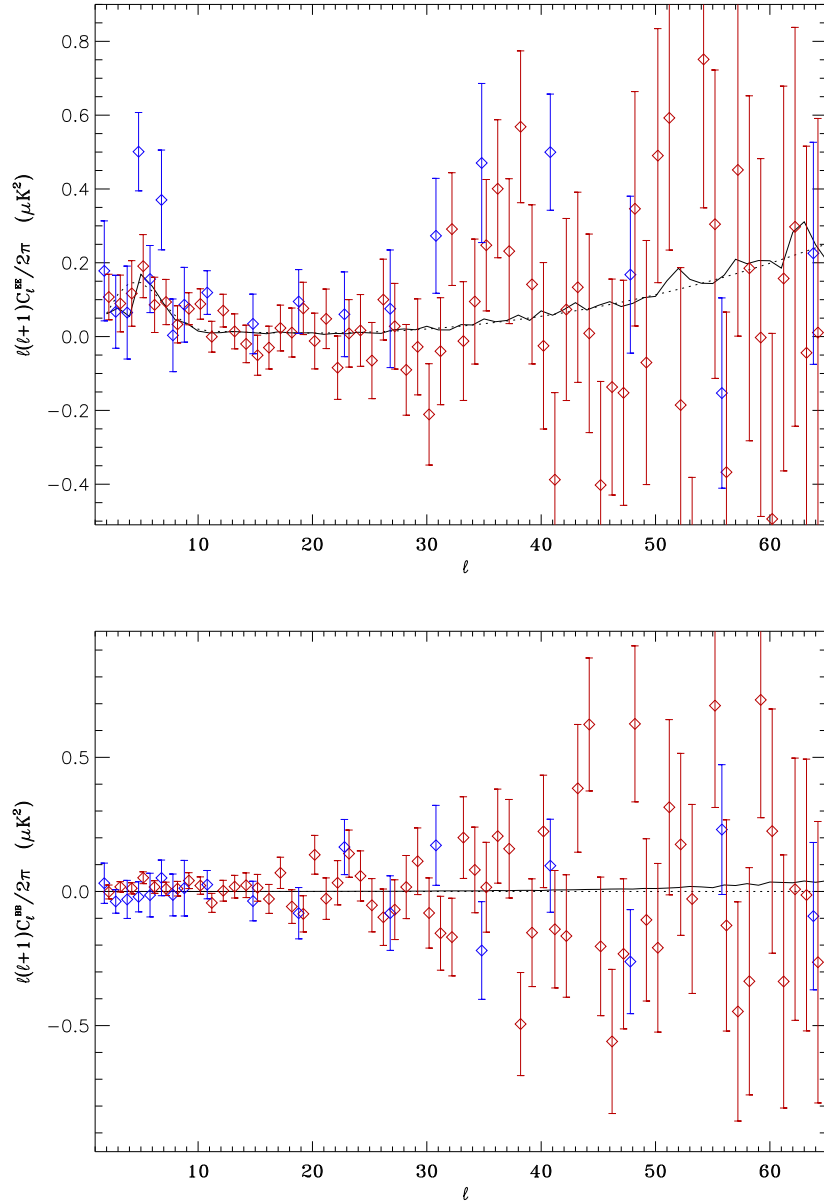


Figure 4.3: Red estimates and error bars have been obtained with *BolPol* on *Planck* CTP simulated data at resolution  $N_{\text{side}} = 32$ . Solid and dotted line show the *true* CMB sky used and the fiducial model beneath it respectively. In blue, the result from *ROMaster* on the same simulations. Top: *EE* spectrum. Bottom: *BB* spectrum.

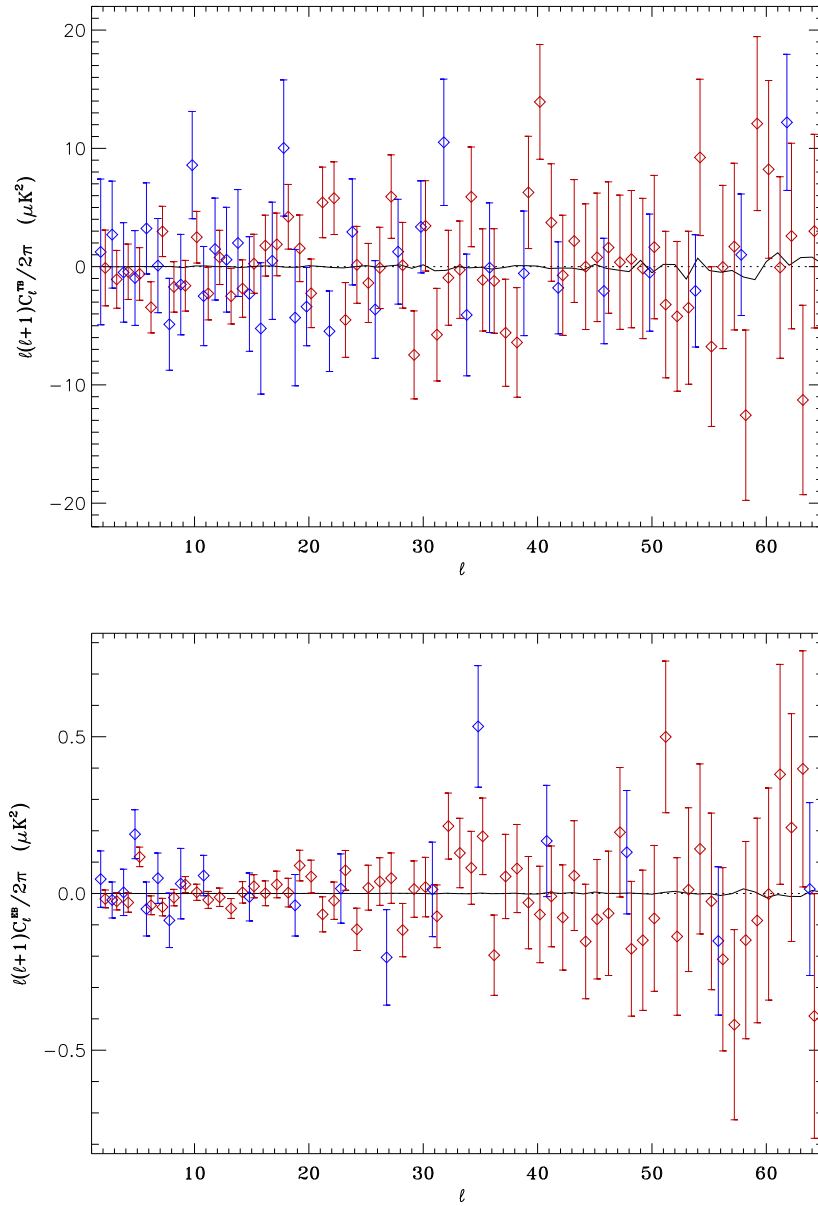


Figure 4.4: Red estimates and error bars have been obtained with *BolPol* on *Planck* CTP simulated data at resolution  $N_{\text{side}} = 32$ . Solid and dotted line show the *true* CMB sky used and the fiducial model beneath it respectively. In blue, the result from *ROMaster* on the same simulations. Top: *TB* spectrum. Bottom: *EB* spectrum.

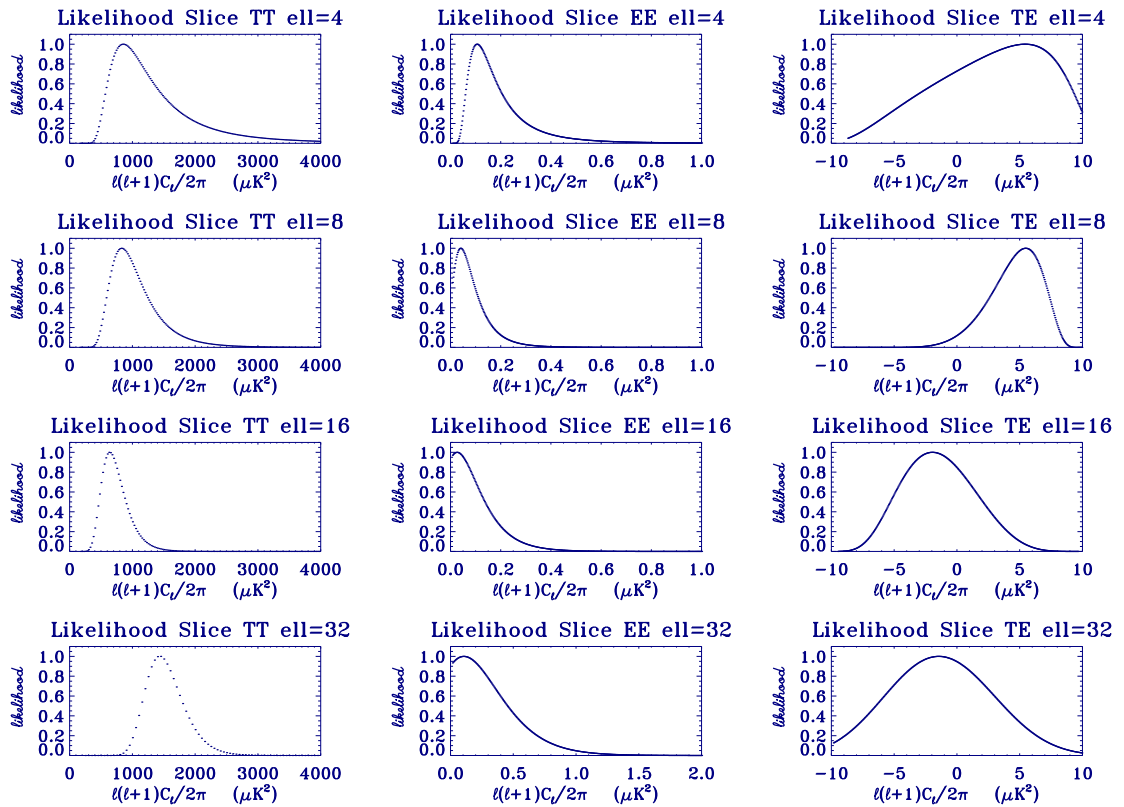


Figure 4.5: Conditional likelihoods for the *Planck* CTP data-set

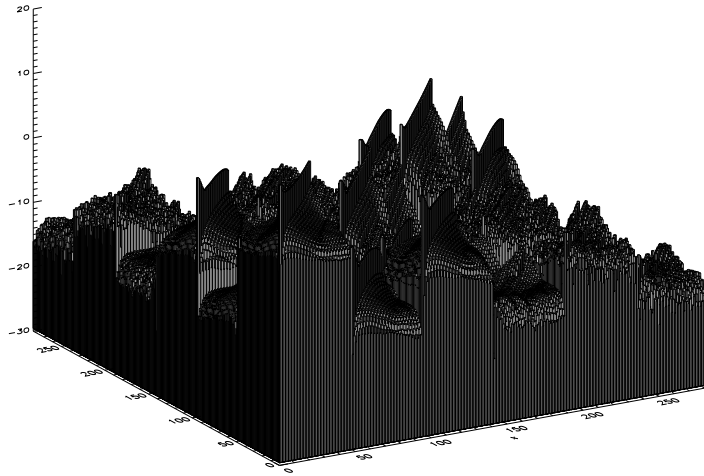


Figure 4.6: Inverse Fisher matrix

result on an attempt we made in that direction. We adopted a cosmological model described by the following six parameters  $\Omega_b h^2 = 0.0268$ ,  $\Omega_c h^2 = 0.1081$ ,  $A = 2.41 \times 10^{-9}$ ,  $n_s = 0.967$ ,  $\tau = 0.089$ ,  $H_0 = 72.4$  at pivot scale  $k_* = 0.02$  and add a tensor contribution  $r = 0.133$ . This cosmological model contains a primordial power spectrum for scalar and tensor perturbation generated by the simplest inflationary model with  $V(\phi) = (m^2 \phi^2)/2$ . From this model we generated a sky realization for temperature and polarization making use of the Healpix package at resolution  $N_{\text{side}} = 16$ . To describe the noise properties we rescaled the 70GHz *Planck* noise covariance matrix used within the CTP exercise by a factor 9.8944213; such a rescaling allows us to reach the nominal sensitivity of the 143GHz *Planck* polarized frequency channel [94], the most sensitive one. Of course, this is not exactly true for temperature but since the noise level would be in anycase far below the cosmological signal such an approximation does not lead to any significant error. From the rescaled noise covariance matrix we extracted a noise realization by Cholesky decomposing it. The angular power spectra estimated by *BolPol* are shown in Figs. (4.7, 4.8).

Few comments about Fig. (??) are in order. The temperature and the  $TE$  power spectra seem to have no bias, while  $EE$  presents a bias towards high multipoles.  $TB$  and  $EB$  scatter around their zero value. Note that the lower level of noise is clear with respect to Fig. (4.2-4.4). We do not provide

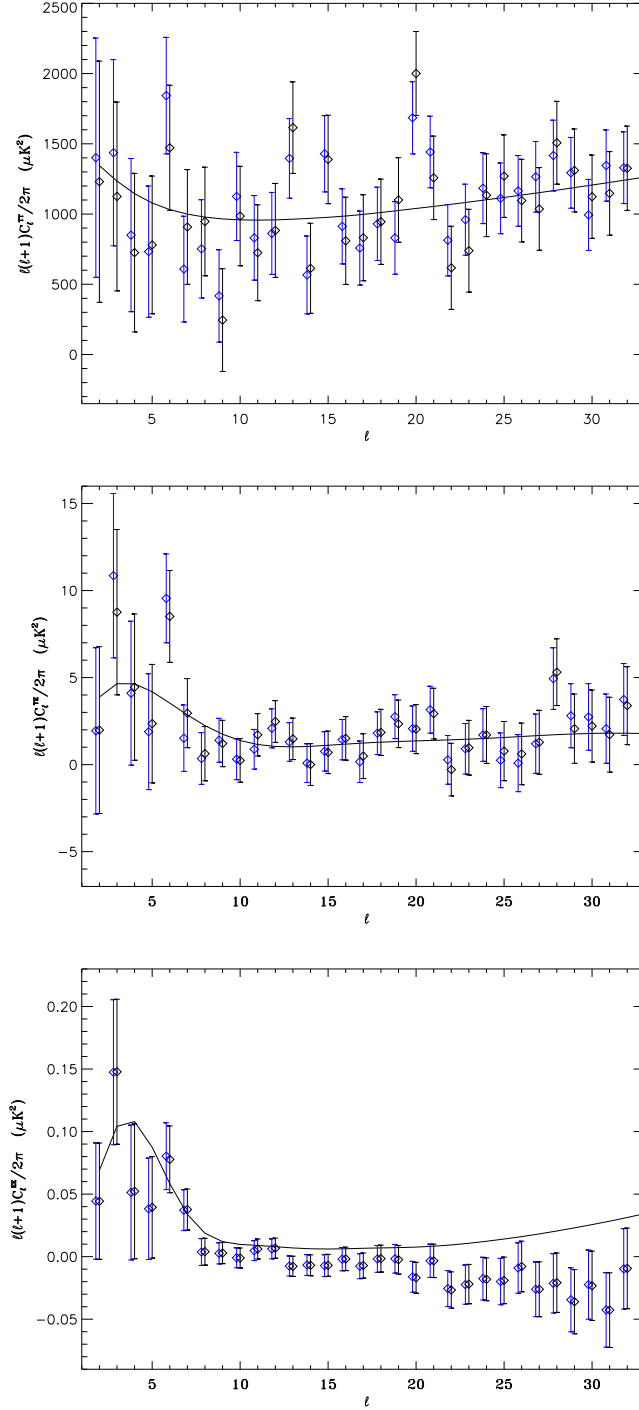


Figure 4.7: Estimates and errors from *BolPol* on a CMB realization from the model defined by:  $\Omega_b h^2 = 0.0268$ ,  $\Omega_c h^2 = 0.1081$ ,  $A = 2.41 \times 10^{-9}$ ,  $n_s = 0.967$ ,  $\tau = 0.089$ ,  $H_0 = 72.4$ ,  $r = 0.133$ ,  $k_* = 0.02$ . The sky has been masked either with the two temperature and polarization masks as above (blue) or by applying the polarization mask also to the temperature map (black). From top to bottom:  $TT$ ,  $TE$ ,  $EE$

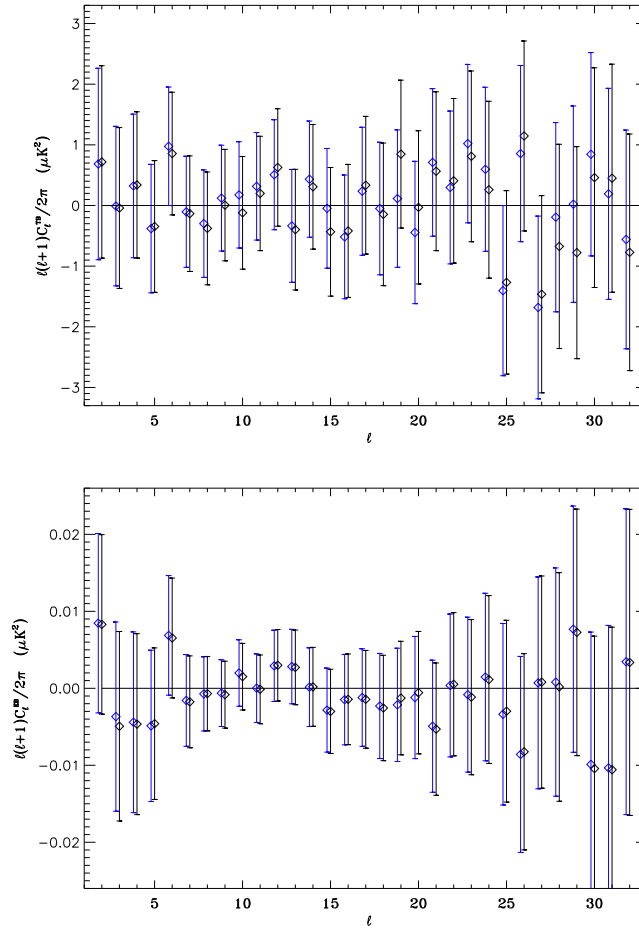


Figure 4.8: Estimates and errors from *BolPol* on a CMB realization from the model defined by:  $\Omega_b h^2 = 0.0268$ ,  $\Omega_c h^2 = 0.1081$ ,  $A = 2.4110^{-9}$ ,  $n_s = 0.967$ ,  $\tau = 0.089$ ,  $H_0 = 72.4$ ,  $r = 0.133$ ,  $k_x = 0.02$ . The sky has been masked either with the two temperature and polarization masks as above (blue) or by applying the polarization mask also to the temperature map (black). *TB* (top) and *EB* (bottom) spectra

the  $BB$  spectrum since it seem to present troubles and deserves more study.

## 4.7 Application to *WMAP* low-resolution data

In the following, we will describe the application of *BolPol* to the *WMAP* 5 year low resolution data-set. The products we used are public and available at the LAMBDA web site<sup>2</sup>. The temperature map is the ILC map at  $N_{side} = 16$  smoothed with a 9.8 degrees Gaussian beam. We have added a random noise realization with variance  $1\mu\text{K}^2$ , following the *WMAP* procedure. Consistently, the noise covariance matrix in the  $TT$  sector has been assumed diagonal with variance  $1\mu\text{K}^2$ . The temperature map has been masked with KQ85 mask used by the *WMAP* team and the monopole and the dipole have been subtracted from the observed sky by means of the Healpix routines[?]. The  $Q$  and  $U$  polarization maps are provided by the *WMAP* team at the same resolution  $N_{side} = 16$ . The inverse of the masked noise covariance matrix for the polarization part is available at the same resolution on the LAMBDA web site. We have followed the procedure explained at the LAMBDA web site to obtain the direct noise covariance for the observed pixels. The polarization mask is the one which the *WMAP* team made of for the analysis at low resolution, slightly larger than the temperature one. The noise covariance matrices for  $TQ$  and  $TU$  block are not provided and we set them to zero.

### 4.7.1 Results

We present the results obtained by our implementation of the QML estimator on the low resolution *WMAP*5 maps described above and those obtained by the *WMAP* team in Figs. (4.7)-(4.12) for  $TT$ ,  $EE$ ,  $TE$  and  $BB$  spectrum respectively. In the top panels we show the *BolPol* estimates with error bars (dark blue or red, see below) and the (*Pseudo- $C_\ell$* ) estimates obtained by the *WMAP* team with error bars (light blue). The *BolPol* estimates in dark blue are obtained by using as fiducial spectrum the theoretical *WMAP*5 best-fit [93], a  $\tau\Lambda\text{CDM}$  cosmological model with  $\Omega_b h^2 = 0.0227$ ,  $\Omega_c h^2 = 0.108$ ,  $H_0 = 72.4 \text{ km s}^{-1} \text{ Mpc}^{-1}$ ,  $\tau = 0.089$ ,  $n_s = 0.961$ ,  $A_s = 2.41 \times 10^{-9}$  (at  $k = 0.002 \text{ Mpc}^{-1}$ ). Error bars loose dependence on the fiducial model by iterating the QML: we use the first run of *BolPol*<sup>3</sup> to obtain

<sup>2</sup><http://lambda.gsfc.nasa.gov/>

<sup>3</sup>As fiducial spectra for the iterated *BolPol* run we use the first  $TT$  and  $TE$  *BolPol* estimates and leave the  $EE$  as given in the previous fiducial model when possible. The fiducial spectra of  $BB$ ,  $TB$ ,  $EB$  for the iterated *BolPol* run are set to zero.

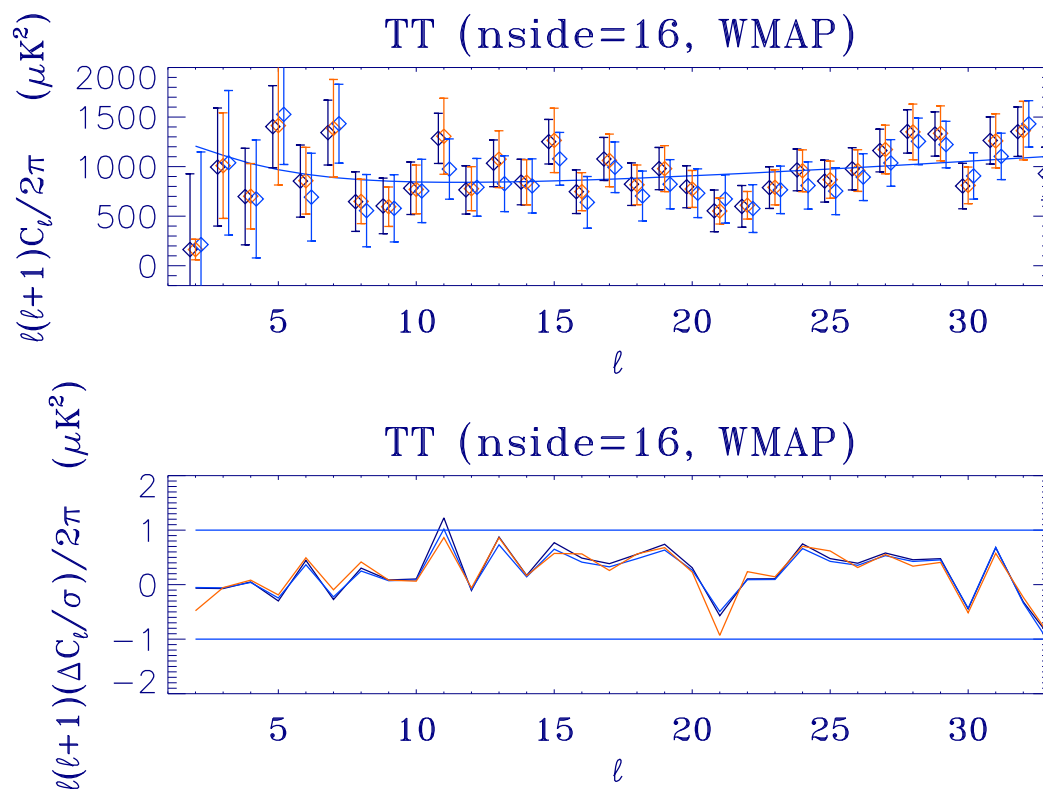


Figure 4.9: Estimates of TT angular power spectrum from WMAP 5 year data at low resolution. Upper panel: BolPol estimates (dark blue diamonds) with error bars (dark blue), iterated BolPol estimates (red diamonds) with error bars (red), WMAP estimates (light blue diamonds) with error bars (light blue). Lower panel: differences between the sets of estimates in unit of sigma (same conventions as upper panel).

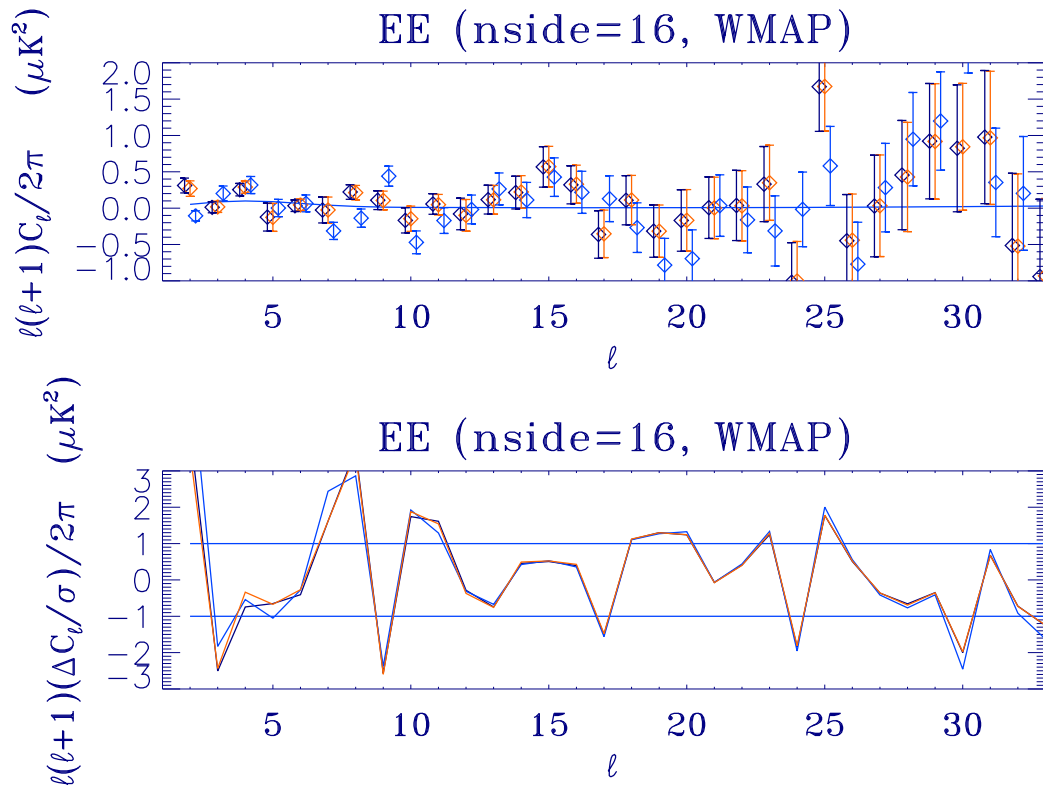


Figure 4.10: Estimates of TE angular power spectrum from WMAP 5 year data at low resolution. Upper panel: BolPol estimates (dark blue diamonds) with error bars (dark blue), iterated BolPol estimates (red diamonds) with error bars (red), WMAP estimates (light blue diamonds) with error bars (light blue). Lower panel: differences between the sets of estimates in unit of sigma (same conventions as upper panel).

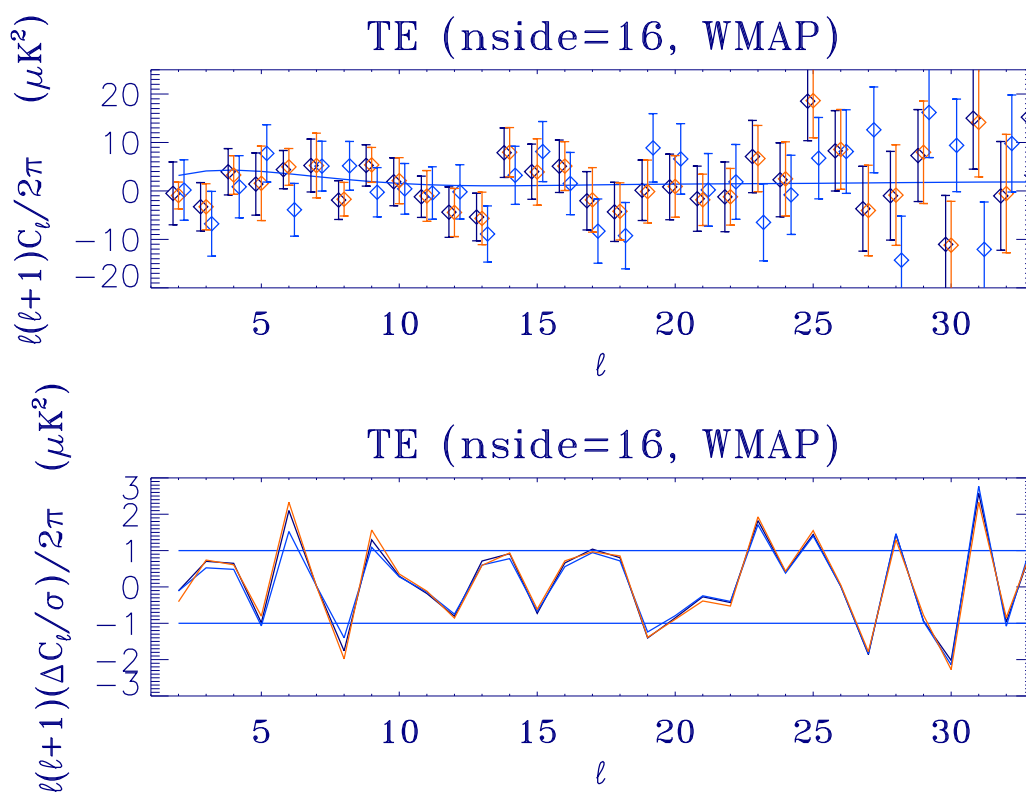


Figure 4.11: Estimates of EE angular power spectrum from WMAP 5 year data at low resolution. Upper panel: BolPol estimates (dark blue diamonds) with error bars (dark blue), iterated BolPol estimates (red diamonds) with error bars (red), WMAP estimates (light blue diamonds) with error bars (light blue). Lower panel: differences between the sets of estimates in unit of sigma (same conventions as upper panel).

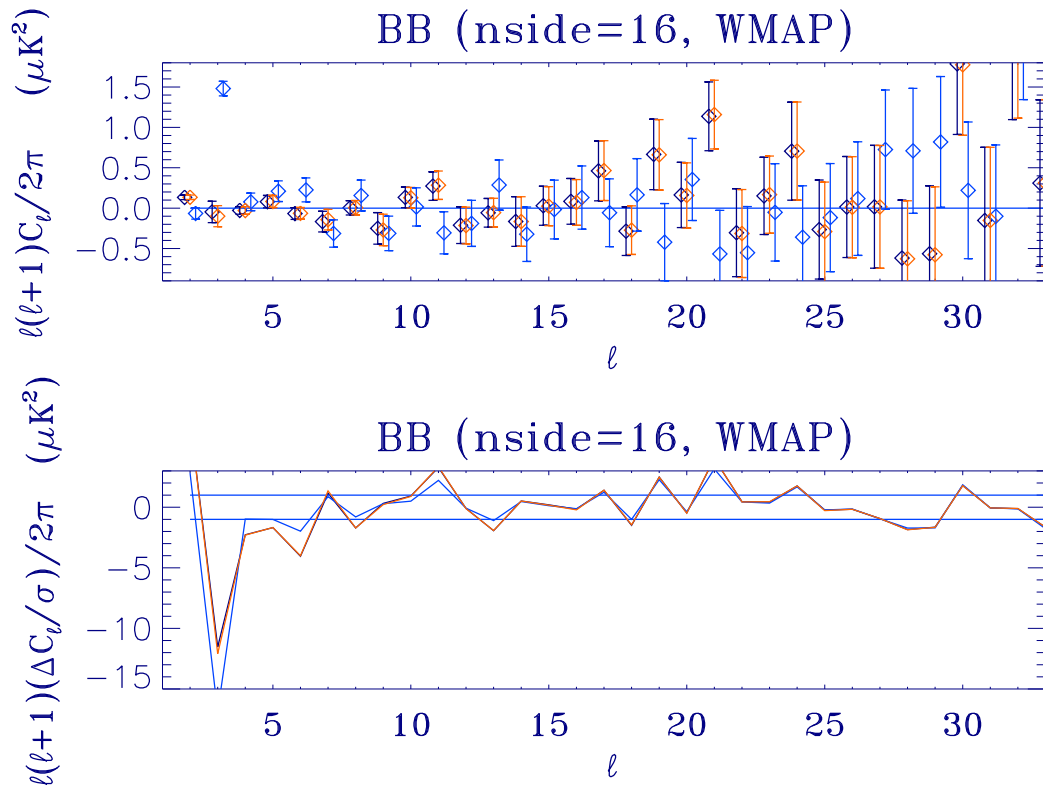


Figure 4.12: Estimates of BB angular power spectrum from WMAP 5 year data at low resolution. Upper panel: BolPol estimates (dark blue diamonds) with error bars (dark blue), iterated BolPol estimates (red diamonds) with error bars (red), WMAP estimates (light blue diamonds) with error bars (light blue). Lower panel: differences between the sets of estimates in unit of sigma (same conventions as upper panel).

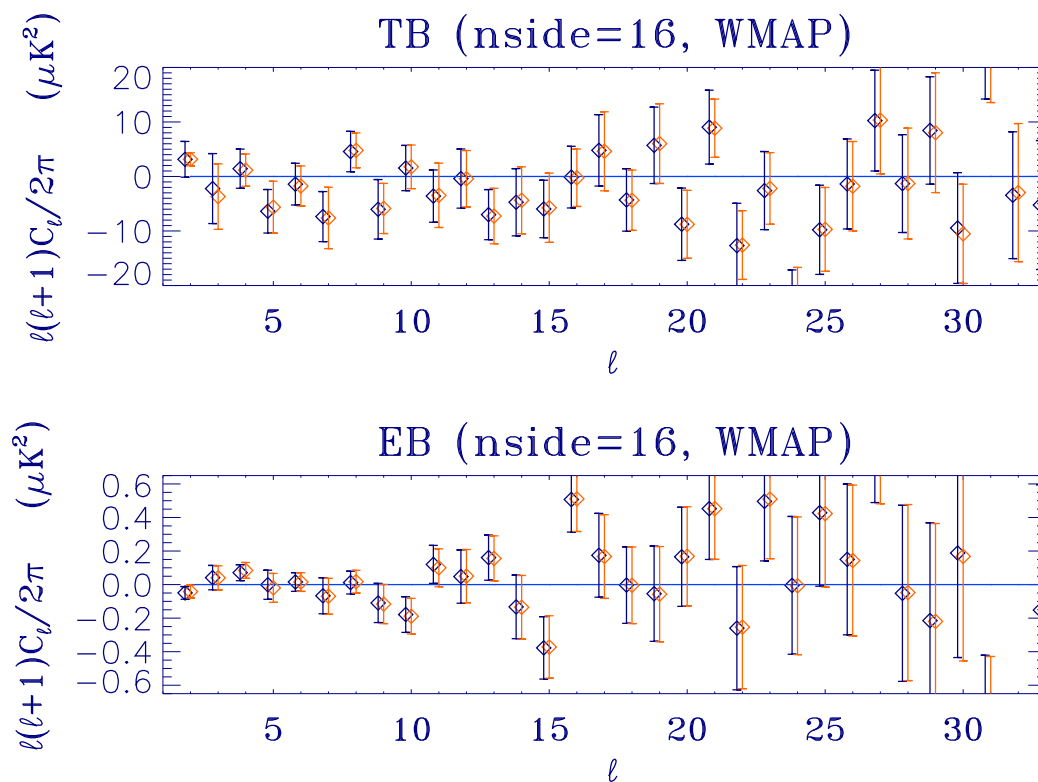
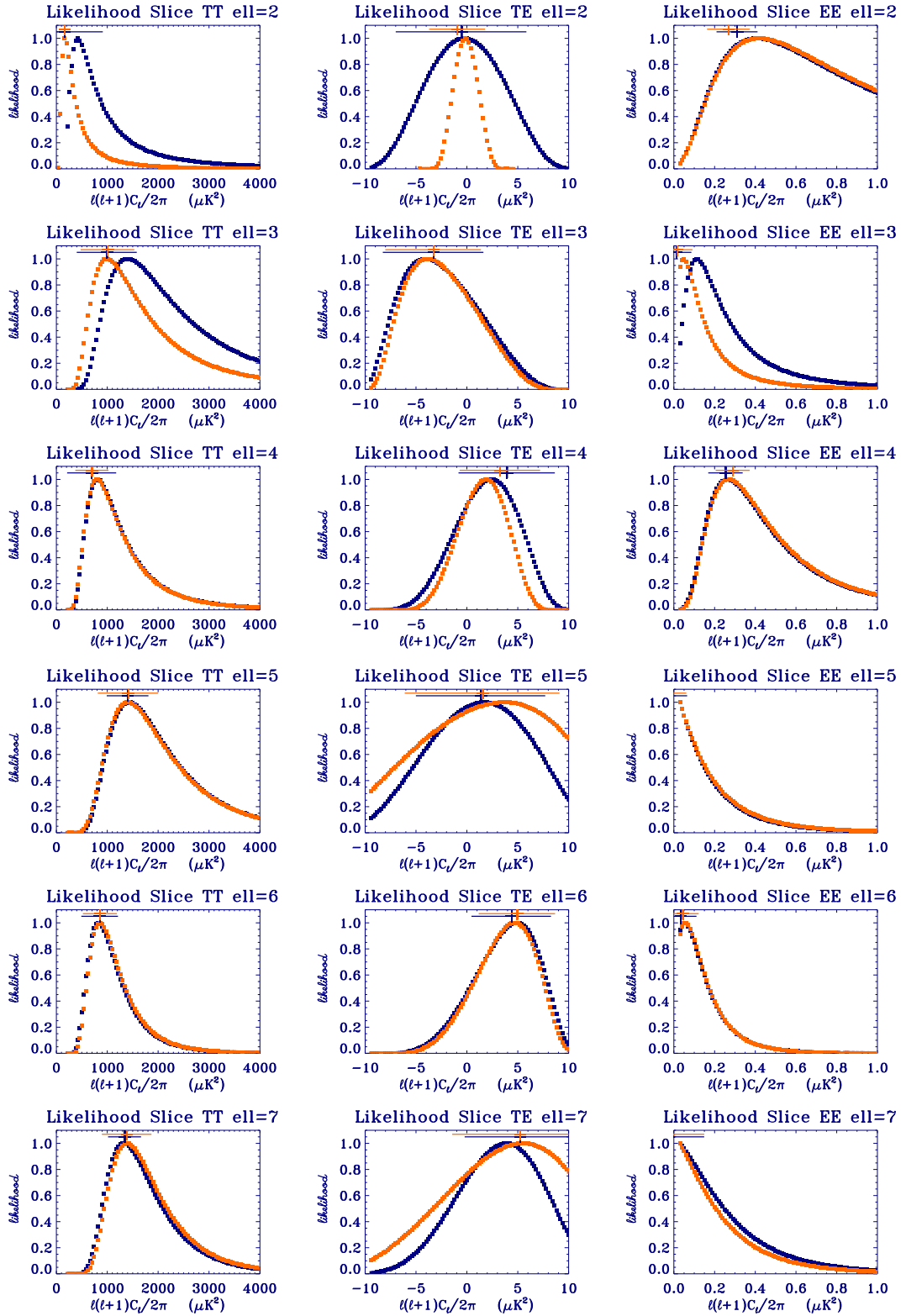


Figure 4.13: BolPol estimates of TB (upper panel) and EB (lower panel) angular power spectra from WMAP 5 year data at low resolution. Dark blue symbols are for the not iterated case and red for the iterated case.



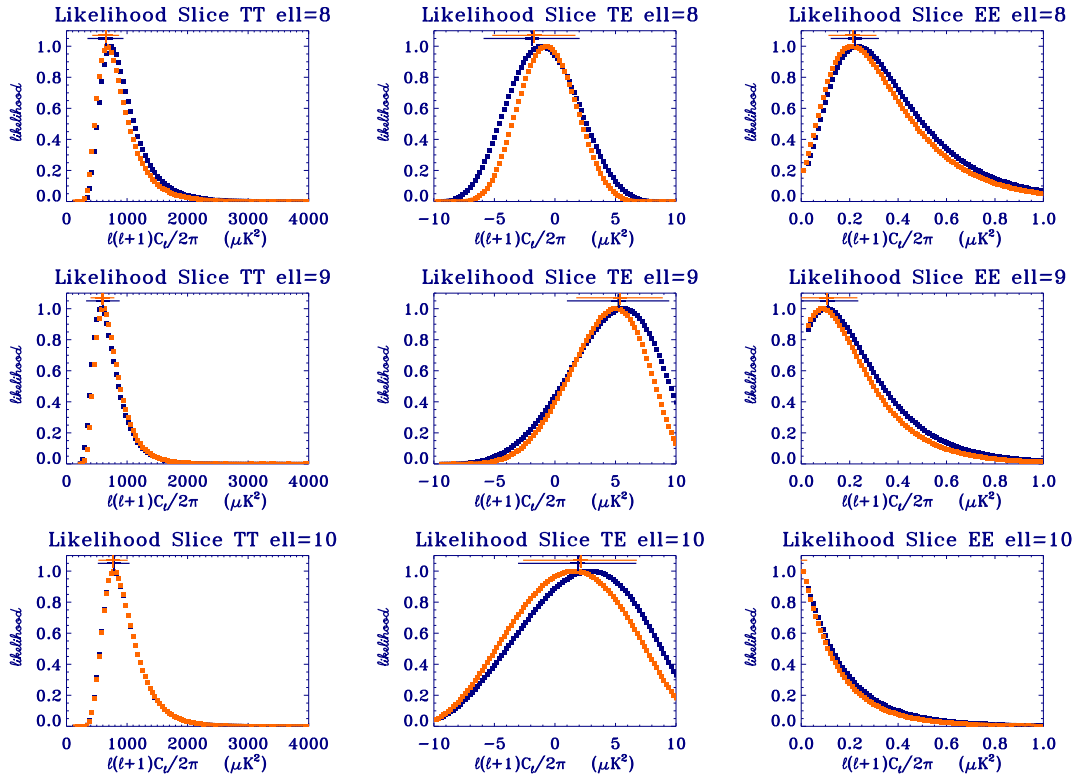
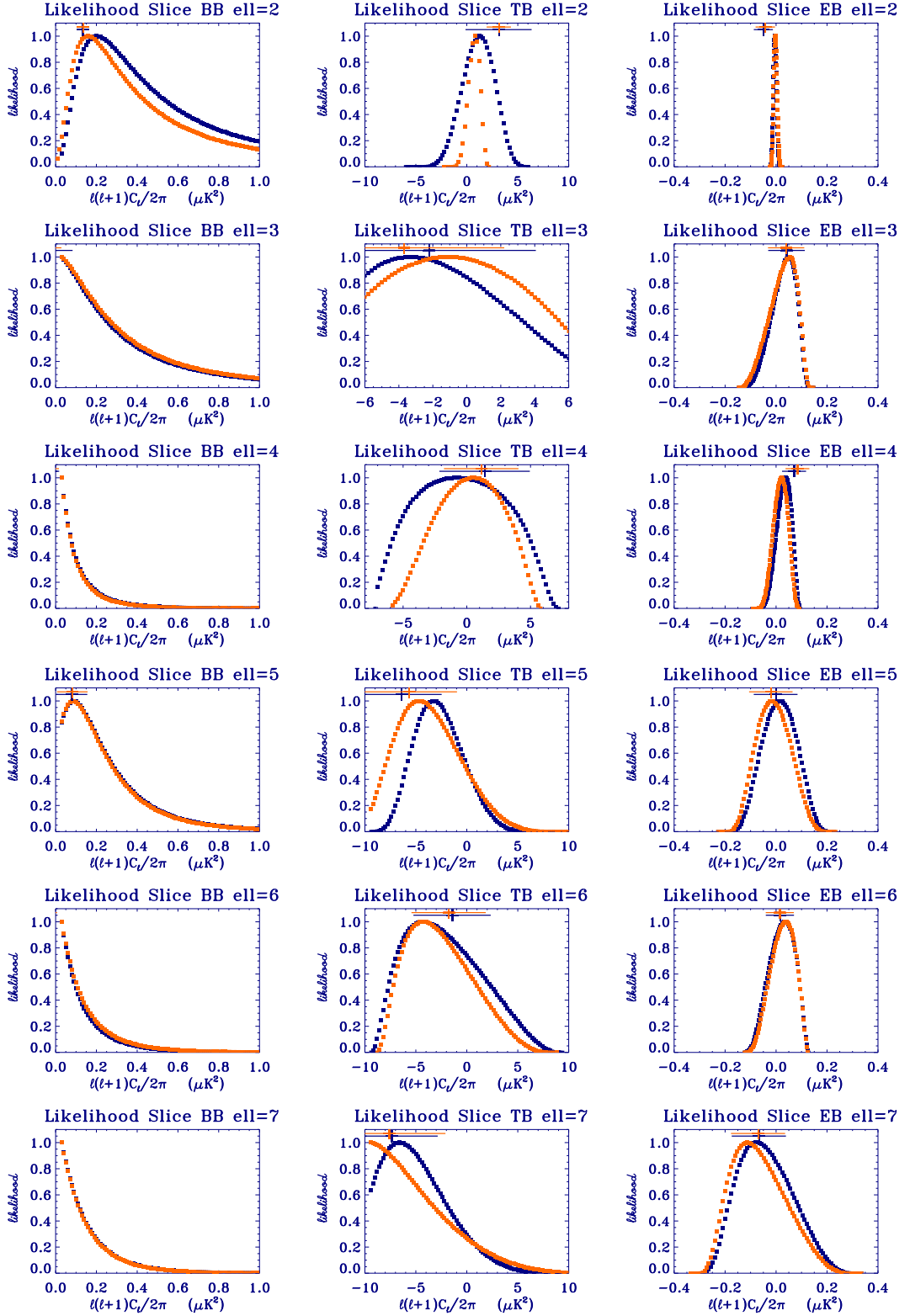


Figure 4.14: Likelihood Slices for TT, TE and EE from  $\ell = 2$  to 10 for the WMAP 5 year data at low resolution (i.e.  $n_{\text{side}} = 16$ ). Blue slices are for the not iterated case and the red ones for the iterated case. The blue plus represent the not iterated *BolPol* estimate with error bars (blue horizontal line) and the red plus the iterated ones.



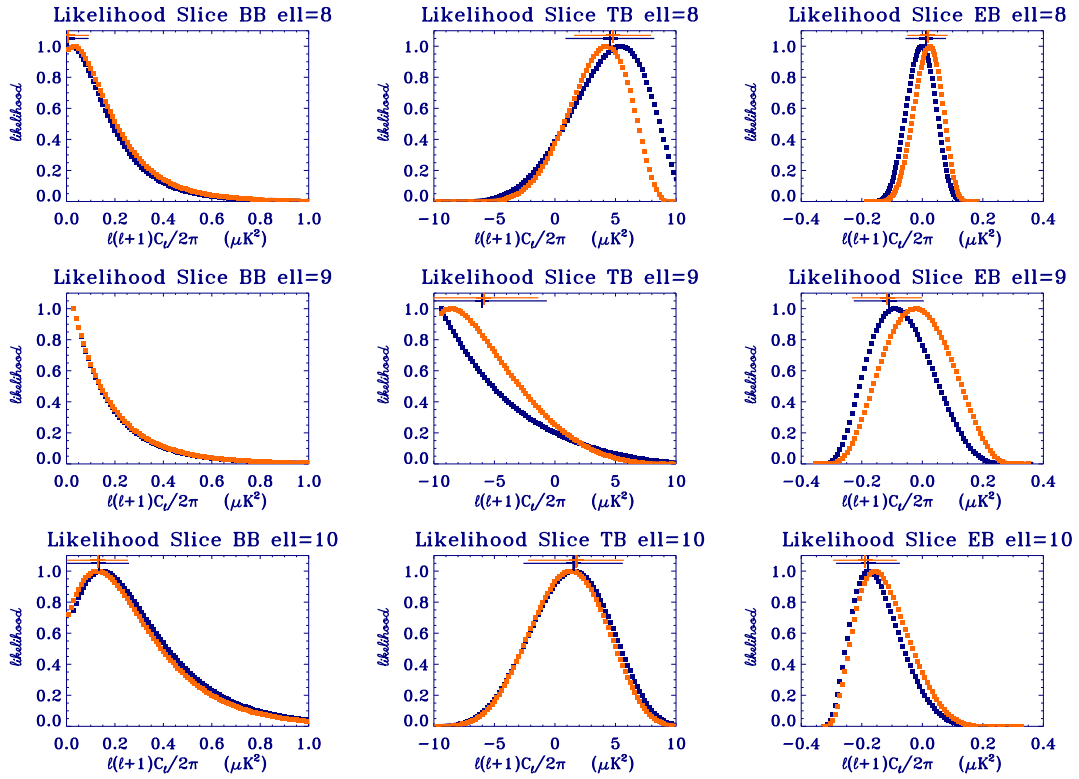


Figure 4.15: Likelihood Slices for BB, TB and EB from  $\ell = 2$  to 10 for the WMAP 5 year data at low resolution (i.e.  $n_{\text{side}} = 16$ ). Blue slices are for the not iterated case and the red ones for the iterated case. The blue plus represent the not iterated BolPol estimate with error bars (blue horizontal line) and the red plus the iterated ones.

another set of estimates with relative error bars, which is plotted in red. The iterated estimates are always very close to those obtained with the *WMAP5* best-fit as fiducial model: this means that QML estimates are sufficiently stable with respect to iteration. The same does not hold for error bars. In particular, the error on the *TT* quadrupole is substantially smaller, and a decrease of the error also occurs for  $\ell = 3, 4$  in temperature. Our estimate for the octupole in *BB* then is consistent with zero and very different from the one obtained by *WMAP* (note however that the *WMAP* likelihood slice for  $C_{\ell=3}^{BB}$  is not anomalous as the *WMAP* pseudo- $C_\ell$  estimate).

In the lower panels we show the differences between the two sets of estimates in unit of sigma (same conventions as upper panels). More precisely we show  $(C_\ell^{BolPol} - C_\ell^{WMAP})/\sigma$  where the *BolPol* estimates and  $\sigma$  are given by: *BolPol* estimates with *BolPol* error bars for the no-iteration case (dark blue lines); *BolPol* estimates in the no-iteration case and *WMAP* error bars (light blue line); *BolPol* estimates with *BolPol* error bars for the iteration case (red line).

We list now the reduced  $\chi^2$  values for the iterated *BolPol* estimates from  $\ell = 2$  to  $\ell = 32$  with respect to the *WMAP5* best-fit model:  $\chi_{TT}^2 = 4.423$  but excluding the quadrupole this value decreases to 1.079;  $\chi_{TE}^2 = 0.785$ ,  $\chi_{EE}^2 = 1.422$ ,  $\chi_{BB}^2 = 1.607$ .

We also plot the first and iterated *BolPol* estimates and relative error bars (in blue and red, respectively) for *TB* and *EB* (Fig. 4.13), but can not perform any comparison since these two polarizations are not provided in the LAMBDA web site. Also for these parity-odd correlators the QML estimates are very stable with respect to the iteration. Note how the error bars in *TB* change (due to substantially different fiducial model in *TT* in the iterated run), whereas those in *EB* not (since the fiducial *EE* and *BB* spectra are mainly unchanged during the iteration). The *TB* null reduced  $\chi^2$  for  $\ell = 2 - 23$  is 1.34 to be compared with 0.97 quoted for  $\ell = 24 - 450$  by the *WMAP* team. The *EB* null reduced  $\chi^2$  for  $\ell = 2 - 23$  is 1.14.

So far, we have used the Fisher information as the error associated to the estimates. However, it is known that at low multipoles the probability distribution for the  $C_\ell$  significantly deviates from being Gaussian, making the errors not symmetric. We therefore evaluate the conditional likelihood slices for the six spectra from  $\ell = 2$  to 10; we present these results in Figs. (??). As for the QML, we compute the slices on the *WMAP5* best-fit (blue points) and on the *BolPol* estimates (orange points obtained with the same fiducial used for the iterated QML run). It is important to note that the peaks of the likelihood slices are very different for the two sets of conditionings: the quadrupole in temperature is the most striking example. We do not observe

such dependence on the fiducial model in the estimates in the QML method. As for the errors of the QML method, also the shape of the conditional slices depends on the fiducial model. The trend in the iteration is the same of the one observed for the QML: confidence levels shrink by feeding the iterated QML estimates as conditioning.

For comparison with the QML, we also plot the QML estimate and error bars on top of the likelihood curves (blue for the first *BolPol* run and orange for the iterated one). The peaks of the likelihood slices are always consistent with the QML estimates within the error bars for both conditioning: however, an excellent agreement emerges when the QML estimates are used as conditioning.

Few results deserve to be commented for their cosmological importance. Our estimate (position of the peak) for the  $\ell(\ell + 1)C_\ell^{TT}/(2\pi)|_{\ell=2}$  is  $165 \mu K^2$  for the iterated QML (pixel base likelihood code). Basing on our pixel likelihood code *BoLike*, the conditional likelihood (normalized to 1) for  $\ell(\ell + 1)C_\ell^{TT}/(2\pi)|_{\ell=2}$  is larger than 0.05 between  $50 \mu K^2$  and  $1305 \mu K^2$ . This range has to be compared with the one given in Fig. 4 of [93].



# Conclusions

The pattern of CMB anisotropies is enclosing information on most of the cosmological history of our universe. Ground experiments, balloons and space satellites have been able to collect an incredible amount of information and new generation experiments are continuously planned for the future. In the immediate future, the *Planck* satellite will be launched - date is April 29th at present - and its scientific capabilities can generate another revolution in the understanding of cosmology. With its very low sensitivity and the ideal observational strategy - full sky from L2 -, *Planck* can improve the knowledge of CMB polarization. *Planck* is expected to improve the present constraints on  $B$  polarization and has the detector sensitivity potentially able to detect large field inflationary model such as  $m^2\phi^2$  [49].

In this thesis we have presented original work on the theory of primordial tensor modes and their possible detection through CMB polarization, specific for the *Planck* mission.

An analytical derivation about the coupling of gravitational waves with free-streaming matter - as neutrinos - has been presented. We have shown the relation between the Boltzmann hierarchy of coupled differential equations for the angular moments of the distribution function and the integro-differential approach of Weinberg [51]. In the first case, we see by numerical integration of the Einstein equations for tensors that the truncation of the neutrino hierarchy can be made at very low multipole, without any significant loss of information. The same rapid convergence is seen by performing different truncations of the neutrino hierarchy in the CAMB code. We have shown that the effect of free-streaming matter decreases the amplitude of  $C_\ell^{BB}$  in a range of multipoles above the first peak position ( $\ell \sim 90$ ). We have thus considered the evolution of tensor modes when a fully inhomogeneous component - as a stochastic background of primordial magnetic fields - is present (see also Appendix A for a study of scalar and vector perturbations). In the case with magnetic fields the interaction with neutrinos drastically changes the behaviour of gravitational waves. This interaction is characterized by

a compensation between the anisotropic stress of neutrinos and the one by magnetic fields. We found the analytical expressions for the convolution integrals which represent the energy-momentum tensor of PMF. By feeding the correct equations for tensors (scalar and vectors have been consistently treated as well) in a modified version of the CAMB code, we are able to simulate the magnetic contribution to CMB angular power spectra. It turns out that the tensor mode is subdominant with respect to the scalar and vector magnetic contribution. By switching off the neutrino interaction with tensors, the absence of compensation with magnetic modes leads to a much higher contribution to  $B$ -modes from magnetic fields. As a second part of the theoretical chapter, we have also presented results on the energy-momentum tensor associated to gravitational waves. We performed the integration over Fourier space of energy density and pressure, showing that tensor modes can be described as a viscous fluid whose equation of state tracks the cosmological expansion. We have shown how an additional term in the energy density does not lead to any significant modification for the direct detection of gravitational waves, being its contribution negligible at high frequencies. We have however shown that it is important to include it in a fluid treatment.

We moved then to testing and developing techniques and software for the data analysis for the *Planck* mission. We have presented a test of the Internal Linear Combination method for foreground cleaning on simulated polarization maps at low resolution. CMB and foreground have been simulated for the 70, 100, 143 and 217GHz channel with the Planck Sky Model and a mask has been applied to cover the most contaminated region. We found that, in the absence of instrumental noise, Internal Linear Combination of CMB maps which contain no tensor contribution provides cleaned polarization maps with an excess of variance comparable to the contribution of  $B$ -modes with a tensor-scalar ratio  $r = 0.1$ . Such residuals are mainly due to the cross-correlation between CMB and foregrounds and induce a non-negligible offset on the posterior for  $r$ , strongly dependent on the CMB realization analysed. Moreover, some of the ILC coefficients are larger than unity and would lead, for the *Planck* sensitivities, to a large noise level for the ILC cleaned map. We suggested as alternative method for foreground removal at low resolution, the use of internal templates, and tested it in the simplified case of no-noise. By taking two *Planck* channels as internal templates, we found in the absence of noise a posterior for  $r$  much narrower than we did with ILC.

A new pixel based power spectrum estimation code has been presented in the last chapter, *BolPol*, together with a likelihood code which uses some of

the same subroutines, *BoLike*. *BolPol* is a Fortran 90 parallel implementation of the Quadratic Maximum Likelihood method [88, 89], which provides optimal estimates and minimum variance error bars for all the six angular power spectra ( $TT$ ,  $EE$ ,  $TE$ ,  $BB$ ,  $TB$ ,  $EB$ ). At present *BolPol* can work at resolution  $N_{\text{side}} = 32$ , a resolution which provides reliable estimates and errors up to  $\ell \sim 64$ . It can deal with different masks for temperature and polarization and with a full noise covariance matrix (not only its diagonal elements). We have shown how it improves on the *Pseudo- $C_\ell$*  approach for *Planck* simulated data either in terms of less scattered estimates around the theoretical model or in terms of smaller error associated. An application to real data has also been performed. We have applied *BolPol* to the public *WMAP5* low resolution data-set ( $N_{\text{side}} = 16$ ) and found a substantial agreement with the *WMAP* team results. By iterating the QML method, we found that the estimates show a good stability, whereas error bars loose dependence on the fiducial model. We used *BoLike* to produce conditional slices for the first nine multipoles assuming as fiducial model either the *WMAP5* best-fit model or the *BolPol* estimates. The impact of iteration is much more evident in the likelihood analysis, consistently with what we saw for errors. Consistently with the iteration procedure we adopted, we found an improvement on the  $TT$  and  $TE$  spectra, with the others almost unchanged. We have shown how a parallel version of the QML or a pixel-based likelihood code is an excellent tool for low resolution data analysis. The present capabilities of *BolPol* - able to run on maps at resolution  $N_{\text{side}} = 32$  to provide unbinned estimates of all the six power spectra - is already sufficient to handle  $N_{\text{side}} = 64$  maps and estimate power spectra with a light binning. Such map resolutions would allow us to explore the multipoles where the  $BB$  signal generated by primordial gravitational waves with a scale invariant spectrum would be maximum. Our implementation of the QML method and a pixel-based likelihood code is therefore ready not only for *Planck*, but also for the next generation of experiments which target the  $BB$  polarization signal generated by inflation.



# Appendix A

## Scalar and vectors magnetic modes

In this appendix we summarise our results for scalar and vector magnetic modes as well. More details can be found in Finelli, Paci, Paoletti, *Physical Review D*, 78, 023510 (2008) [63] and in Paoletti, Finelli, Paci [arXiv:0811.0230], submitted for publication on MNRAS [64]

We choose to work in the synchronous gauge, where the scalar metric perturbations are described in Fourier space by two scalar potentials,  $h$  and  $\eta$ . In this appendix we denote the conformal time by  $\tau$ . In presence of magnetic fields, Einstein equations for scalars are

$$\begin{aligned} k^2\eta - \frac{1}{2}\mathcal{H}h' &= 4\pi Ga^2(\Sigma_n \rho_n \delta_n + \rho_B), \\ k^2\eta' &= 4\pi Ga^2 \Sigma_n (\rho_n + P_n)\theta_n, \\ h'' + 2\mathcal{H}h' - 2k^2\eta &= -8\pi Ga^2(\Sigma_n c_{sn}^2 \rho_n \delta_n + \frac{\delta\rho_B}{3}), \\ h'' + 6\eta'' + 2\mathcal{H}(h' + 6\eta') - 2k^2\eta &= -24\pi Ga^2[\Sigma_n(\rho_n + P_n)\sigma_n + \sigma_B], \end{aligned} \tag{A.1}$$

where  $n$  represents the various species of the plasma, i.e. baryons, cold dark matter (CDM), photons and massless neutrinos. For vectors, instead, we have

$$h'^V + 2\mathcal{H}h^V = -16\pi Ga^2(\Pi_\nu^{(V)} + \Pi_\gamma^{(V)} + \Pi_B^{(V)})/k. \tag{A.2}$$

Energy-density conservation leads to a relation for scalars between energy density, scalar anisotropic stress and Lorentz force induced by magnetic fields on baryons. A similar relation holds for the vector contribution at the

anisotropic stress and the Lorentz force. Thus, we need to compute only three quantities out of the five. We chose the following

$$\begin{aligned}
|\rho_B(k)|^2 &= \frac{1}{1024\pi^5} \int d\mathbf{p} P_B(p) P_B(|\mathbf{k} - \mathbf{p}|) (1 + \mu^2) \\
|\Pi^{(V)}(k)|^2 &= \frac{1}{512\pi^5} \int d\mathbf{p} P_B(p) P_B(|\mathbf{k} - \mathbf{p}|) [(1 + \beta^2)(1 - \gamma^2) + \gamma\beta(\mu - \gamma\beta)] \\
|L(k)|^2 &= \frac{1}{1024\pi^5 a^8} \int d\mathbf{p} P_B(p) P_B(|\mathbf{k} - \mathbf{p}|) [1 + \mu^2 + 4\gamma\beta(\gamma\beta - \mu)]. \quad (\text{A.3})
\end{aligned}$$

Both for scalars and vectors, the Lorence force induced on baryons modifies the velocity equation. The magnetized adiabatic mode initial conditions we found are:

$$\begin{aligned}
h &= C_1 k^2 \tau^2 \\
\eta &= 2C_1 - \frac{5 + 4R_\nu}{6(15 + 4R_\nu)} C_1 k^2 \tau^2 - \left[ \frac{\Omega_B(17 - 14R_\nu)}{28(15 + 4R_\nu)} + \frac{23L_B}{28(15 + 4R_\nu)} \right] k^2 \tau^2 \\
\delta_\gamma &= -\Omega_B - \frac{2}{3} C_1 k^2 \tau^2 + \left[ \frac{\Omega_B}{6} + \frac{L_B}{2(1 - R_\nu)} \right] k^2 \tau^2 \\
\delta_\nu &= -\Omega_B - \frac{2}{3} C_1 k^2 \tau^2 - \left[ \frac{\Omega_B(1 - R_\nu)}{6R_\nu} + \frac{L_B}{2R_\nu} \right] k^2 \tau^2 \\
\delta_b &= -\frac{3}{4} \Omega_B - \frac{C_1}{2} (k\tau)^2 + \left[ \frac{\Omega_B}{8} + \frac{3L_B}{8(1 - R_\nu)} \right] k^2 \tau^2 \\
\delta_c &= -\frac{C_1}{2} k^2 \tau^2 \\
\theta_\gamma &= -\frac{C_1}{18} k^4 \tau^3 - \left[ \frac{\Omega_B}{4} + \frac{3}{4} \frac{L_B}{(1 - R_\nu)} \right] k^2 \tau + \left[ \frac{\Omega_B}{72} + \frac{L_B}{24(1 - R_\nu)} \right] k^4 \tau^3 \\
\theta_b &= \theta_\gamma \\
\theta_c &= 0 \\
\theta_\nu &= -\frac{(23 + 4R_\nu)}{18(15 + 4R_\nu)} C_1 k^4 \tau^3 + \left[ \frac{\Omega_B(1 - R_\nu)}{4R_\nu} + \frac{3}{4} \frac{L_B}{R_\nu} \right] k^2 \tau \\
&\quad + \left[ \frac{(411 - 7R_\nu(47 + 4R_\nu))\Omega_B}{504R_\nu(15 + 4R_\nu)} + \frac{(33 - 28R_\nu)L_B}{168R_\nu(15 + 4R_\nu)} \right] k^4 \tau^3 \\
\sigma_\nu &= \frac{4C_1}{3(15 + 4R_\nu)} k^2 \tau^2 - \frac{\Omega_B}{4R_\nu} - \frac{3}{4} \frac{L_B}{R_\nu} + \left[ \frac{3\Omega_B(17 - 14R_\nu)}{(15 + 4R_\nu)} + \frac{69L_B}{(15 + 4R_\nu)} \right] \frac{k^2 \tau^2}{28R_\nu} \\
F_{3\nu} &= -\frac{6}{7} \left[ \frac{\Omega_B}{4R_\nu} + \frac{3}{4} \frac{L_B}{R_\nu} \right] k\tau. \quad (\text{A.4})
\end{aligned}$$

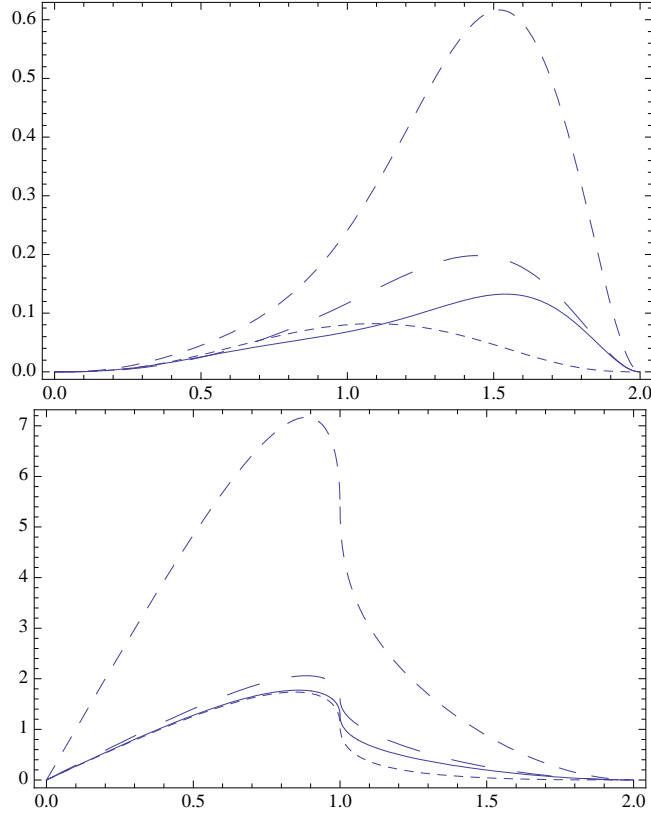


Figure A.1: Comparison of  $k^3|\rho_B(k)|^2$  (solid line),  $k^3|L(k)|^2$  (large dashed line),  $k^3|\Pi_i^{(V)}(k)|^2$  (small dashed line),  $k^3|\Pi_{ij}^{(T)}(k)|^2$  (medium dashed line) in units of  $\langle B^2 \rangle^2 / (1024\pi^3)$  versus  $k/k_D$ . The two panels are for  $n_B = 2$  (top) and  $n_B = -5/2$  (bottom).

In Fig.(A.1) we show a comparison among the scalar, vector and tensor convolutions for the two cases  $n_B = -2.5$  and 2.

In Fig. (A.2), instead, we show the scalar, vector and tensor contribution to the CMB angular power spectra for the  $TT$ ,  $TE$  and  $EE$  polarizations (once again for  $n_B = 2$  and  $n_B = -2.5$ ).

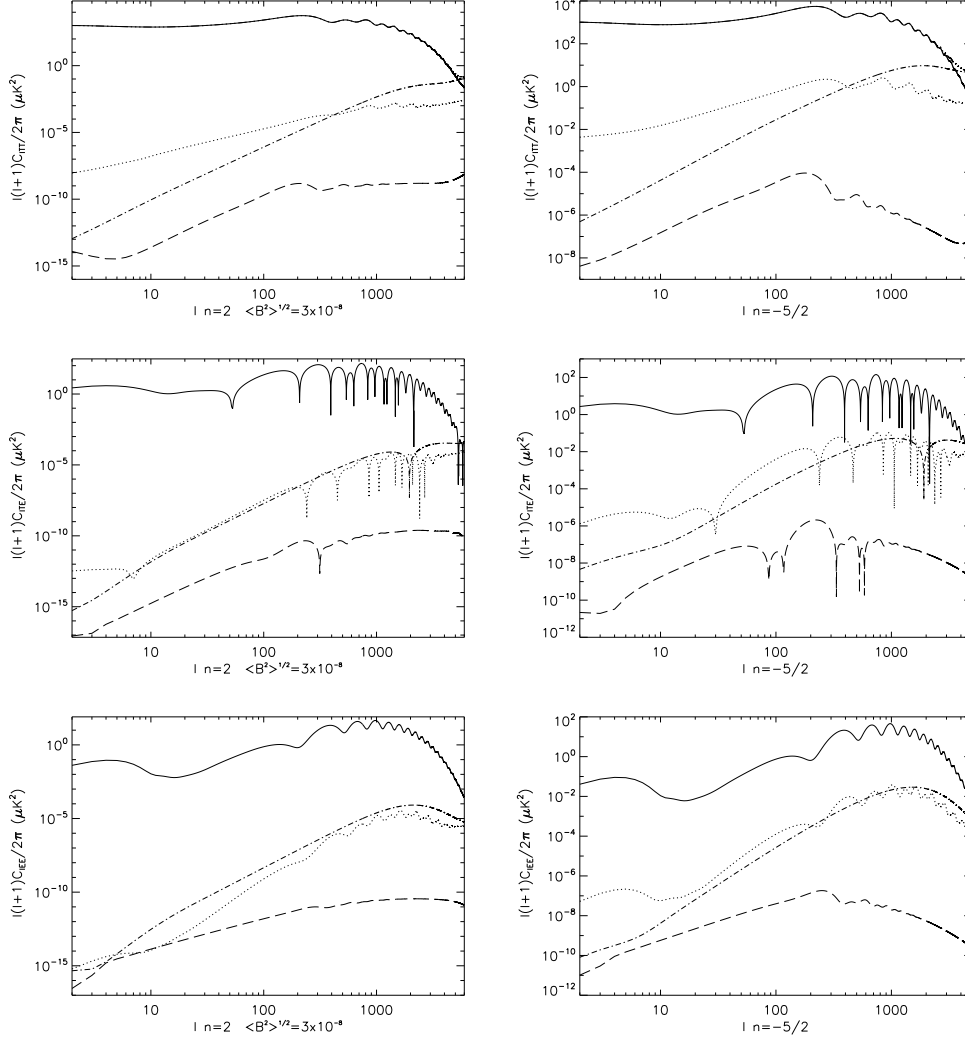


Figure A.2: CMB angular power spectrum for TT (top panels), TE (center panels), EE (bottom left) for  $n_B = 2$  (left column) and  $n_B = -2.5$  (right column). The solid line is the adiabatic scalar contribution; the dotted, dot-dashed, dashed are the scalar, vector and tensor contributions of a SB of PMF respectively for  $\sqrt{\langle B^2 \rangle} = 7.5$  nG and  $k_D = 2\pi \text{ Mpc}^{-1}$ . The cosmological parameters of the flat  $\Lambda\text{CDM}$  model are  $\Omega_b h^2 = 0.022$ ,  $\Omega_c h^2 = 0.123$ ,  $z_{\text{re}} = 12$ ,  $n_s = 1$ ,  $H_0 = 100 h \text{ km s}^{-1} \text{ Mpc}^{-1} = 72 \text{ km s}^{-1} \text{ Mpc}^{-1}$ .

# Appendix B

## EMT integrals

In this appendix we compute explicitly the relevant energy momentum tensor components for gravitational waves, i.e. energy density and isotropic pressure. The starting point are the following two integrals in Fourier space:

$$\begin{aligned}\epsilon &= \frac{M_{\text{pl}}^2}{4\pi^2 a^2} \int_0^\infty k^2 dk [ |h'_k|^2 + k^2 |h_k|^2 + 8\mathcal{H} |h'_k h_k| ] \\ p &= \frac{M_{\text{pl}}^2}{12\pi^2 a^2} \int_0^\infty k^2 dk [ -5|h'_k|^2 + 7k^2|h_k|^2 ]\end{aligned}\quad (\text{B.1})$$

We assume a power law expansion of the scale factor in conformal time,

$$a(\eta) = a_* \eta^\beta \quad a'(\eta) = a_* \beta \eta^{\beta-1} \quad \mathcal{H} = \frac{\beta}{\eta}, \quad (\text{B.2})$$

where we remind that  $\beta = 1$  for radiation and  $\beta = 2$  for matter, and keep only the growing mode of tensor modes

$$h_k = A_k \frac{J_{\beta-1/2}(k\eta)}{(k\eta)^{\beta-1/2}} \quad h'_k = -A_k k \frac{J_{\beta+1/2}(k\eta)}{(k\eta)^{\beta-1/2}} \quad (\text{B.3})$$

where  $A_k = \tilde{A} k^{-3+n_T}$ . The three quantities which need to be integrated are the following

$$\begin{aligned}k^2 |h'_k|^2 &= \frac{\tilde{A}^2}{\eta^{2\beta-1}} k^{2-2\beta+n_T} J_{\beta+1/2}^2(k\eta) \\ k^4 |h_k|^2 &= \frac{\tilde{A}^2}{\eta^{2\beta-1}} k^{2-2\beta+n_T} J_{\beta-1/2}^2(k\eta) \\ k^2 h_k h'_k &= -\frac{\tilde{A}^2}{\eta^{2\beta-1}} k^{1-2\beta+n_T} J_{\beta-1/2}^2(k\eta) J_{\beta+1/2}^2(k\eta).\end{aligned}\quad (\text{B.4})$$

For each of the we give the result together with the parameter region  $(n_T, \beta)$  allowed by the convergence of the integral.

- *first integral*

convergence for  $-4 < n_T < 2\beta - 2$

$$\begin{aligned} \int_0^\infty dk k^2 |h'_k|^2 &= \frac{\tilde{A}^2}{\eta^{2\beta-1}} \int_0^\infty dk k^{2-2\beta+n_T} J_{\beta+1/2}^2(k\eta) \\ &= \frac{\tilde{A}^2 \eta^{-n_T-2}}{2^{2\beta-n_T-2}} \frac{\Gamma(2\beta - n_T - 2) \Gamma(2 + \frac{n_T}{2})}{\Gamma^2(\frac{2\beta-n_T-1}{2}) \Gamma(2\beta - \frac{n_T}{2})} \end{aligned} \quad (\text{B.5})$$

- *second integral*

convergence for  $-2 < n_T < 2\beta - 2$

$$\begin{aligned} \int_0^\infty dk k^4 |h_k|^2 &= \frac{\tilde{A}^2}{\eta^{2\beta-1}} \int_0^\infty dk k^{2-2\beta+n_T} J_{\beta-1/2}^2(k\eta) \\ &= \frac{\tilde{A}^2 \eta^{-n_T-2}}{2^{2\beta-n_T-2}} \frac{\Gamma(2\beta - n_T - 2) \Gamma(1 + \frac{n_T}{2})}{\Gamma^2(\frac{2\beta-n_T-1}{2}) \Gamma(2\beta - \frac{n_T}{2} - 1)} \end{aligned} \quad (\text{B.6})$$

- *third integral*

convergence for  $-2 < n_T < 2\beta - 1$

$$\begin{aligned} \int_0^\infty dk k^2 |h_k h'_k| &= -\frac{\tilde{A}^2}{\eta^{2\beta-1}} \int_0^\infty dk k^{1-2\beta+n_T} J_{\beta-1/2}^2(k\eta) J_{\beta+1/2}^2(k\eta) \\ &= \frac{\tilde{A}^2 \eta^{-n_T-1}}{2^{2\beta-n_T-1}} \frac{\Gamma(2\beta - n_T - 1) \Gamma(1 + \frac{n_T}{2})}{\Gamma(\frac{2\beta-n_T-1}{2}) \Gamma(\frac{2\beta-n_T+1}{2}) \Gamma(2\beta - \frac{n_T}{2})} \end{aligned} \quad (\text{B.7})$$

Note that without any cut-off scale, the laplacian and kinetic term diverge in radiation era for a pure scale-invariant spectrum ( $n_T = 0$ ).

# Appendix C

## QML derivation

In this appendix we provide a derivation of the QML algebra, extending the details of Ref. [88]

We look for estimates which are quadratic on the data

$$\tilde{C}_\ell = \mathbf{x}^t \mathbf{E}_\ell \mathbf{x}, \quad (\text{C.1})$$

where  $\mathbf{x}$  is the data vector and  $\mathbf{E}_\ell$  is the object we want to find. Introducing the covariance matrix and using the addition theorem for spherical harmonics we can write

$$\langle \mathbf{x} \mathbf{x}^t \rangle = \mathbf{C} = \sum_{\ell'} \mathbf{P}_{\ell'} C_{\ell'} \quad (\text{C.2})$$

from which

$$\langle \tilde{C}_\ell \rangle = \text{tr}[\mathbf{E}_\ell \mathbf{C}] = \text{tr}[\mathbf{E}_\ell \sum_{\ell'} \mathbf{P}_{\ell'} C_{\ell'}] = \sum_{\ell'} \text{tr}[\mathbf{E}_\ell \mathbf{P}_{\ell'}] C_{\ell'} \quad (\text{C.3})$$

and the covariance is

$$V_{\ell\ell'} = \langle \tilde{C}_\ell \tilde{C}_{\ell'} \rangle - \langle \tilde{C}_\ell \rangle \langle \tilde{C}_{\ell'} \rangle = 2 \text{tr}[\mathbf{C} \mathbf{E}_\ell \mathbf{C} \mathbf{E}_{\ell'}]. \quad (\text{C.4})$$

We need to minimise  $V_{\ell\ell'}$  under the condition that

$$\text{tr}[\mathbf{E}_\ell \mathbf{P}_{\ell'}] = 1. \quad (\text{C.5})$$

To do this we go through the Lagrange multipliers procedure.

$$L = \text{tr}[\mathbf{C} \mathbf{E}_\ell \mathbf{C} \mathbf{E}_{\ell'} - 2\lambda(\mathbf{P}_\ell \mathbf{E}_\ell - 1)], \quad (\text{C.6})$$

$$\frac{\partial L}{\partial \mathbf{E}} = 0 \quad \rightarrow \quad \mathbf{C} \mathbf{E}_\ell \mathbf{C} = \lambda \mathbf{P}_\ell \quad \rightarrow \quad \mathbf{E}_\ell = \lambda \mathbf{C}^{-1} \mathbf{P}_\ell \mathbf{C}^{-1}. \quad (\text{C.7})$$

Feeding this expression for  $\mathbf{E}$  into Eq. (C.5), we get

$$\lambda = \frac{1}{\text{tr}[\mathbf{C}^{-1}\mathbf{P}_\ell\mathbf{C}^{-1}P_\ell]} = \frac{1}{2F_{\ell\ell}} \quad (\text{C.8})$$

where the Fisher matrix  $F$  has been introduced and the final expression for  $\mathbf{E}_\ell$  takes the form

$$\mathbf{E}_\ell = \frac{1}{2F_{\ell\ell}}\mathbf{C}^{-1}\mathbf{P}_\ell\mathbf{C}^{-1}. \quad (\text{C.9})$$

We define now a rescaling of the estimator  $\tilde{C}_\ell$  by

$$y_\ell = F_{\ell\ell}\tilde{C}_\ell \quad (\text{C.10})$$

and see that its average value is

$$\langle y_\ell \rangle = F_{\ell\ell}\langle \tilde{C}_\ell \rangle = F_{\ell\ell}C_{\ell'}. \quad (\text{C.11})$$

Finally, we define a new estimator as

$$\hat{C}_\ell = F_{\ell\ell}^{-1}y_{\ell'}. \quad (\text{C.12})$$

whose mean is

$$\langle \hat{C}_\ell \rangle = F_{\ell\ell}^{-1}\langle y_{\ell'} \rangle = F_{\ell\ell}^{-1}F_{\ell'\ell''}C_{\ell''} = \delta_{\ell\ell''}C_{\ell''} = C_\ell \quad (\text{C.13})$$

and its covariance is

$$\begin{aligned} \langle (\hat{C}_\ell - C_\ell)(\hat{C}_\ell - C_\ell)^t \rangle &= \langle \hat{C}_\ell \hat{C}_{\ell'}^t - C_\ell \hat{C}_{\ell'}^t - \hat{C}_\ell C_{\ell'} + C_\ell C_{\ell'} \rangle \\ &= \langle \hat{C}_\ell \hat{C}_{\ell'}^t - C_\ell C_{\ell'} \rangle \\ &= \langle F_{\ell\ell'}^{-1}y_{\ell''}y_{\ell'''}F_{\ell''\ell'''}^{-1} \rangle - C_\ell C_{\ell'}' \\ &= F_{\ell\ell'}^{-1}(F_{\ell''\ell'''} + \langle y_{\ell''} \rangle \langle y_{\ell'''} \rangle^t)F_{\ell''\ell'''}^{-1} - C_\ell C_{\ell'}' \\ &= F_{\ell\ell'}^{-1} + \langle \hat{C}_\ell \rangle + \langle \hat{C}_{\ell'} \rangle - C_\ell C_{\ell'}' = F_{\ell\ell'}^{-1} \end{aligned} \quad (\text{C.14})$$

Thus, we demonstrated that the estimator  $\hat{C}_\ell$  is unbiased and optimal, since its covariance matrix is the fisher matrix,  $F_{\ell\ell'}^{-1}$ , the best covariance matrix for an estimator [90].

# Bibliography

- [1] A. Guth, Physical Review D, 23, 347 (1981)
- [2] A. Linde, Physics Letters B 108, 389 (1982)
- [3] A. A. Starobinsky, Journal of Experimental and Theoretical Physics Letters 30, 682 (1979)
- [4] A. A. Starobinsky, Physics Letters B 117, 175 (1982)
- [5] A. Albrecht, P. J. Steinhardt, Physical Review Letters 48, 1220 (1982)
- [6] M. Gasperini, G. Veneziano, Physics Reptort, 373, 1 (2003)
- [7] J. Khoury *et al.* , Physical Review D, 64 123522 (2001)
- [8] F. Finelli, R. Brandenberger, Physical Review D, 65 103522 (2002)
- [9] A. G. Polnarev, Sov. Astron. 29, 607 (1985)
- [10] L. Knox, Y.-S. Song, Phys. Rev. Lett. 89, 011303 (2002) [astro-ph/0202286]
- [11] <http://lambda.gsfc.nasa.gov/product/cobe/>
- [12] <http://cmb.phys.cwru.edu/boomerang/>
- [13] <http://map.gsfc.nasa.gov/>
- [14] <http://cosmology.berkeley.edu/group/swlh/acbar/>
- [15] <http://astro.uchicago.edu/dasi/>
- [16] <http://www.astro.caltech.edu/tjp/CBI/>
- [17] <http://www-astro.physics.ox.ac.uk/research/expcosmology/groupclover.html>
- [18] [http://bicep0.caltech.edu/bicep/bicep\\_front.htm](http://bicep0.caltech.edu/bicep/bicep_front.htm)

- [19] <http://www.rssd.esa.int/index.php?project=planck>
- [20] <http://quiet.uchicago.edu/index.php>
- [21] <http://www.bpol.org/bpolscience.php>
- [22] <http://cmbpol.uchicago.edu/>
- [23] S. Burles, K. M. Nollett, M. S. Turner, astro-ph/9903300 (1999)
- [24] A. A. Penzias, R. W. Wilson, *Astrophysical Journal Letters* 142, 1149 (1965)
- [25] J. C. Mather, *Astrophysical Journal*, 512, 511 (1999)
- [26] S. Weinberg, *Gravitation and Cosmology* (Wiley, N.Y. 1973)
- [27] E. W. Kolb, M. S. Turner, *The Early Universe* (Addison-Wesley, Redwood City 1990)
- [28] P. Coles, F. Lucchin, *Cosmology* (Wiley, 2002)
- [29] S. Dodelson, *Modern Cosmology* (Academic Press, 2003)
- [30] V. Mukhanov, *Physical Foundation of Cosmology* (Cambridge University Press, 2005)
- [31] E. Hubble, *Proceedings of the National Academy of Science* 15, (1929)
- [32] W. Freedman *et al.* , *Astrophysical Journal* 553, 47 (2001)
- [33] J. D. Jackson, *Classical electrodynamics* (Wiley, N.Y. 1998)
- [34] J. M. Bardeen, P. J. Steinhardt, M. S. Turner, *Physical Review D*, 28, 679 (1983)
- [35] J. M. Bardeen, *Phys. Rev. D* 22, 1882 (1980)
- [36] H. Kodama, M. Sasaki, *Progress of Theoretical Physics Supplement* 78, 1984
- [37] V. F. Mukhanov, H. A. Feldman, R. H. Brandenberger, *Phys. Rep.* 215 1 (1992)
- [38] E. Bertschinger, in *Proc. Les Houches School, Session LX*, ed. R. Schaeffer *et al.* (Netherlands: Elsevier 1996) [astro-ph/9503125]

- [39] C.-P. Ma, E. Bertschinger, *Astrophysical Journal* 455, 7 (1995)
- [40] E. M. Lifshitz, *J. Phys (USSR)* 10, 116 (1946)
- [41] W. Hu, S. Dodelson, *Ann. Rev. Astron. Astrophys.* 40, 171 (2002) [astro-ph/0110414]
- [42] U. Seljak, *Astrophysical Journal* 435, L87 (1996)
- [43] W. Hu, N. Sugiyama, *Astrophysical Journal* 444, 489 (1995)
- [44] U. Seljak, M. Zaldarriaga, *ApJ* 469, 437 (1996) [astro-ph/9603033]
- [45] M. Zaldarriaga, Ph.D. Thesis, M.I.T. [astro-ph/9806122]
- [46] A. Lewis, A. Challinor, A. Lasenby, *Astrophysical Journal* 538, 473 (2000)
- [47] M. Bersanelli, N. Mandolesi, *Astrophysical Letters and Comments* 37, 171 (2000)
- [48] J.-M. Lamarre *et al.*, *SPIE*, 4850, 730 (2003)
- [49] G. Efstathiou, S. Gratton, F. Paci [arXiv:0902.4803]
- [50] S. W. Hawking, *Astrophysical Journal* 145, 544 (1966)
- [51] S. Weinberg, *Physical Review D* 69, 023503 (2004) [astro-ph/0306304]
- [52] S. Bashinsky, (2005) [astro-ph/0505502]
- [53] D. A. Dicus, W. W. Repko, *Physical Review D* 72, 088302 (2005)
- [54] Y. Watanabe, E. Komatsu, *Physical Review D* 73, 123515 (2005)
- [55] T. L. Smith, M. Kamionkowski, A. Cooray [astro-ph/0506422]
- [56] E. Komatsu *et al.*, *Astrophysical Journal Supplement Series*, 180, 330 (2009)
- [57] J. Dunkley *et al.*, *Astrophysical Journal Supplement Series*, 180, 306 (2009)
- [58] J. Lesgourgues, S. Pastor, *Physics Reports* 429, 307 (2006)
- [59] A. Dolgov [arXiv:0803:3887]

- [60] M. Zaldarriaga, U. Seljak, *Physical Review D* 55, 1830 (1997) [astro-ph/9609170]
- [61] J. R. Bond, A. S. Szalay, *ApJ* 274, 443 (1983)
- [62] R. Durrer, P. G. Ferreira, T. Kahniashvili, *Physical Review D* 61, 043001 (1999)
- [63] F. Finelli, F. Paci, D. Paoletti, *Physical Review D*, 78, 023510 (2008)
- [64] D. Paoletti, F. Finelli, F. Paci [arXiv:0811.0230]
- [65] A. Lewis, *Physical Review D*, 70, 043011 (2004)
- [66] L. R. W. Abramo, R. H. Brandenberger, V. F. Mukhanov, *Physical Review D*, 56, 3248 (1997)
- [67] L. R. Abramo, *Physical Review D*, 60, 064004 (1999)
- [68] F. Finelli *et al.*, *Physical Review D*, 71, 023522 (2005)
- [69] <http://www.ligo.caltech.edu/>
- [70] <http://lisa.nasa.gov/>
- [71] <http://tamago.mtk.nao.ac.jp/>
- [72] <http://www.geo600.de/>
- [73] <http://universe.nasa.gov/program/>
- [74] S. Kawamura, *Classical and Quantum Gravity* 23, S125 (2006)
- [75] G. B. Rybicki, A. Lightman, *Radiative Processes in Astrophysics* (Wiley, N. Y. 1979)
- [76] B. Gold, *Astrophysical Journal Supplement Series*, 180, 265 (2009)
- [77] C. L. Bennett *et al.*, *Astrophysical Journal Supplement Series*, 148, 97 (2003)
- [78] D. P. Finkbeiner, *Astrophysical Journal Supplement Series* 146, 407
- [79] B. G. Keating, *Astrophysical Journal* 495, 580 (1998)
- [80] D. P. Finkbeiner, M. Davis, D. J. Schlegel, *Astrophysical Journal* 524, 867 (1999)

- [81] S. M. Leach *et al.*, *Astronomy & Astrophysics* 491, 597 (2008)
- [82] M. Tegmark, G. Efstathiou, *Monthly Notices of the Royal Astronomical Society*, 281, 1297 (1996)
- [83] H. K. K. Eriksen *et al.*, *Astrophysical Journal* 612, 633
- [84] B. D. Wandelt, E. Hivon, K. M. Górski, *Physical Review D*, 64, 083003 (2001)
- [85] E. Hivon *et al.*, *Astrophysical Journal*, 567, 2 (2002)
- [86] G. Efstathiou, *Monthly Notices of the Royal Astronomical Society*, 349, 603 (2004)
- [87] G. Efstathiou, *Monthly Notices of the Royal Astronomical Society*, 370, 343 (2006)
- [88] M. Tegmark, *Physical Review D*, 55, 5895 (1997)
- [89] M. Tegmark, A. de Oliveira-Costa, *Physical Review D*, 64, 063001 (2001)
- [90] M. Tegmark, A. N. Taylor, A. F. Heavens, *Astrophysical Journal* 480, 22 (1997)
- [91] E. Keihänen, H. Kurki-Suonio, T. Poutanen, *Monthly Notices of the Royal Astronomical Society*, 360, 390 (2005)
- [92] K. M. Gorski *et al.*, *Astrophysical Journal*, 622, 759 (2005)
- [93] J. Dunkley *et al.*, *Astrophysical Journal Supplement Series* 180, 306 (2009) [arXiv:0803.0586]
- [94] The *Planck* collaboration, 'The scientific Program of *Planck*', eds. Efstathiou, Lawrence, Tauber, ESA-SCI (2005), ESA Publications
- [95] B. Schutz, *A first course in general relativity* (Cambridge University Press, 1985)
- [96] M. Zaldarriaga [astro-ph/0305272]
- [97] J. R. Pritchard, M. Kamionkowski, *Annals Phys.* 318, 2 (2005) [astro-ph/0412581]
- [98] N. Goldberg *et al.*, *J. Math. Phys.* 8, 2155 (1966)
- [99] A. Challinor [astro-ph/0502093]

- 
- [100] J. R. Bond, G. Efstathiou, MNRAS 226, 655 (1987)
  - [101] Y.-T. Lin, B. D. Wandelt [astro-ph/0409734]
  - [102] E. Newmann, R. Penrose, J. Math. Phys. 7, 863 (1966)
  - [103] C.-P. Ma, E. Bertschinger, ApJ 429, 22 (1994) [astro-ph/9308006]
  - [104] C. Misner, K. S. Thorne, J. A. Wheeler, *Gravitation* (Freeman, San Francisco 1973)
  - [105] L. Knox, M. S. Turner, Phys. Rev. Lett. 73, 3347 (1994) [astro-ph/9407037]
  - [106] J. R. Bond, A. S. Szalay, ApJ 274, 443 (1983)
  - [107] R. K. Sachs, A. M. Wolfe, ApJ 147, 73 (1967)
  - [108] Burles *et al.* 1999 f
  - [109] Tegmark M., Physical Review D 55, 5895

# Acknowledgments

I would like to thank Lauro Moscardini and Fabio Finelli for their support, encouragement and patience.

I wish to thank the people at IASF-Bologna who have been part of this work, Alessandro Gruppuso, Daniela Paoletti and Adriano de Rosa. Thanks also to Matteo Galaverni and Pietro Procopio and all the other people who have made life at the institute enjoyable.

I thank George Efstathiou and Steven Gratton for their helpfulness and kindness, and the Institute of Astronomy of Cambridge where part of this work has been carried out.

I acknowledge the *Planck* CTP working group, the use of the Planck Sky Model and of the Healpix package.